Overcoming the limits of strain-induced martensitic transformation in metastable face-centered cubic alloys

by

Shaolou Wei

B.Eng. Materials Science and Engineering
Harbin Institute of Technology, 2017

SUBMITTED TO THE DEPARTMENT OF MATERIALS SCIENCE AND ENGINEERING
IN PARTIAL FULFILLMENT OF THE REQUIREMENTS FOR THE DEGREE OF

Doctor of Science in Materials Science and Engineering

at the

MASSACHUSETTS INSTITUTE OF TECHNOLOGY

January, 2022

Signature of Author:…………………………………………………………………………
Department of Materials Science and Engineering
January 10, 2022

Certified by:………………………………………………………………………………….
C. Cem Tasan
Thomas B. King Associate Professor of Metallurgy
Thesis Supervisor

Accepted by:………………………………………………………………………………….
Frances M. Ross
Chair, Departmental Committee for Graduate Studies

Overcoming the limits of strain-induced martensitic transformation in metastable face-centered cubic alloys

by

Shaolou Wei

B.Eng. Materials Science and Engineering
Harbin Institute of Technology, 2017

Submitted to the Department of Materials Science and Engineering
on January 10, 2022, in Partial Fulfillment of the Requirements for the Degree of

Doctor of Science

Abstract

Metastable phenomena are ubiquitous and have enabled substantial property enhancement for metallic alloys. Amongst them, martensitic phase transformations activated by plastic straining are considered as one of the most effective pathways to promote strength while preserving desirable ductility. The resultant transformation-induced plasticity effect has enabled great success in advancing steels, titanium alloys, and more recently complex concentrated alloys design. However, an intrinsic dilemma is still hindering the development of these metastable alloys: the limited plastic strain accommodation capability of the martensite often leads to early-stage damage nucleation.

This thesis builds upon the objective to overcome such an intrinsic dilemma and explores potential microstructural design guidance with the aids of *in-situ* experiments and theoretical calculations. Two categories of approaches, respectively focusing on phase transformations and plastic deformation micro-mechanisms are explored. Specifically, plastic strain-induced sequential martensitic transformation and thermally-driven martensite reversion are recognized to exhibit the potentials to further improve the mechanical properties of metastable alloys. In light of the atomistic processes of strain-induced face-centered cubic (FCC) to hexagonal close-packed (HCP) martensitic transformation, a plastic deformation-driven stacking fault formation concept is also assessed, which contributes to latent strain hardening while mitigating the formation of blocky HCP-martensite. Future suggestions for metastable alloy design are also proposed based on the current experimental and theoretical understandings.

Thesis supervisor: C. Cem Tasan
Title: Thomas B. King Associate Professor of Metallurgy

Dedication

Affectionately dedicated to those who have advanced the science and technology of physical metallurgy.

Acknowledgments

In the short period of my life so far, I have had the privilege and fortune to meet a great number of excellent people who have helped me in different aspects to establish my attitude towards science. Even though thanking all of them in one written document might not be possible, I will make an attempt to sincerely acknowledge some of these important people.

First and foremost, to Professor Cemal Cem Tasan, my thesis supervisor, I most gratefully thank you for the invaluable guidance and unlimited support throughout my entire doctoral study. It is my greatest pleasure and honor to have had the opportunity to study after you. Your enthusiasm about science, perseverance in truth, and optimism towards failure have truly encouraged me in more ways than one and much more beyond what is presented in this written thesis! I heartfully thank you for respecting all my interest in different aspects of physical metallurgy and for always being supportive in helping me to consolidate, peruse, and accomplish one after another, which has finally enabled me a joyous, eventful, and productive Sc.D. Throughout my tumultuous four-year life at MIT, you have been the most resourceful person who always helps me see a way through all the challenges and difficulties. Thank you again, fondly, for everything!

To my thesis committee members, Professor Christopher A. Schuh and Professor Ju Li, I am deeply indebted to you for being the important elements for my research and for all your insightful comments and suggestions. You have been critically helpful in evaluating my thesis work and have pushed me beyond what is expected for me. I truly cherish your support and guidance.

To Professor Ju Li, I am extraordinarily grateful to you for all the detailed support-no matter experimental or theoretical-you offered ever since I started my thesis research. I most genuinely believe that Course 3.33 "Defects in Materials", which I took after you, is one of the best at MIT: it deepens my understanding of phase transformations and strongly promotes my interest in the physics of plasticity micro-mechanisms, as Chapter 4 of this thesis shows. I would like to express my sincere gratitude to you for the inspiring discussion, valuable suggestions, and kind encouragement.

To Professor Lallit Anand, I am deeply humbled to get to know you and have had the prestigious opportunity to accomplish my minor program in solid mechanics with your guidance and support. I am especially grateful to you for not only teaching me the fruitful knowledge of mechanics but also for personifying the rigorous, precise, and creative mind that a scientist shall always aim to develop. I truly cherish your considerate advice to me for my future academic career, hopefully, as a faculty member.

To all the group members and lab mates, it has been my greatest pleasure to work with all of you. You have all been supportive, helpful, and empathetic throughout all my research activities. Having been able to learn, fail, succeed, and eventually grow academically together at MIT is the bittersweet memory that will never perish wherever I go. Especially, to Dr. Jinwoo Kim, you took me under your wings when I was a first-year student. The detailed training and mentorship you provided became the solid foundations for my research at MIT. It is also ceremonial that I managed to co-author with you the first and the last papers when I was a doctoral student. I promise that your kindness will be circled to the younger fellows.

To the technicians of the department, Dr. Michael J. Tarkanian, Dr. Shaymus Hudson, Dr. James Hunter, Dr. Yong Zhang, and Dr. Geetha Berera, I truly appreciate your support in all aspects of my research activities. Some experiments presented in the thesis will never become possible without your detailed support.

Now turning to my personal connections, whom, provided the limited space here, I shall still acknowledge briefly but heartfully.

To Feng He and Shao-Shi Rui, I am deeply indebted to all your personal encouragement and camaraderie. Time flies so fast that you have already become faculty members and started to recruit your own graduate students! Every time I recall my early days at MIT, it still feels like it was just yesterday that two of you were like the elder brothers helping me in many ways. There is always a big smile on my face whenever I reminisce about the time we were together! Thank you fondly, for being the most truthful academic buddies during my doctoral study.

To my close friends at MIT, Jiyun Kang, William Yu-Ren Zhou, S. Mohadeseh Taheri-Mousavi, Yuntong Zhu, Hyunseok Oh, Tingyu Su, and Jonathan Paras, thank you for being an essential part of my life in graduate school. I can never become the person I am today without your emotional support and personal encouragement. Thank you truly, for the friendship!

Last but not least, to my family, albeit I never say it aloud, you are always my constant source of strength.

I would like to finalize the Acknowledgements by replicating a paragraph that I wrote in the personal statement when I applied to MIT in 2016.

"*I am fascinated by the forms and microstructures I see around me and how they are mirrored in our inner world. So while I would like to work in the research fields such as dendritic growth kinetics, composite materials, complex concentrated alloys, and TRIP steels, throughout my entire life at universe I do hope I can develop some of those characteristics of preeminent, solidary, versatile, and perseverance in myself as a human being...*"

After six years, in 2022, I still naively, but affectionately believe that these correlations philosophically exist, and I am ready to be dedicated to exploring more of them as I grow academically and professionally as a physical metallurgist.

Table of Contents

List of Figures

List of Tables

Chapter 1: Introduction

Section 1.1: Overview

Metals and alloys are mankind's most essential structural materials and witnessed the coming of human civilization. For structural applications, mechanical strength and ductility are two of the most important properties that trigger appreciable alloy design activities. To realize optimal strength-ductility combination, martensitic transformation activated by plastic deformation are often considered as the most effective microstructural design strategy. This is because the onset of such a phase transformation has the effects of relieving local stress concentrators, improving strain hardenability, and promoting homogenous plastic deformation. These benefits jointly contribute to the increase in strength, ductility, and toughness. Successful applications this sort of metastable microstructural design concept are also numerous: kiloton production of transformation-induced plasticity (TRIP) steels in the automobile industry is one such examples.

While these metastable alloys can exhibit noticeable mechanical property enhancement compared with their stable counterparts, one intrinsic dilemma still persists. Because of deformation incompatibility, the resultant transformation product, martensite, is often acting as the origin of damage nucleation and sometimes causing local embrittlement in the microstructure. Motivated by this intrinsic shortcoming, the present thesis aims to seek for novel microstructural design strategies on the basis of *in-situ* experimental investigations. Specifically, phase transformation-guided strategy and plasticity micro-mechanism-guided strategy will be systematically assessed.

The introductory chapter of the thesis will be developed as follows: first, a general background of metastability effect will be introduced followed by the important elements of martensitic transformation. Next, strain-induced martensitic transformation will be discussed in greater depth with a combination of its historical aspects and the state-of-the-art progress in the literature. Finally, the structure of the thesis will be presented.

Section 1.2: Background

Portions of this Section are based on:

[1] <u>S.L. Wei</u> et al., Metastability in high-entropy alloys: a review. **Journal of Materials Research**, 2018, 33: 2924-2937.

[2] <u>S.L. Wei</u> et al., Boundary micro-cracking in metastable $Fe_{45}Mn_{35}Co_{10}Cr_{10}$ high-entropy alloys. **Acta Materialia**, 2019, 168: 76-86.

Section 1.2.1: Metastability and Its Relevance for Microstructural Design

Metastable phenomena are ubiquitous and have revealed salient advantages in structural alloy development. The examples are numerous: transformation or twinning-induced plasticity steels, cobalt or titanium alloys, age hardenable aluminum alloys, and nano-structured copper alloys produced by severe plastic deformation. In each of these cases, exceptional engineering property combinations are achieved by exploring limits of stability. While comprehensive overview of metastable states of alloys is well-documented in physical metallurgy textbook, the delimitation and categorization of metastability is briefly presented here for the sake of completeness. A "metastable" system, following the definition of the inventor for this terminology, W. Ostwald [1], persists in its existing state when undisturbed or subject to disturbances smaller than some small or infinitesimal amount, but passes to a more stable state when subject to greater perturbations. Using more thermodynamic terminology, such metastable states correspond to states that possess excess free energy compared to that of equilibrium states. According to Turnbull [2], three kinds of metastability can be identified, which would lead to the creation of such an excess free energy: morphological (arising from crystallographic defects), compositional (arising from supersaturated solid solutions), and structural (arising from metastable phases). Often such effects present simultaneously, since processing treatments that lead to metastability (e.g. quenching from elevated temperatures) generate multiple microstructural changes. The major scope of the thesis, presented hereafter, focuses on structural metastability, and to be more specific, phase transformations activated by plastic deformation.

In pursuance of optimal load-bearing performances in metallic alloys, displacive phase transformations upon deformation are regarded as one of the most effective approaches to enhance strain hardenability and impede plastic instability incipience [3,4]. Such positive contributions can be found in high-strength steels development, for example (**Figure 1.1**). The metastable transformation transformation-induced

plasticity (TRIP) steels which benefits from strain-induced martensitic transformation, exhibits improved strength-ductility combination than its stable counterparts.

The rest of this section will provide a detailed discussion, focusing on martensitic transformation active by plastic deformation. More specifically, **Section 1.2.2** reviews the important elements for martensitic transformation in general; **Section 1.2.3** discusses strain-induced martensitic transformation; **Section 1.2.4** focuses on the challenges of strain-induced martensitic transformation as well as reported solution in the literature.
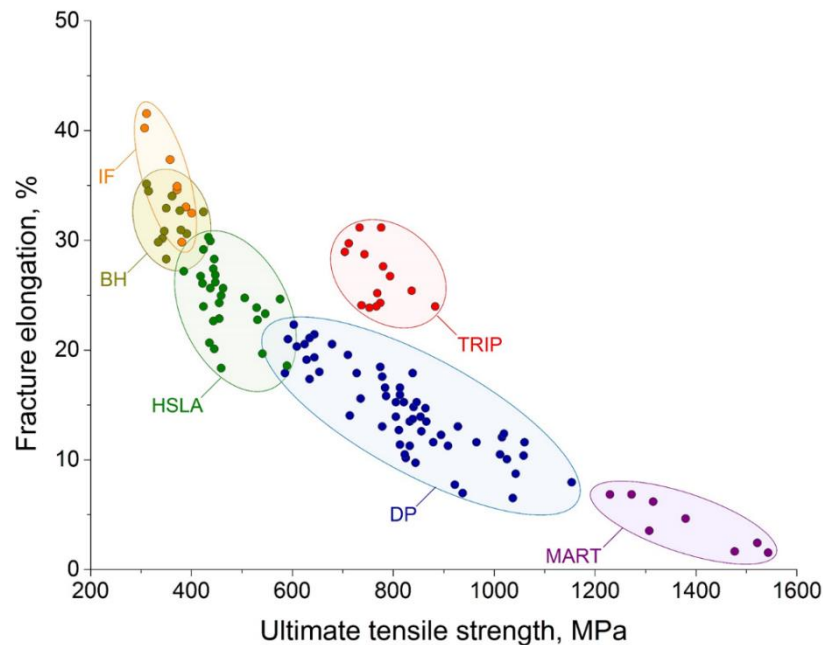
Figure 1.1: Mechanical property comparison for various steels. Data point for commercialized steels were extracted from Tata Steel Europe. Abbreviations adopted in this plot: IF: interstitial free, BH: bake hardenable, HSLA: high-strength low alloy, DP: dual phase, and MART: martensitic.

Section 1.2.2: Important Elements of Martensitic Transformation

This section provides a short overview of the important historical elements of martensitic transformation, including its definition, thermodynamic condition, nucleation features, and crystallographic characteristics.

Unlike other types of phase transformations in metallic alloys, the formation of martensite is accomplished by the deformation of its parent austenitic lattice without long-range diffusion of alloying

elements. Historically, martensitic transformation was first defined as a sub-category of displacive phase transformations by Cohen, Olson, and Clapp at the 1979's International Conference of Martensitic Transformation [5] (ICOMAT79 at MIT). As illustrated in **Figure 1.2**, compared to the wider world of displacive transformations, martensitic transformation mostly shares the common characteristics of [6]:

(1) lattice-distortive displacement;

(2) extensive deviatoric strain component;

(3) strain energy dominance.
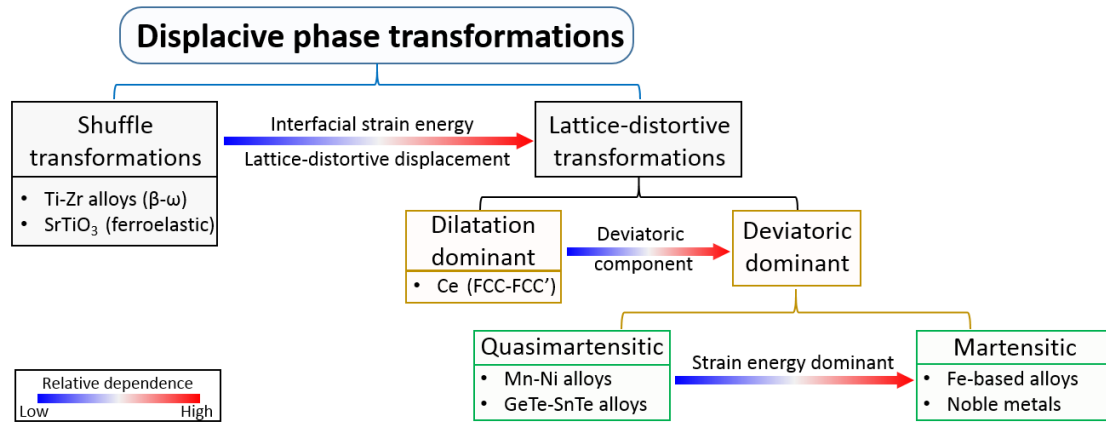
Figure 1.2: Characteristics of martensitic transformation compared with the wider world of displacive phase transformations.

Associated with volumetric variation and release of latent heat, martensitic transformation possesses the common characteristics of first-order phase transformation, for which sophisticated thermodynamic theories have been established. As schematically displayed in **Figure 1.3 (a)**, the thermodynamic driving force of martensitic transformation comes from the free energy difference $\Delta G^{M-P} = G^M - G^P$ between martensite (M) and its parent phase (P). It should be noted that owing to the displacive nature, the transformed martensite exhibits the same composition as its parent phase, and such a feature requires extra thermodynamic driving force [7] (thus $\Delta G^{M-P} < 0$), indicating that at a certain temperature T_1, martensitic transformation cannot take place with solute concentration higher than X_C. By connecting all the critical composition at given temperatures, a T_0 line can be subsequently constructed within the phase diagram, the left of which represents the parent phase compositions that are possible to initiate martensitic transformation. In the following discussion M_s and M_f will be utilized to denote

martensitic transformation starting and complete temperatures.

For a given parent phase composition X_A (strain energy is firstly ignored) at a certain temperature T_1, tie line $|AD|$ represents the thermodynamic driving force for an equilibrium transformation. At the eventual stage of it the composition will be partitioned into $X_\alpha^{eq.}$ and $X_\gamma^{eq.}$. Whereas the displacive nature of martensitic transformation prohibits the elemental partitioning, and as a result, the thermodynamic driving force is altered to the value of $|AC|$. If strain energy is also taken into account (dashed line in the schematics), the nominal driving force for martensitic transformation correspondingly varies to $|AB|$. It should be pointed out that the prediction of thermodynamic driving force for martensitic transformation extensively relies on the selection of solution model that applied to the calculation of G^M and G^P, representative work can be found in the literature [7–10]. A connection between thermodynamics and transformation kinetics can be established by the temperature-transformation-time diagram (TTT-diagram, **Figure 1.3 (b)**), where it is evident that either the formation of martensite or the stabilization of metastable austenite requires comparatively high cooling rate to suppress diffusional phase transformation.
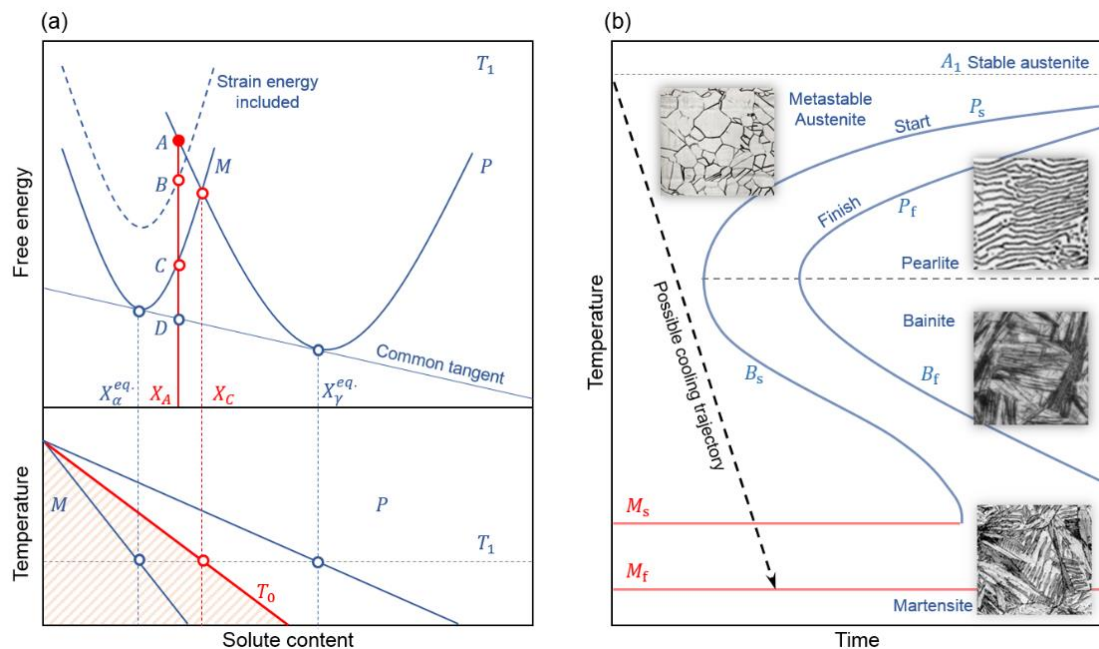
Figure 1.3: Thermodynamics of martensitic transformation. (a) Illustration of thermodynamic driving force; (b) schematic of TTT-diagram and a possible cooling trajectory

According to Olson and Roitburd [11], theories regarding the nucleation of martensite can be

categorized on the basis of heterogeneity, strain path (structure), and relaxation (substructure). As illustrated in **Figure 1.4**, X_1 axis describes the strain path of transformation by strain order parameter η which is defined as the relative strain level θ/θ_M, and thus $\eta = 0$ denotes parent phase, while $\eta = 1$ indicates the completeness of transformation. In this sense, classical nucleation theory treats the structural core of martensite as $\eta^* = 1$, whereas nonclassical nucleation theory allows transition state $(\eta^* < 1)$, including $\eta^* \to 0$ where the lattice approaches instability incipience. X_2 axis represents the strain relaxation level within the martensite that dominates the interfacial structure and substructure within the martensite (such as twins and stacking faults). X_3 axis denotes the heterogeneity of nucleation, where homogenous nucleation stands for the cases where comparatively weak interaction exists amongst the defects [12]. Heterogeneous nucleation is also classified into two groups based on the "intensity" of defects, namely, whether or not stable defect embryo exists prior to the nucleation of martensite. In fact, defect structures developed during martensitic transformation closely depends on the imposed boundary conditions, since the primary scope of the thesis is on strain-induced martensite, relevant discussion on such topics is provide in **Section 1.2.3**.
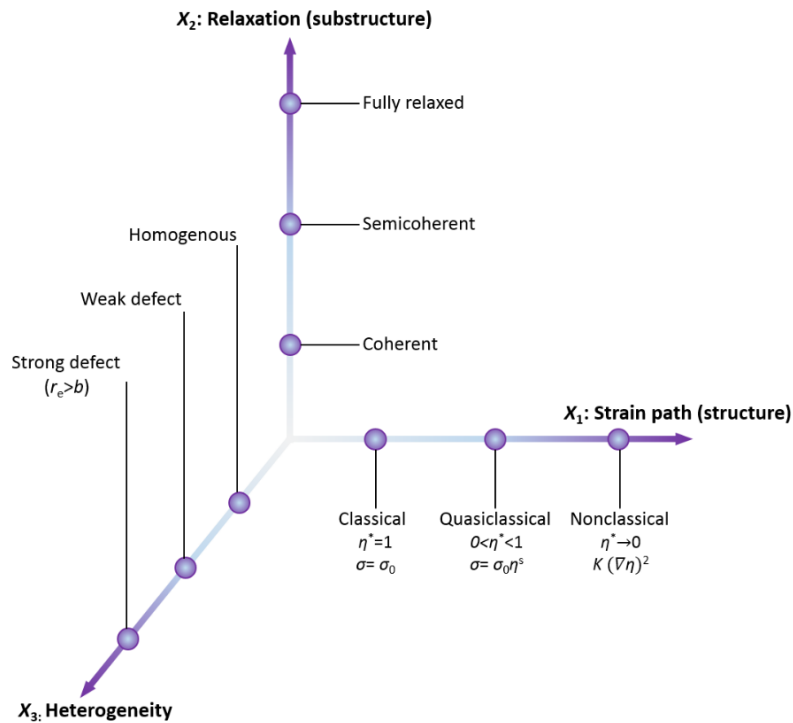
Figure 1.4: Illustration of the theoretical space of martensite nucleation

Ever since the recognition of the shear strain-assisted characteristic of martensitic transformation,

appreciable theoretical attempts were accomplished to elucidate the underlying crystallographic features. The first crystallographic theory for martensitic transformation was proposed by Bain [13] in 1924 regarding the face-centered cubic (FCC) to body-centered tetragonal (BCT) transformation in Fe-C alloys. It was postulated that BCT structure pre-existed in the parent FCC lattice where such a transformation can be simply accomplished by the subtle position adjustment of the parent lattice atoms. The corresponded expansion of two axes of the parent lattice and contraction of the third one can be expressed in matrix form:

$$\boldsymbol{B} = \begin{bmatrix} \sqrt{2}a/a_0 & 0 & 0 \\ 0 & \sqrt{2}a/a_0 & 0 \\ 0 & 0 & c/a_0 \end{bmatrix} \tag{1.1}$$

In **Eq. (1.1)**, a_0 is the lattice constant of the parent FCC-lattice, a and c denote the lattice constants of the BCT-martensite. **Eq. (1.1)** is also known as the Bain strain, which connotes the structural change during martensitic transformation. While Bain's theory successfully predicts the transformation pathway for minimum atom displacement, it fails to match with the invariant plane strain associated with martensitic transformation. With regard to this, in 1953, Wechsler, Lieberman, and Read employed matrix algebra to further describe the crystallographic characteristics (W-L-R theory [14]). It was proposed that the total invariant plane strain of martensitic transformation can be decomposed into three sub-parts (see **Figure 1.5**, following [15]):

(1) Bain strain (**$\boldsymbol{B}$**) for lattice structural change;

(2) Shape strain ($\overline{\boldsymbol{P}}$) for lattice invariant shear events (such as dislocation slip and/or twinning);

(3) Rigid lattice rotation (**$\boldsymbol{R}$**) for crystallographic orientation.

Thus the invariant plane strain can be calculated as:

$$\boldsymbol{P}_1 = \boldsymbol{R}\overline{\boldsymbol{P}}\boldsymbol{B} \tag{1.2}$$

Based on **Eq. (1.2)**, once given the lattice parameters of parent and martensitic phases together with the lattice invariant shear systems (either slip or twinning), the corresponded habit plane, crystallographic orientation, and shear strain can be subsequently predicted. Considering the translatable symmetry of

Eq. (1.3) where the sequence of Bain strain and shape strain can be exchanged:

$$P_1 P_2 = RB \qquad (1.3)$$

Since both P_1 and $P_2 = \overline{P}^{-1}$ are invariant plane strain, their combination represents an invariant line strain RB. **Eq. (1.3)** was independently proposed by Bowles and Mackenzie in 1954 (B-M theory [16,17]) which has also been widely adopted to determine crystallographic parameters with given line strain. To date, both W-L-R and B-M theories have been successfully applied to martensitic transformations in both ferrous and nonferrous metals, although their capability in explaining the formation martensitic substructures still remain to be further developed.
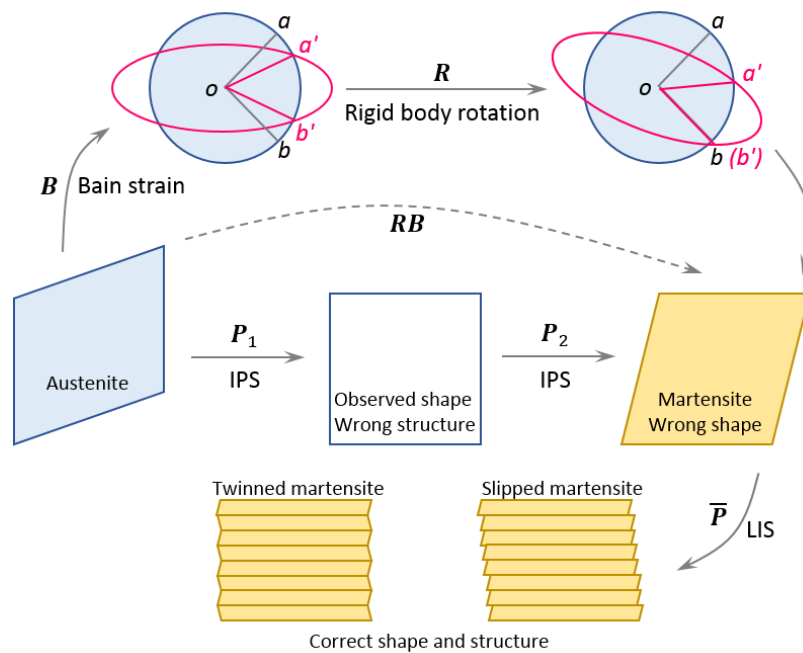
Figure 1.5: Schematic of W-L-R and B-M crystallographic theories of martensitic transformation. Abbreviations adopted in this plot: IPS: invariant plane strain, LIS: lattice invariant shear. This schematic is based on ref. [15].

Section 1.2.3: Strain-induced Martensitic Transformation

To understand the influence of stress and deformation, Olson et al. [18] introduced a critical temperature M_d (**Figure 1.6 (a)**), above which deformation was unable to facilitate martensitic transformation. It should be noted that although stress and strain have both been termed in the literature to describe the

origin of external driving force, in the present study "strain-induced martensitic transformation" is referred to the cases where plastic deformation of the parent phase takes place prior to the formation of martensite (corresponds to TRIP effect), whereas "stress-induced martensitic transformation" implies only elastic deformation occurs within the parent phase (corresponds to pseudoelasticity [19]). External mechanical loading mostly affects martensitic transformation in two ways:

(1) it acts as an extra driving force that raises the M_s point;

(2) it alters the internal stress state of martensite that leads to the variation in martensitic morphology and the formation of particular variant.
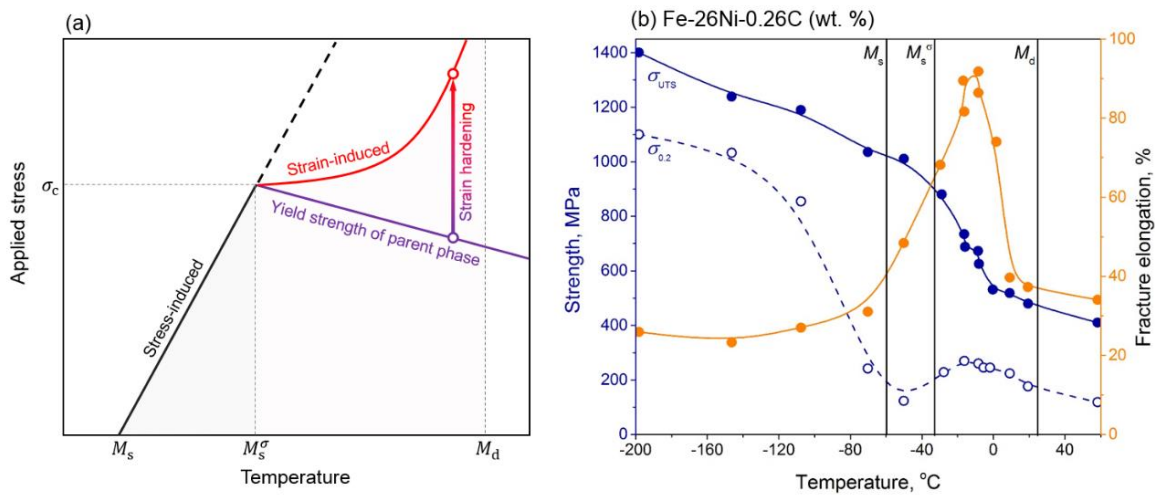
Figure 1.6: Influence of external stress on martensitic transformation. (a) Theoretical illustration of the mechanical criterion for strain-induced martensitic transformation; (b) tensile properties of Fe-26Ni-0.26 C alloys [20] with respect to testing temperature.

Patel and Cohen [21] summarizes the critical stress for the incipience of martensitic transformation, where M_s^σ was introduced to denote the temperature where the external stress required for martensitic equaled the yield stress of parent phase. Therefore, in the temperature range of M_s to M_s^σ martensitic transformation takes place before the parent phase reaches its yielding point, leading macroscopically observed pseudoelasticity. When the temperature exceed M_s^σ, plastic relaxation in the parent phase will occur the corresponded strain hardening effect will lift the stress level to the critical value to activate martensitic transformation. As evidenced by Tamura et al. [20] in Fe-Ni-C alloys (**Figure 1.6 (b)**), when the testing temperature is kept between M_s^σ and M_d a significant increase in tensile elongation can be achieved, implying the strain-induced martensitic transformation contribute to ductility enhancement,

and such a phenomenon refers to the widely documented "transformation-induced plasticity" (TRIP) effect.

An important structural aspect of strain-induced martensitic transformation lies in the fact that the resultant martensitic structures (i.e. the transformation pathways) highly depend on the composition of the alloy. Although appreciable achievement has been accomplished in both ferrous and non-ferrous systems, the following discussion will mostly focus on Fe-Mn systems [22] which share some similarities with the alloys to be investigated in the present thesis. Depending on the Mn content, which thereby affects the intrinsic stacking fault energy, two typical transformation pathways are commonly documented in the metastable Fe-Mn-based alloys.

First, the FCC (austenite, γ) → hexagonal close-packed (HCP, martensite, ε) → BCT (martensite, α') transformation. According to Chowdhury et al. [22], this sort of transformation exists in alloys with medium Mn content (approximately 5-12 wt. %). Fujita et al. [23], investigated such type of transformation in an Fe-Cr-Ni alloy under *in-situ* transmission electron microscope (TEM). They observed that during deformation, secondary deformation-driven BCT-martensite frequently nucleated at the intersection between priori ε-martensitic bands formed along the primary or conjugate slip planes of parent FCC-austenite (**Figure 1.7**).
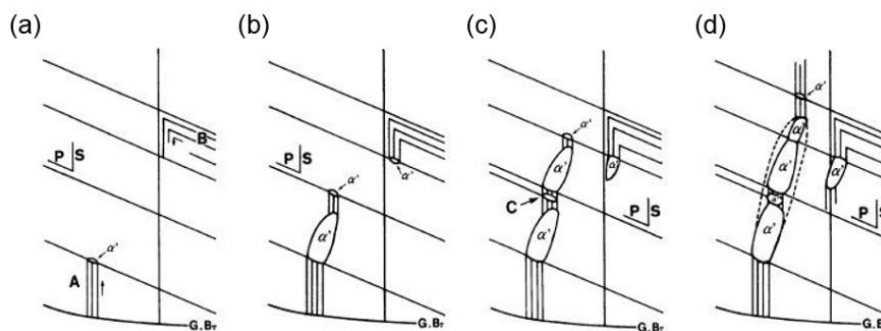
Figure 1.7: Schematic of the strain-induced FCC-HCP-BCT transformation pathway. (a) Nucleation of the BCT embryo from the intersection of HCP martensite and slip band; (b)-(d) growth of the BCT martensite.

Similar to the work reported by Liu et al. [24], FCC-BCT transformation can also be accomplished without the formation of HCP-marensite. Liu et al. [24], and Fujita et al. [23] both ascribed the

underlying mechanisms to local stress concentration and the existence of strong defects such as austenitic grain or twin boundaries. More recent mechanistic studies carried out using high-resolution transmission electron microscope (HRTEM) also highlights the potential role of atomic shuffle in assisting the HCP-BCT transformation [25,26].

Second, the FCC (austenite, γ) $\rightarrow$ HCP (martensite, ε) transformation. This kind of transformation is more frequently observed in alloys with higher Mn content (around 15-30 wt. %). Fruitful theoretical and experimental investigations have been achieved regarding this transformation pathway. Based on dislocation structures, Christian once predicted that stacking faults originated from the decomposition of perfect dislocations can act as the nucleation sites of HCP-martensite through the asynchronous motion of leading and trialing partials [27]. Later in the 1980s, Olson and Cohen [28,29] established the stacking fault-assisted HCP-martensite transformation theory, where they hypothesized that HCP-martensite can nucleate on the intrinsic stacking faults through <112> direction glide of partials on very other {111} plane of the parent FCC-phase (**Figure 1.8**). Such a mechanism was then widely validated by high-resolution diffractomety and microscopy characterization techniques in both thin foil and bulk specimens [30,31]. It should be noted that owing to such a transformation mechanism, HCP martensite displays an orientation relation of $\{0001\}_{HCP}//\{111\}_{FCC}$, $\langle11\bar{2}0\rangle_{HCP}//\langle110\rangle_{FCC}$.
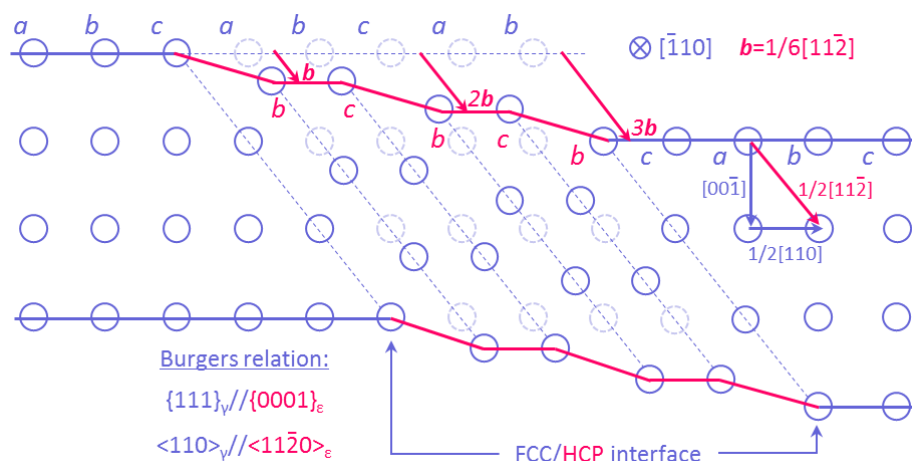
Figure 1.8: Schematic of the atomistic mechanisms for the strain-induced FCC-HCP transformation (based on ref. [29]).

One of the conspicuous differences between FCC-HCP-BCT and FCC-HCP transformation pathways

lie in the resultant defect structures formed during the transformation. Theoretically, the BCT-martensite formation, according **Eq. (1.2)** and **Figure 1.7** requires significant plastic accommodation because of the Bain strain, lattice invariant shear events, as well as lattice rigid rotation that are involved. Exemplary *in-situ* TEM study by Liu et al. [24] validates the extensive dislocation activity during the formation such a martensite (**Figure 1.9 (a)**). The FCC-HCP transformation pathway, in contrast, is accompanied by less amounts of defect substructures formation. This can be rationally understood from **Eq. (1.2)** and **Figure 1.8**: because of the similar stacking sequence between FCC (i.e. $ABCABC$) and HCP (i.e. $ABABAB$) lattices, the FCC to HCP transformation can be accomplished by a simple shear deformation and the resultant interface is ideally coherent and rather mobile. As comparatively demonstrated in **Figure 1.9 (b)**, the *in-situ* TEM experiment reported by Jiang et al. [32], reveals that upon the formation of HCP-martensite, negligible amounts of defects form in interface vicinity, confirming the moderate plastic accommodation within the parent FCC-phase.
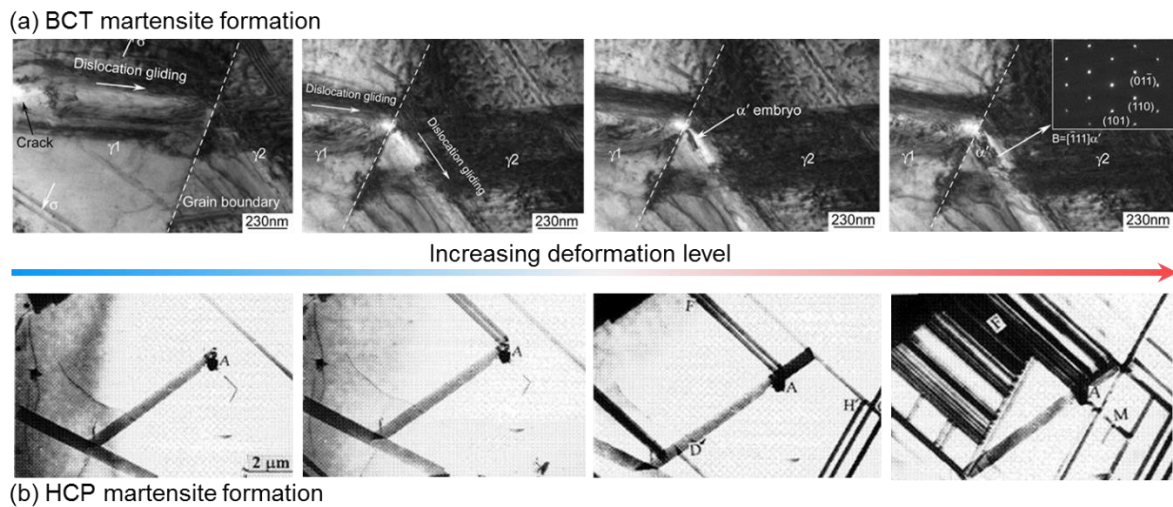
Figure 1.9: Comparison of defect substructural evolution during different strain-induced martensitic transformation pathway. (a) BCT martensite formation [24]; (b) HCP martensite formation [32].

In terms of mechanical performances, it has been widely recognized that owing to the strain-induced martensitic transformation, TRIP-assisted metastable alloys exhibit comparatively higher strength and more uniform elongation before failure compared to their stable counterparts. The underlying strengthening mechanisms can mostly understood from two respects:

(1) the creation of extensive amounts of phase boundaries: resulting from the incipience of martensitic transformation, high volumetric fraction of martensite/austenite phase boundaries are subsequently formed. Li et al. [33] revealed by electron channeling contrast imaging that the dislocations pile up at the HCP-martensite/FCC austenite boundaries contributing to strength enhancement (**Figure 1.10 (a)**). Similar phenomena were also reported by Fujita et al. [23] for BCT-martensite/FCC-austenite phase boundaries.

(2) the formation of stronger martensitic phase: the product of the TRIP effect, martensite, often exhibits superior strength to its parent austenite. By incorporating neutron diffraction technique into tensile testing, Harjo et al. [34] reported that martensite accommodated the extensive plastic stress once they were formed during deformation, while in contrast, the stress accommodation from untransformed austenite was more moderate (**Figure 1.10 (b)**).
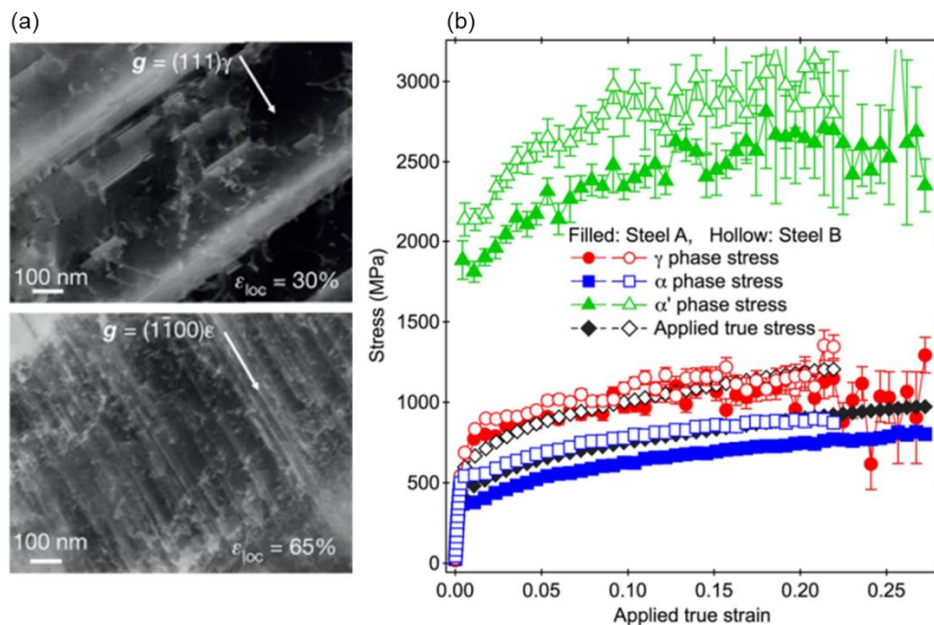
Figure 1.10: Experimental evidence of the strengthening mechanisms by strain-induced martensitic transformation. (a) The creation of extensive amounts of phase boundaries; (b) The formation of stronger martensitic-phase.

Section 1.2.4: Dilemma and State-of-the-art

As discussed in the previous Section, while strain-induced martensitic transformation can bring about desirable mechanical property improvement, including ultimate tensile strength and fracture elongation

improvement, the resultant product, martensite, is not desirable in terms of damage tolerance.

In fact, owing to the hardenability difference between transformed martensite and the parent phases, interfacial decohesion failure module has been widely highlighted in TRIP-assisted ferrous-based alloys. Koyama et al. [35] examined the fracture mechanisms of an Fe-Mn-C alloy at various temperatures under tensile loading (Fig. 2.8). From post mortem microscopy and topography observations, they demonstrated that the principal crack initiated at the intersected regime between HCP-martensite and annealing twin boundary which resulted in quasi-cleavage fractography. Lee et al. [36] also reported that the fracture surface of Fe-Mn-Si-C alloys exhibited both dimple and quasi-cleavage characteristics, suggesting that the formation of HCP-martensite was the origin of brittle-like fracture under tensile stress.
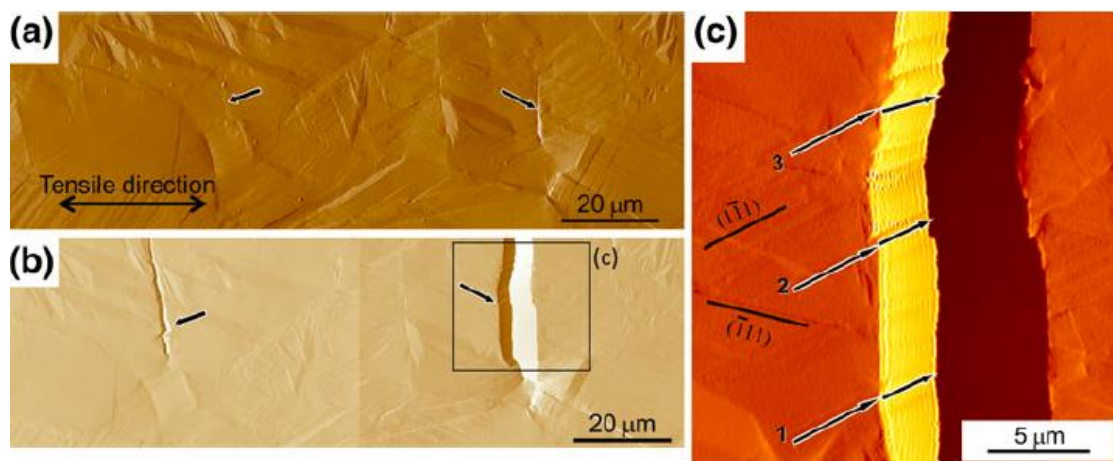
Figure 1.11: Quasi-cleavage fracture in an Fe-Mn-C alloy at ambient temperature. (a) and (b) Atomic force microscope (AFM) topographies of deformed specimens at global strain level 5.0 % and 9.9 %; (c) magnified AFM micrograph of cleavage crack [35].

While these classical post mortem analyses on fracture surface or cross section have brought about qualitative explanations of damage incidents, challenges still remain in:

(1) providing a quantitative assessment of damage evolution characteristics;

(2) interpreting the role of crystallographic orientation differences in the damage process;

(3) synchronous monitoring of both phase and morphological evolution.

To further showcase the damage inception processes that are associated with the strain-induced

martensitic transformation, we detail below an *in-situ* study carried out for a metastable $Fe_{45}Mn_{35}Co_{10}Cr_{10}$ alloy [37], which also motivates the investigations presented in **Chapter 3**.

The study starts with post-mortem damage assessment. **Figure 1.12 (a)** shows the backscattered electron (BSE) micrograph of the cross-section of the fractured $Fe_{45}Mn_{35}Co_{10}Cr_{10}$ alloy. It is seen that a high density of microcracks exists in the necking regime. In terms of morphology, the observed microcracks can be classified into two categories:

(1) cracks with a relatively large aspect ratio and sharp tips (**Figure 1.12 (b)**);

(2) near ellipse-shaped cracks with an inclusion particle at the middle (**Figure 1.12 (c)**).

From a mechanism perspective, such morphological distinctions clearly indicate that both boundary decohesion-induced and inclusion-induced cracking exist in the present alloy. The corresponded SEM micrograph of fracture surface in **Figure 1.12 (d)** displays typical ductile fracture characteristics. As higher magnifications, two types of fracture characteristics can be clearly observed:

(1) comparatively smooth and dimple-free tearing edges (**Figure 1.12 (e)**);

(2) quasi-symmetric dimples with some of which containing spherical inclusions (**Figure 1.12 (f)**).
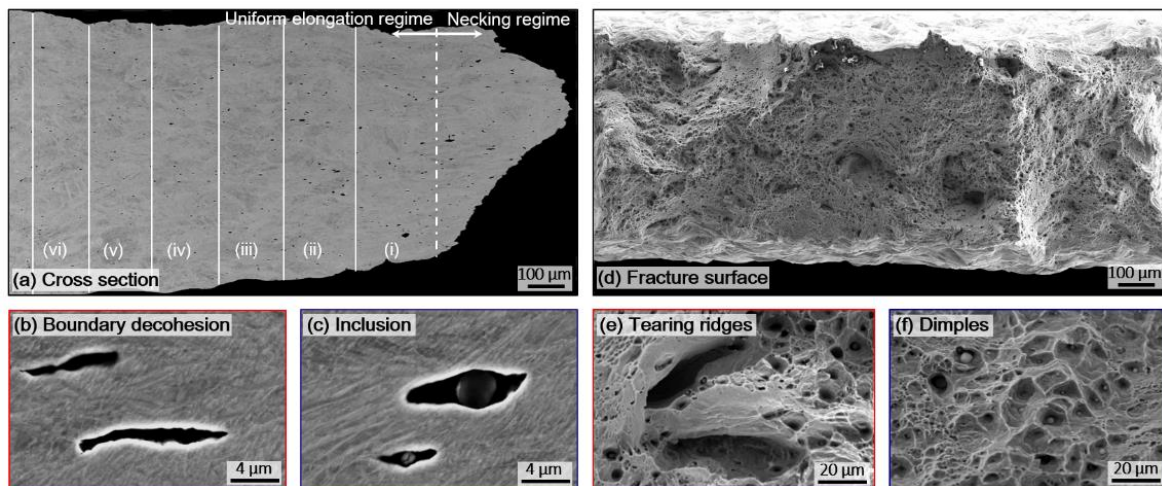
Figure 1.12: SEM micrographs for fracture morphologies after uniaxial tensile testing. (a) Fracture cross-section; (b) boundary decohesion-induced microcracks; (c) inclusion-induced microcracks; (d) fracture surface; (e) dimple-free tearing ridges; (f) quasi-equiaxed dimples.

Figure 1.13 presents a quantitative assessment of the evolution of damage area fraction, number of cracking incidences, and average crack size along the loading direction for both types of cracking

features. In order to better interpret the damage evolution tendency, in the present study the uniform elongation regime has been divided into six equi-area subsections (denoted as (i)-(vi) in **Figure 1.12 (a)**) by setting the necking regime area as a reference unit value. As demonstrated in **Figure 1.13 (a)** and **(b)**, a total number of 29 boundary decohesion-induced microcracks is observed within the necking regime, contributing to 0.69 % of the total area.

In contrast, only 15 inclusion-induced induced cracking events exist within the necking regime, exhibiting a comparatively lower area fraction of 0.17 %. Outside the necking regime, the number of boundary decohesion-induced microcracks exhibits a significant decrease and the corresponded area fraction also demonstrates a similar tendency. However, the quantity of the inclusion-induced microcracks maintains a comparable value to that of the necking regime, and their total area fraction varies within the range of 0.10-0.20 %. In terms of the average crack size evolution (calculated by utilizing the raw data in **Figure 1.13 (a)** and **(b)**), the boundary decohesion-induced microcracks possess an average size of approximately 30.0 μm^2 within the necking regime, which is significantly larger than that of the inclusion-induced ones (about 14.5 μm^2, **Figure 1.13 (c)**). However, the boundary decohesion-induced microcracks exhibit a sharp decrease in their average size outside the necking regime, while in contrast, only small variations exist in the average size of the inclusion-induced microcracks. In the light of the distinctions in damage evolution characteristics and fracture morphologies, it can be concluded that even though two types of cracking event co-exist during deformation, it is the boundary decohesion-induced microcracks that dominate the eventual fracture process.

In order to clarify the mechanisms for boundary decohesion-induced cracking, *in-situ* SEM/EBSD analyses were conducted for a selected area of interest. As confirmed from the *in-situ* EBSD measurement (**Figure 1.14 (a1)**), the monitored regime completely consists of FCC-phase at the undeformed state, and it undergoes elastic deformation until the global stress level exceeds 160 MPa (**Figure 1.14 (a2)** and **(b)**). At such a stress level, the incipience of plasticity can be observed within the upper grain (darker contrast) in the form of parallel slip steps (**Figure 1.14 (b)**), while in the lower grain (brighter contrast), no evident trait of slip steps exists. However, a relatively narrow line with an even brighter contrast appears at the middle of the grain, which is later proved to be the onset of the strain-induced martensitic transformation.
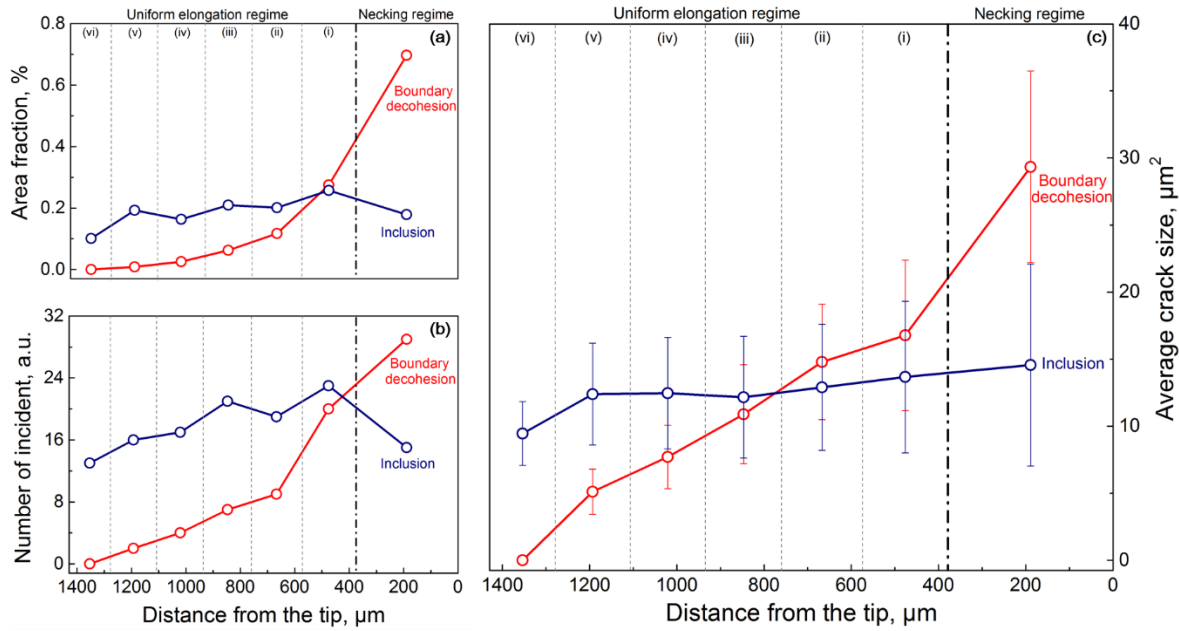
Figure 1.13: Damage evolution characteristics for inclusion-induced and boundary-tearing induced cracking events. (a) Area fraction; (b) number of cracking incidences; (c) average crack size.
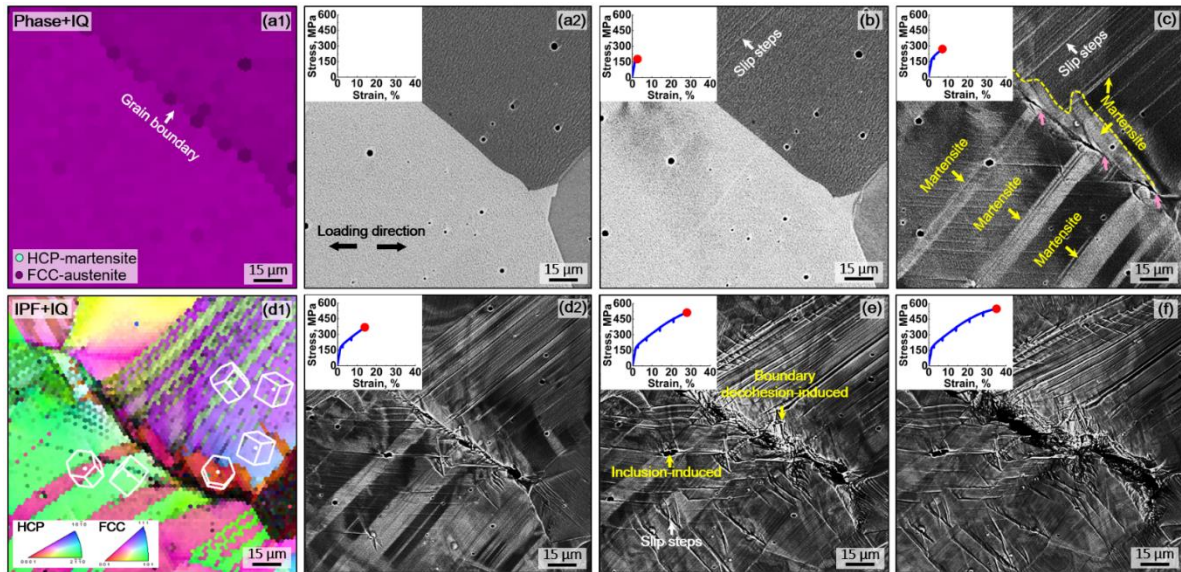
Figure 1.14: In-situ EBSD/BSE analyses of the selected regime at different deformation states with engineering stress-strain curves inserted. (a1) Phase and image quality (IQ) overlapped maps correspond to (a2); (d1) and (d2) IPF and IQ overlapped correspond to (d2).

As the stress level increases to approximately 300 MPa (**Figure 1.14 (c)**), clear traits of martensitic formation appear in the lower grain. Three microvoids (marked with pink arrows) nucleate at the intersected regimes between the transformed martensite and grain boundary. The martensitic transformation features of the upper grain show significant differences at the grain boundary compared

31

to its inner part: a large amount of martensite regions are observed near the grain boundary, while only very thin martensite (thickness close to slip steps) forms inside the grain. When the global stress further increases to about 400 MPa, the nucleated martensite within both the lower and upper grain undergoes an evident thickness increase (**Figure 1.14 (d1)** and **(d2)**). Further EBSD analysis (**Figure 1.14 (d1)**) reveals that a dissimilarly oriented HCP-martensite variant nucleates along the upper grain boundary and the corresponded BSE micrograph confirms the coalescence of the microvoids and the formation of a microcrack at the grain boundary. It is noteworthy that the microcrack exhibits a large aspect ratio together with sharp tips, agreeing well with the observation from the fracture cross-section (**Figure 1.12** (b)). With increasing global stress level (**Figure 1.14   (e)** and **(f)**), the microcrack keeps propagating along the grain boundary, and slip steps also appear in the transformed HCP-martensite. It should be pointed out that only at such high stress levels, the inclusion (or pore) starts to initiate cracking (**Figure 1.14 (d2)-(h)**), however, its size is almost negligible compared to the principal crack induced by grain boundary decohesion.

Figure 1.15 demonstrates the in-situ EBSD analyses of the monitored boundary decohesion regime at a global stress level of 400 MPa. As reveled in **Figure 1.15 (a)** and **(c)**, the intersection regimes between the transformed martensite and the grain boundary display significantly higher kernel average misorientation (KAM) and grain reference orientation deviation (GROD) values compared to the inner grain regime.

Such distinctions are indicative of the strong plasticity gradient localized at the grain boundary regime, which is mainly attributed to the volumetric change that associated with the strain-induced martensitic transformation. Interestingly, as revealed by the crystallographic analyses (details presented in **Chapter 3**), approximately 1 % volumetric contraction is convinced to accompany with the martensitic transformation upon deformation, giving rise to the observed strain incompatibility. It shall be noted that such a volumetric contraction upon the formation of HCP-martensite has also been reported in Si interstitial-doped Fe-Mn-based shape-memory alloys [38], however, the origin of the same phenomenon in pure substutional alloys still remains to be further explored.

The geometrically necessary dislocation (GND) density in both austenitic and martensitic phase reaches

a level of 10^{12}-10^{13} m^{-2}, in particular, the GND density near the grain boundary exhibits a relatively larger value compared to the inner grain regime (**Figure 1.15 (d)** and (**e**)), which further supports the highly localized incompatible strain. The pole figure for crystallographic orientation analyses reveals that the martensite in both lower and upper grains yield a typical Burgers relation with the parent austenite, coinciding with the results recognized in the literature. Nonetheless, the martensite near the upper grain boundary displays an orientation of $(111)_\gamma//(0001)_\varepsilon$ compared to that of its inner grain counterpart which exhibits $(1\bar{1}1)_\gamma//(0001)_\varepsilon$. Note that here the orientation is referred to different martensitic variants which share the common $\{111\}_\gamma$ family plane given their difference in the Miller indices (plus or minus 1, see **Figure 1.15 (b)**). The formation of this specific martensitic variant along the upper grain boundary results in the suppression of slip transfer between the two adjacent grains which also contributes to the localized incompatible strain.
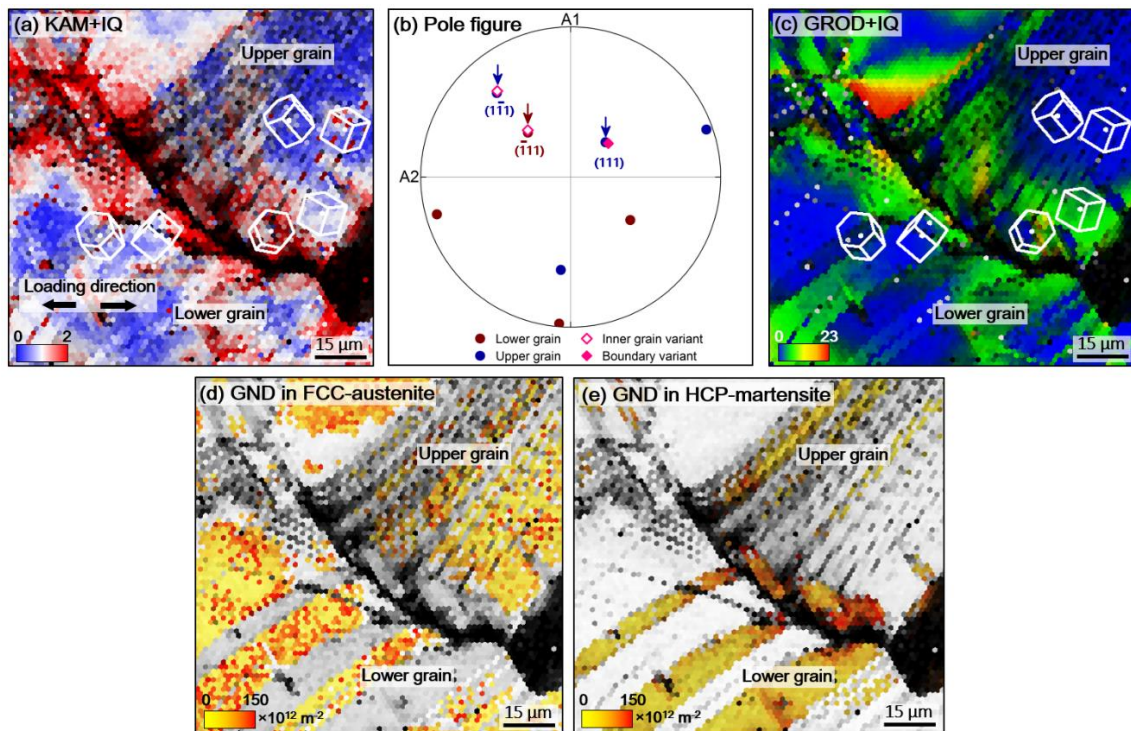
Figure 1.15: *In-situ* EBSD analyses of the monitored regime at a global stress level at 400 MPa. (a) KAM and IQ overlapped map; (c) pole figure for crystallographic orientation; (d) GROD and IQ overlapped map; (e) GND density in FCC phase; (f) GND density in HCP phase.

The foregoing results highlight the role of strain-induced martensitic transformation in the damage inception processes of metastable alloys. In the past decades, appreciable efforts have been achieved in the literature to optimize the microstructures of these metastable alloys, aiming to improve the damage

tolerance, and thereby the strength-ductility combination. While the detailed microstructure design approaches can be varied in different metastable alloy system, general strategies reported in the literature can be categorized into three respects:

(1) Texture optimization of the parent phase. This approach is exploited based on the anisotropy effect of crystallographic orientation, which can therefore affect the strain-induced martensitic transformation rate in response to external plastic straining. **Figure 1.16** presents one such investigations. In their study, Kang et al. [39] employed metastable lean duplex stainless steels with the same austenite (FCC-phase) phase fraction but distinctive texture therein by optimizing the thermomechanical processing conditions. The corresponding tensile response shows that by increasing the amount of $\{4\ 4\ 11\}\langle 11\ 11\ 8\rangle$ D-type texture component, the steepness of the inflection in the strain hardening rate (acquired by uniaxial tensile test) is reduced. Such a feature imply that the transformation rate of the metastable austenite is suppressed by crystallographic texture, which in turn increases the uniform elongation.
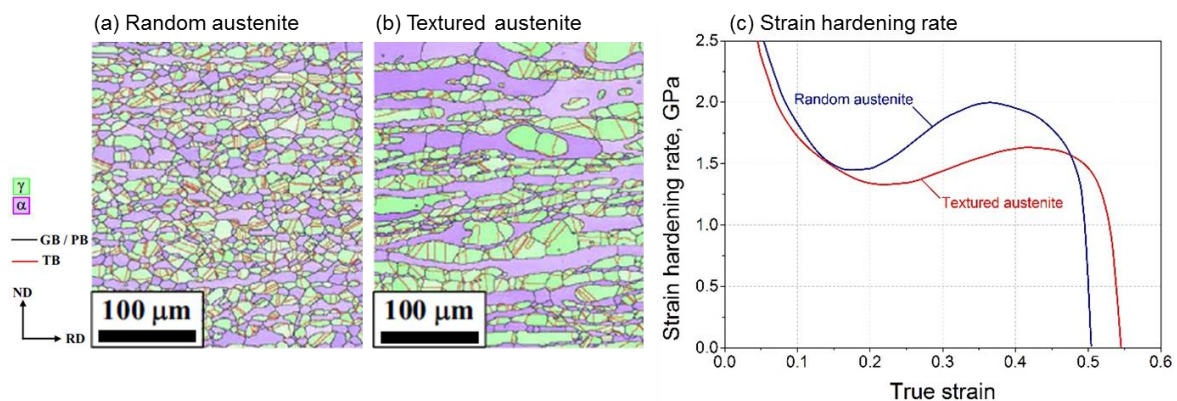
Figure 1.16: Crystallographic texture effect on strain-induced martensitic transformation rate. (a) Randomly orientated austenite; (b) textured austenite; (c) resultant strain hardening response [39].

(2) Grain size optimization of the parent phase. The fundamentals of this approach is based on the classical Hall-Petch strengthening concept, which predicts that parent phase with finer grain size will retard the transformation rate due to the increased yield strength. It can be therefore expected that if the parent phase grain size can exhibit a more disperse distribution, the burst-like feature of the strain-induced martensitic transformation can be mitigated and will then keep operating at the later stages of strain hardening. Following such a concept, Wang et al. [40] realized a "Spectral TRIP" microstructure in metastable FeMnNiAlC steels. By carrying out different cold-rolling and reversion treatment, they

realized a wider distribution of the parent austenite (FCC-phase) grain size (**Figure 1.17 (a)**). The corresponding uniaxial tensile response shows an evident improvement in yield strength, ultimate tensile strength, and fracture elongation (**Figure 1.17 (b)**).
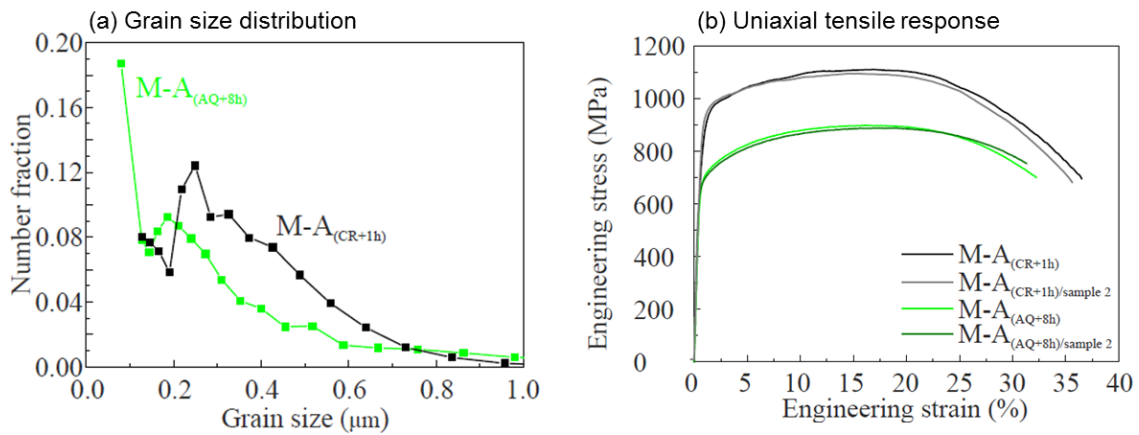
Figure 1.17: Grain size effect on strain-induced martensitic transformation. (a) Two types of grain size distribution in FeMnNiAlC steels; (b) the resultant uniaxial tensile response [40].

(3) Introduction of nano-sized precipitates. This microstructure design concepts focuses on diversifying the strengthening mechanisms of the metastable alloys. Raabe et al. [41] presented the feasibility to introduce $Ni_3(Ti,Al)$-type nano-sized precipitates (**Figure 1.18 (a)**) into the matrix of a low-alloyed metastable FeMnNiMoTiAl steels.
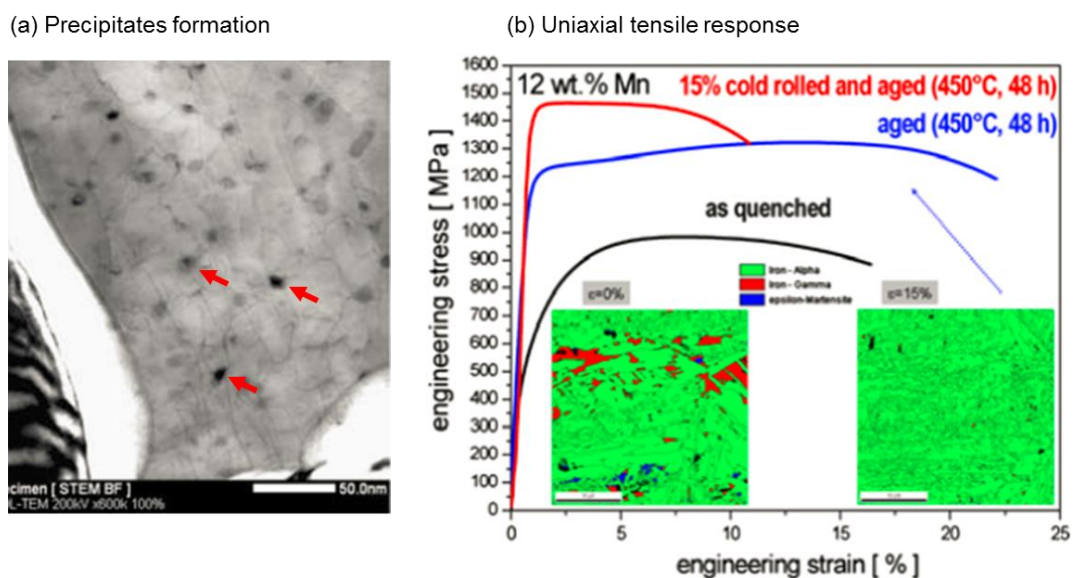
Figure 1.18: Nano-sized precipitation effect on strain-induced martensitic transformation. (a) $Ni_3(Ti,Al)$-type precipitates from ageing treatment; (b) the resultant uniaxial tensile response [41].

After intermediate temperature aging treatment, it is seen from the uniaxial tensile testing that compared with the as-quenched state, the aged condition reveals discernible increase in yield strength, ultimate tensile strength, and fracture elongation (**Figure 1.18 (b)**). It was also suggested that the ductilization mechanisms are although a combination of both strain-induced martensitic transformation and Orowan hardening. The latter, however, is more predominant as implied from the strain hardening rate calculation.

Section 1.3: Structure of the Thesis

Although the foregoing concepts have revealed great success metastable FCC alloy design, one fundamental limitation is still lacking of exploration: strain hardenability will be consumed with respect to the formation of the metastable parent phase. The formation of martensite, consequently leads to damage nucleation and micro-cracking. This thesis suggests that, in addition to the reported microstructural design concepts that are based on "existing presumptions", an alternative design space may also be perused: by studying the mechanical responses of existing metastable alloys in greater depths via *in-situ* experimentations. Then using the less-explored phenomena investigated as new guidance for microstructural design. Following this concept, the present thesis is developed as follows:

Chapter 2: Material and Methods. A systematic presentation of the material processing, characterization, and testing methods is revealed in this chapter.

Chapter 3: Phase Transformation-guided Design Strategies. Is it possible to realize suitable phase transformation in the strain-induced martensite such that its detrimental effect in damage tolerance can be mitigated? This chapter studies two possible pathways: first, plastic strain-driven FCC-HCP-FCC transformation; and second, thermally-driven HCP-FCC reverse transformation.

Chapter 4: Plasticity Micro-mechanism-guided Design Strategies. Is it possible to activate plausible deformation micro-mechanisms such that the blocky strain-induced martensite formation can be delayed? This chapter explores a potential solution via plastic deformation-induced stacking fault formation.

Chapter 5: Discussion and Future Directions. This chapter extends the discussion of **Chapters 3** and **4** and provides suggestions for future work.

Chapter 6: Conclusions. This chapter concludes the thesis.

Chapter 2: Material and Methods

Section 2.1: Alloy Fabrication

Alloys adopted in the present thesis were fabricated by vacuum arc melting from high purity raw elements purchased from Alpha Asear (at least 99.9 % purity). Vacuum arc melting was performed on an Edmund Bühler GmbH AM500 arc melter (**Figure 2.1 (a)**) during which a vacuum level of 5×10^{-5} mbar was reached. All the alloys were melted, flipped, then re-melted for at least five times to ensure homogeneity before being suction cast into rectangular geometries. These suction cast ingots were next subjected to thermomechanical processing. Most of the alloys (unless specified) were firstly subjected to cold-roll (using an IRM rolling mill, see **Figure 2.1 (b)**) down to 50 % thickness reduction, then sealed in quartz ampoules, for further homogenization treatment. The homogenized samples were further cold-rolled and recrystallized at different temperatures for suitable times to achieve the targeted grain sizes. Both recrystallization and homogenization processing were carried out under an Ar protective atmosphere so as to minimize oxidation. Since all the alloys employed in this thesis are interstitial-free, the scanning electron microscopy (SEM)-energy dispersive X-ray spectroscopy (EDS) methods were applied to check the actual composition after final recrystallization. Note that the Co-rich alloys studied in Chapter 4 of the thesis were acquired from Allegheny Technologies Incorporated (ATI), PA, USA.
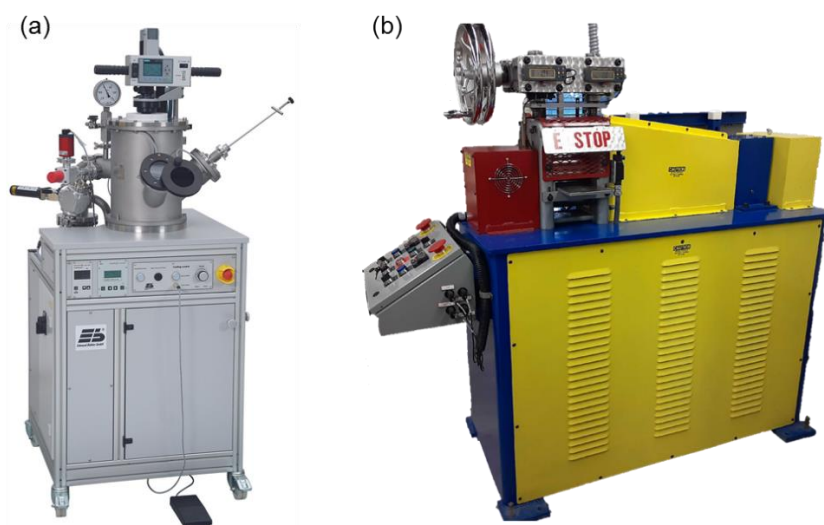
Figure 2.1: Major alloy processing tools employed in the present work. (a) The Edmund Bühler GmbH AM500 arc melter; (b) the IRM rolling mill with heating options.

Section 2.2: Electron Microscopy

Section 2.2.1: Scanning Electron Microscopy

All the meso-scale microstructural characterizations in this thesis were carried out in a TESCAN MIRA3 SEM equipped with electron backscatter diffraction (EBSD) and EDS detectors (**Figure 2.2**). Specimens for these analyses were prepared following the standard metallographic sample preparation routes: they were first sectioned from bulk ingots using wire electrical discharge machining (EDM) into small pieces, then mechanically ground on a series of SiC abrasive papers, polished using diamond suspension with particles sizes of 9 μm, 3 μm, and 1 μm. The final polishing was carried out using colloidal SiO_2 with ~40 nm diameter size. All the polished specimens were ultrasonically cleaned in acetone bath before testing.
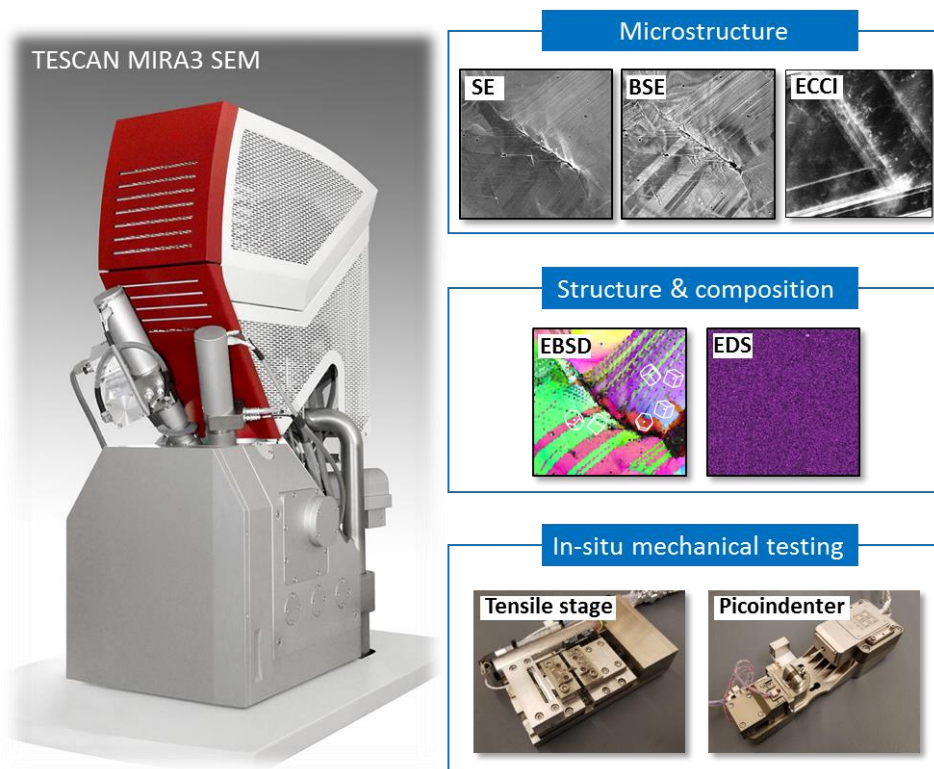
Figure 2.2: The TESCAN MIRA2 SEM system employed for microstructural characterization at the meso-scale

The EBSD raw diffractograms were collected using an EDAX Hikari EBSD camera at 20 kV acceleration voltage with a working distance of ~18.00 mm and a beam intensity of 16.0. The diffractograms were post-processed using an Orientation Imaging Microscopy (OIM) data-collection

software to acquire phase distribution and crystallographic information. *In-situ* EBSD diffraction data presented in Chapter 3 were acquired under 20 kV high voltage with 19.00 mm working distance and a step size of 1.5 μm (scanning area 270×270 μm^2). The geometrically necessary dislocation (GND) density shown in some of the results sections of Chapter 3 was computed using the algorithm reported by Pantleon [42] implemented in the OIM data processing software.

The EDS analyses were performed using an EDAX detector at ~15.00 mm working distance with 20 kV acceleration voltage and 16.0 beam intensity. To ensure a reliable elemental spatial distribution measurement, EDS acquisition parameters were chosen as 512×512 pixel^2 over 40×40 μm^2 area with a 64-frame binning setting. These parameters, according to our previous studies [43,44], are sufficient to identify spatial composition inhomogeneity done to ~1 μm length scale.

Deformation substructures and defects evolution characteristics were studied using the electron channeling contrast imaging (ECCI) technique. The ECCI micrographs were acquired at a ~7.00 mm working distance with 20 kV acceleration voltage and 16.0 beam intensity using the backscatter electron (BSE) signal. For some area, in order to find the optimal channeling condition for imaging, sate rocking and rotating were carried out. The diffraction information of the area subjected to ECCI analyses were acquired by EBSD, following by crystallographic calculation detailed in later section.

Section 2.2.2: Scanning Transmission Electron Microscopy

To further explore the atomistic details for phase transformation and plastic deformation, scanning transmission electron microscopy (STEM) was employed in the present study. In this thesis, to realize site-specific characterizations, Specimens for STEM analyses were prepared by a Raith VELION focused ion beam (FIB)-SEM system utilizing a Au$^+$ source. The initial FIB milling of the lamella was done with a 35 kV Au$^+$ beam and the final polishing process was accomplished using 5 kV Au$^+$. The FIB lift-out region was identified by EBSD in the TESCAN MIRA3 SEM following the methods detailed before. To further polish the FIB lamellar and achieve electron transparency, the sample was single-sector ion-milled [45] using an Ar$^+$ ion beam at 0.3 and 0.1 kV for 3 minutes.. High-angle annular dark-field (HAADF) STEM images were acquired with a Thermo Fisher Scientific Themis Z probe aberration-corrected STEM at 200 kV using a beam current of 30 pA, convergence angle of 19.2 mrad,

and collection semi-angle range of 65-200 mrad. All the HAADF-STEM images were drift-corrected using a Revolving STEM (RevSTEM) method [46,47]. Geometric phase analysis [48] for atomistic strain calculation was accomplished using a Strain++ open-access software (https://jjppeters.github.io/Strainpp/).

Section 2.3: Mechanical Testing

Section 2.3.1: *Ex-situ* Testing with Optical Digital Image Correlation

Ex-situ uniaxial tensile was carried out on a Deben-Gatan micro-mechanical testing platform equipped with an optical camera for digital image correlation (DIC) analyses (**Figure 2.3**). Rectangular dog bone-shaped tensile specimens (gauge dimension: $6.5 \times 2.5 \times 1.0$ mm^3) were sectioned along the rolling direction (RD) of the bulk alloy sheet or ingot using electrical discharge machining (EDM). These specimens were then subjected to mechanical grinding up to #1200 SiC abrasive paper before being speckle patterned for DIC measurement.
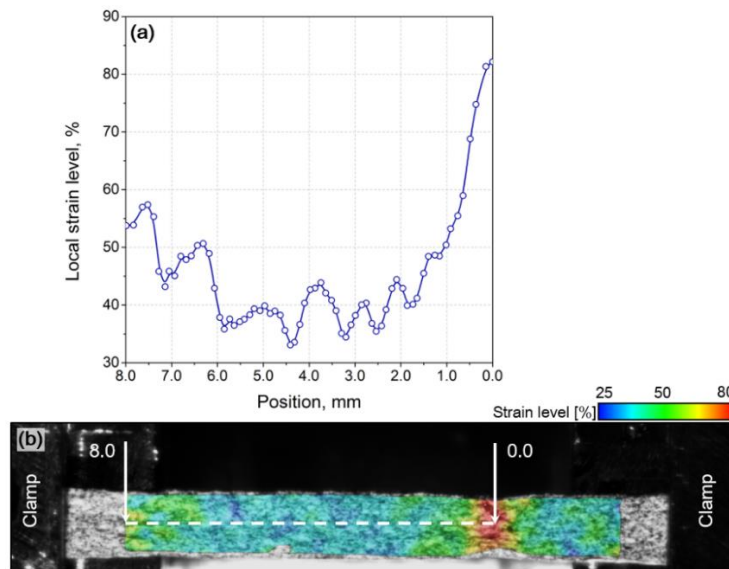
Figure 2.3: Representative *ex-situ* tensile experimental results with optical DIC. (a) Line profile of local strain evolution; (b) two-dimensional strain distribution acquired at one frame before fracture (acquisition frequency: 500 ms per frame).

These samples were then deformed to fracture under a quasi-static loading condition (strain rate: 10^{-3} s^{-1}), during which optical images were recorded every 500 ms for strain profile assessment in a GOM software (https://www.gom.com/3d-software/gom-correlate.html). In the optical DIC analysis, the ε_{xx} engineering strain component (parallel to the loading axis) was utilized to represent the local strain through the gauge section of the tensile specimen. A virtual extensometer was adopted in the DIC analyses to measure the elongation for obtaining the engineering stress-strain curve. The spatial resolution of the optical DIC utilized in these measurements is ~140 pixel/mm. Square facet size and inter-facet distance employed in the strain calculation are ~0.14 mm (20 pixel) and ~0.07 mm (10 pixel).

Section 2.3.2: *In-situ* Microstructure-based Strain Mapping

An *in-situ* microstructure-based digital image correlation approach (hereafter referred was micro-digital imaging correlation, μ-DIC) [49] was employed to quantitatively assess the heterogeneous strain accommodation and evolution during plastic deformation. Following our previous experimental recipes [50–52], speckle patterns were coated on mirror-finished tensile specimens (gauge dimension kept the same as ex-situ testing) by using ~40 nm diameter colloidal SiO_2. These coated specimens were then dried in flow air with sprayed ethanol to achieve desirably homogenous patterns (see **Figure 2.4 (a)-(c)**). During the in-situ tensile experiment, BSE, SE, in-beam BSE, and in-beam SE micrographs with 4096×4096 resolution (roughly 50×50 μm^2 field of view) were recorded every 1.0-1.5% engineering strain incrementation, and the in-beam SE micrographs were subjected to DIC calculation for strain determination in a commercial GOM software (https://www.gom.com/en/products/gom-correlate). The square facet size applied for DIC analysis was 60 pixel, giving rise to a spatial resolution of about 600 nm, and the inter-facet distance was set as ~200 nm, in equivalent to 20 pixel under the current imaging condition. Since the local strain value determined from DIC analysis may exhibit a dependency on the applied subset size, we have validated that the adopted 60 pixel (in equivalent, about 600 nm) subset size exhibits negligibly small influence in the strain calculation results.

Because of the quantitative analyses in the present work involve strain profile acquisition along certain directions as well as distribution assessments, and the physical conclusions drawn should be frame-indifferent [53], the von Mises equivalent strain is therefore adopted. Considering the thin-sheet geometry of the present tensile specimen (thickness ~1.0 mm), a plane stress approximation was applied, which states:

$$\boldsymbol{\varepsilon}_p = \frac{1}{2}[\nabla \mathbf{u} + (\nabla \mathbf{u})^T] \simeq \begin{bmatrix} \varepsilon_{xx} & \varepsilon_{xy} & 0 \\ \varepsilon_{xy} & \varepsilon_{yy} & 0 \\ 0 & 0 & -\varepsilon_{xx} - \varepsilon_{yy} \end{bmatrix} \tag{2.1}$$

In **Eq. (2.1)**, $\boldsymbol{\varepsilon}_p$ is the plastic strain tensor under the plane-stress presumption, $\mathbf{u}$ represents the displacement field which is measured by μ-DIC. The out-of-plane strain component ε_{zz}, was determined using the principle of volume constancy: $\mathrm{tr}(\boldsymbol{\varepsilon}_p) = 0$. The von Mises equivalent strain, which is then an in-plane frame-indifferent scalar, is calculated by:

$$\varepsilon_{VM} = \sqrt{\frac{2}{3} \boldsymbol{\varepsilon}_p : \boldsymbol{\varepsilon}_p} \qquad (2.2)$$

Note that, since the present study primarily concerns about deformation at relatively high plastic strain levels, the elastic compressibility of the present alloy would then have negligible effect on most of the results. However, in the elasto-platic transition region (for example strain maps taken right after yielding), the corresponding result may contain a relatively high portion of elastic strain.
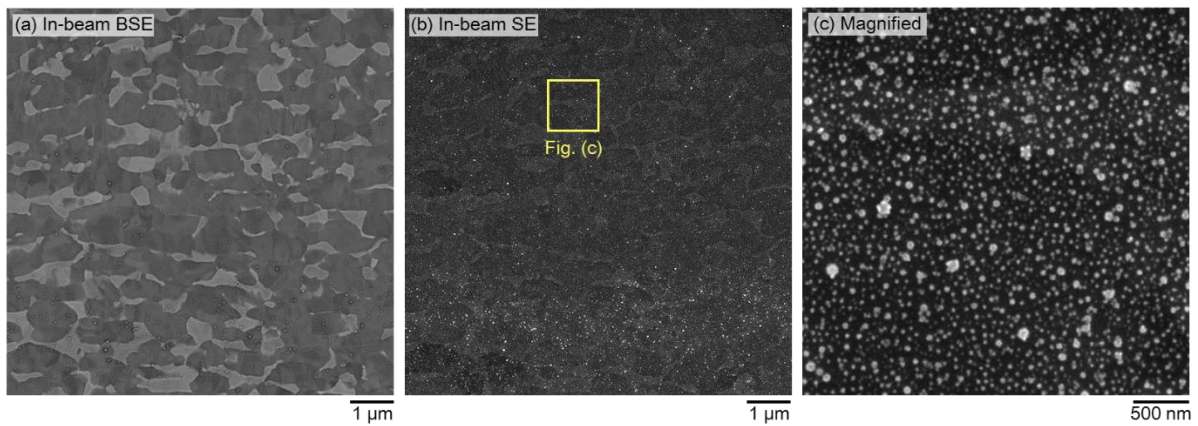
Figure 2.4: Exemplary speckle patterns prepared for *in-situ* strain mapping. (a) In-beam BSE micrograph for morphological observation; (b) in-beam SE micrograph for digital image correlation investigation; (c) magnified in-beam SE micrograph showing the homogenous SiO_2 speckle particle distribution.

Section 2.4: Synchrotron X-ray Diffractometry

To quantitatively analyze the phase constitution change as well as the defect content evolution during plastic deformation, synchrotron X-ray diffraction experimentation was employed for both spot and *in-situ* measurement. All the synchrotron X-ray experiments were performed at beamline ID 11-C, Argonne National Laboratory, Chicago, U.S.A. The following **Figure 2.5** schematically illustrates the experimentation for *in-situ* tensile testing: dog bone-shaped specimen with a gauge geometry of $8.0 \times 2.0 \times 1.5$ mm^3 was subjected to quasi-static tensile loading (strain rate: 1×10^{-3} s^{-1}) under high-energy synchrotron X-ray radiation (wavelength: 0.1173 Å).
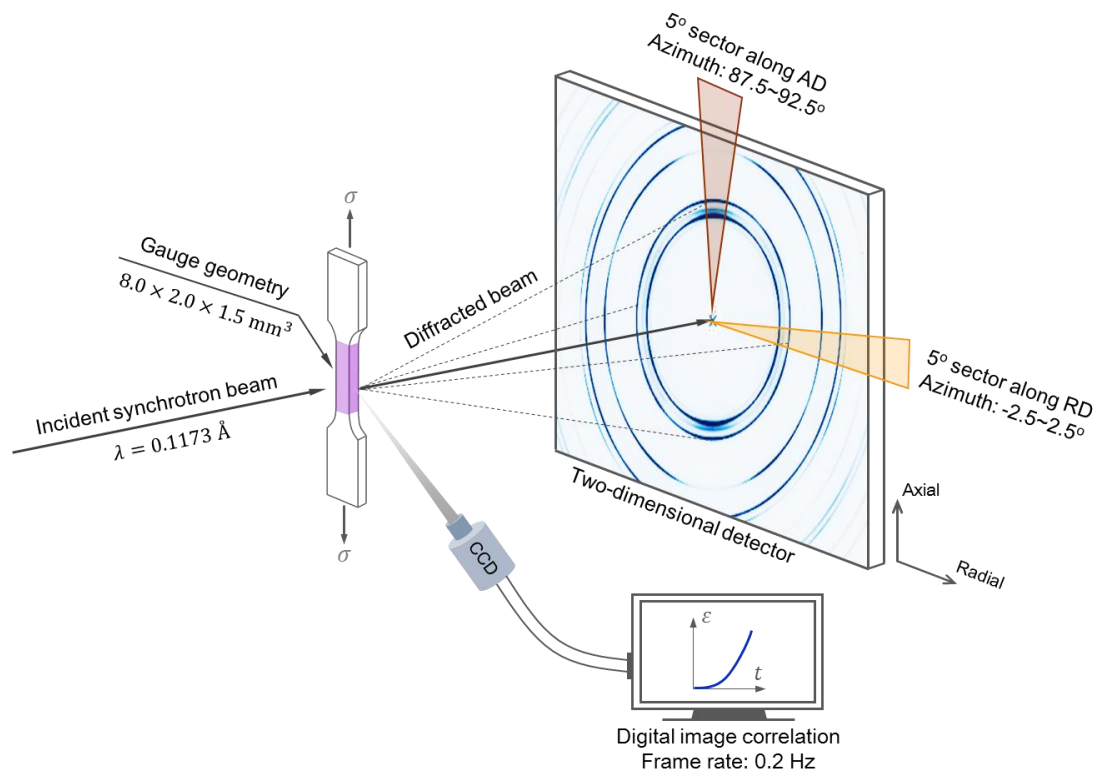
Figure 2.5: Schematic for the in-situ synchrotron X-ray diffraction experimentation and the acquisition for axial and radial diffraction patterns.

Optical DIC technique with an acquisition frame rate of 0.2 Hz was employed to ensure a precise strain measurement and thereby the calculation of strain hardening rate as well as strain hardening exponent. During the deformation procedure, two-dimensional diffractograms were recorded every 1.0 % engineering strain incrementation until fracture. To unambiguously characterize the lattice strain evolution [54–56], the two-dimensional diffractograms were sectioned with a 5 degree sector

respectively along axial (parallel to the loading axis) and radial (perpendicular to the loading axis) directions before being integrated as a function of the corresponding azimuth angles. The integrated peaks were subsequently Rietveld-fitted using GSAS-II [57] and MATLAB software for determining quantitative parameters for further mechanistic explorations. The instrumental broadening was calibrated using the diffraction results of NIST-standard CeO_2 powders.

Section 2.5: Other Experimentations and Theoretical Calculations

Section 2.5.1: Differential Scanning Calorimetry

In order to track the onset temperature of reverse austenitic transformation of the strain-induced martensite, differential scanning calorimetry (DSC) method was employed. The DSC measurements were carried out on a TA Instruments Q100 DSC. Rectangular specimens (dimension: $1.5 \times 1.5 \times 0.8$ mm^3 small pieces) were sectioned from the deformed alloy using electrical discharge machining. Alumina crucibles were utilized for the measurement and the baseline was corrected using empty Alumina crucibles.

Section 2.5.2: Schmid Factor Calculation and Slip Trace Analyses

To identify the operating slip system (or martensitic variant) during plastic deformation slip trace analyses and Schmid factor calculation were carried out via a home-built STrCryst program (https://github.com/shaolouwei/STrCryst, solely developed by the author of this thesis) in which the theoretical slip trace was calculated as [51]:

$$\mathbf{t} = (\boldsymbol{G}^{-1} \cdot \mathbf{n}) \times \mathbf{N} \tag{2.3}$$

where $\mathbf{n}$ and $\mathbf{N} = [001]$ denote the unit slip/twin (crystal frame) and observant plane (specimen frame) normals, and $\boldsymbol{G}$ represents the coordinate transformation matrix [58]:

$$\boldsymbol{G} = \begin{bmatrix} \cos\varphi_1\cos\varphi_2 - \sin\varphi_1\sin\varphi_2\cos\phi & \sin\varphi_1\cos\varphi_2 + \cos\varphi_1\sin\varphi_2\cos\phi & \sin\varphi_2\sin\phi \\ -\cos\varphi_1\sin\varphi_2 - \sin\varphi_1\cos\varphi_2\cos\phi & -\sin\varphi_1\sin\varphi_2 + \cos\varphi_1\cos\varphi_2\cos\phi & \cos\varphi_2\sin\phi \\ \sin\varphi_1\sin\phi & -\cos\varphi_1\sin\phi & \cos\phi \end{bmatrix} \tag{2.4}$$

In **Eq. (2.4)**, $(\varphi_1, \phi, \varphi_2)$ are Euler angles following the Bunge's convention [58] that can be exported for certain microstructural constituents from the corresponding EBSD measurements. It should be noted that for HCP-phases an additional coordinate transformation is needed before using **Eq. (2.3)** for trace analyses. Vector $[u\,v\,t\,w]$ on $(h\,k\,i\,l)$ plane expressed in hexagonal coordinate is transformed to Cartesian coordinate via [58]: $[u'\,v'\,w'] = [(2u+v)\sqrt{3}/2 \quad 3v/2 \quad wr_{c/a}]$ and $(h'\,k'\,l') = ((2h+$

$k)\sqrt{3}/3 \quad k \quad l/r_{c/a}$). The c-to-a ratio ($r_{c/a}$) for the HCP-phase is determined using synchrotron X-ray diffractometry detailed in the previous section. Owing to the fact that surface quality may potentially bring about artifacts (e.g. surface scratches from specimen preparation) to the slip trace analysis, the presence of slip trace was verified by step-wise titling the specimen for ±15º. It is also noted that a ±10º alignment deviation tolerance [51,59] was applied when comparing the actual and the theoretical slip traces.

To assess the crystallographic propensity for the activation of individual slip (or martensitic transformation) systems, Schmid factor calculation were also carried out:

$$SF = (\boldsymbol{G} \cdot \boldsymbol{\sigma}) : (\mathbf{n} \otimes \mathbf{s}) \tag{2.5}$$

Here, $\boldsymbol{\sigma}$ and $\boldsymbol{G}$ represents the imposed stress tensor (rank two) and the coordinate transformation matrix defined by **Eq. (2.4)**. $\mathbf{n} \otimes \mathbf{s}$ is the Schmid tensor (rank two), in which $\mathbf{n}$ and $\mathbf{s}$ are the unit vectors of slip plane normal and slip direction. The present thesis presumes a far-field approximation of the stress state, i.e. uniaxial tension. Therefore, **Eq. (2.5)** can be simplified done to a vector form:

$$SF = [(\boldsymbol{G} \cdot \mathbf{f}) \cdot \mathbf{n}] \cdot [(\boldsymbol{G} \cdot \mathbf{f}) \cdot \mathbf{s}] \tag{2.6}$$

In **Eq. (2.6)**, $\mathbf{f} = [010]^{\mathrm{T}}$ represent the uniaxial tensile loading following the coordinate system of TESCAN MIRA 3. When using **Eq. (2.6)**, $\mathbf{n}$ is firstly identified by trace analysis, and $\mathbf{s}$ is then considered by including all possible slip directions on the identified slip plane.

Programing and graphical user interface of the calculation described in this section were both developed in MATLAB. At the end of the thesis, some portions of the critical codes are provided.

Chapter 3: Phase Transformation-based Solutions

Portions of this chapter are based on:

[1] S.L. Wei et al., Plastic strain-induced sequential martensitic transformation. **Scripta Materialia**, 2020, 185: 36-41.

[2] S.L. Wei et al., Tuning mechanical metastability in FeMnCo medium entropy alloys and a peek into deformable hexagonal close-packed martensite, **Applied Physics Letters**, 2021, 119: 261905.

[3] S.L. Wei et al., Interstitial-free bake hardening realized by epsilon martensite reverse transformation. **Metallurgical and Materials Transactions A**, 2019, 50: 3985-3991.

Section 3.1: Motivations

The primary objective of this chapter is to explore phase transformation-based microstructural design strategies, aiming to enhance the mechanical performances of concentrated metastable FCC alloys. As discussed in Chapter 1, one of the major features of HCP-martensite lie in its similar atomic stacking sequence compared with the parent FCC-phase. Such a characteristic brings about two important microstructural consequences upon the strain-induced FCC-HCP transformations: first, near-coherent interfacial structures with desirable mobility; and second, more moderate plastic accommodation in the untransformed FCC region. Because of these, the following two phase transformation based microstructural design approaches are therefore conceptualized and revealed in detail in the proceeding sections:

First, to activate further displacive phase transformations *by plastic loading* for the strain-induced HCP-martensite (Section 3.2). It is anticipated that through this kind of additional phase transformation, the strain-induced HCP-martensite can further accommodate plastic strain, however, without forming highly defected BCT-structured martensite.

Second, to "remove" strain-induced HCP-martensite *by thermal annealing,* intending to activate an HCP-FCC reverse transformation (Section 3.3). The objective of this approach is enlightened by the bake hardening treatment commonly applied in interstitial-strengthened alloys. However, the target here is to promote the increase of both ultimate tensile strength and cumulative elongation.

Section 3.2: Plastic Strain-driven FCC-HCP-FCC Sequential Transformations

Section 3.2.1: Results

The alloy involved in this Section is a quaternary $Fe_{45}Mn_{35}Co_{10}Cr_{10}$ at. % CCA, of which the undeformed microstructure is shown in **Figure 3.1 (a)** and **(b)**. EDS elemental mapping results suggest that the four principal alloy elements demonstrate uniform distributions across grain boundary (**Figure 3.1 (c1)-(c4)**). *Ex-situ* uniaxial tensile testing (**Figure 3.1 (d)**) reveals a yield strength of ~155 MPa and a significant strain hardenability, leading to an ultimate tensile strength of ~568 MPa and a fracture elongation of ~51 %. Note that the discernable inflection in the strain hardening rate curve indicates the activation of plastic-strain induced FCC-HCP transformation in the present alloy. To further investigate the detailed phase transformation processes during plastic deformation, *in-situ* SEM/EBSD studies were carried out.
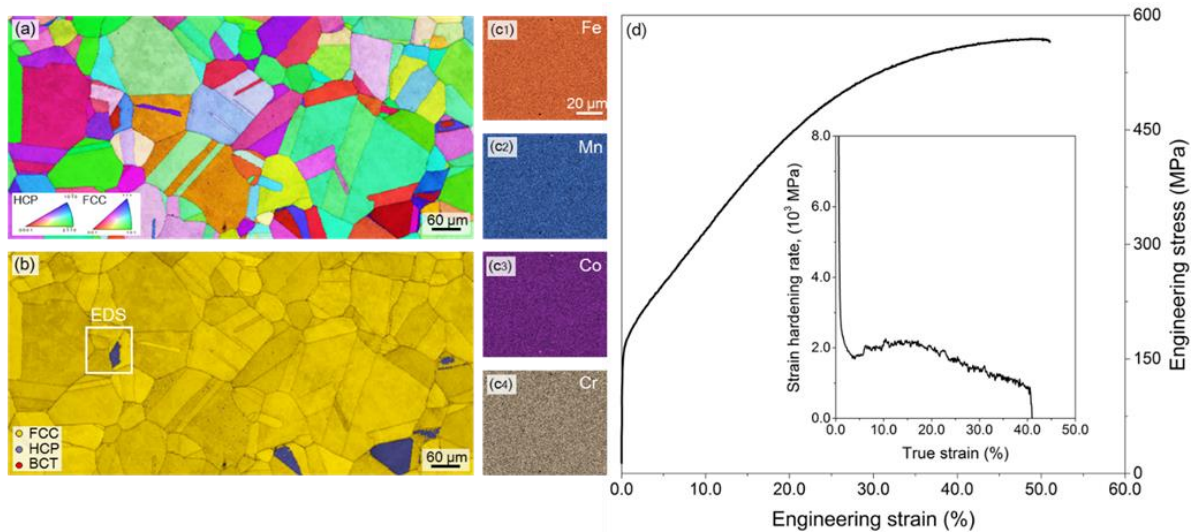
Figure 3.1: Microstructure and uniaxial tensile properties of the quaternary $Fe_{45}Mn_{35}Co_{10}Cr_{10}$ alloy. (a) EBSD inverse pole figure (IPF); (b) phase map; (c1)-(c4) elemental distribution of Fe, Mn, Co, and Cr; (d) engineering stress-strain curve ($\dot{\varepsilon} = 10^{-4}$ s^{-1}) with strain hardening rate chart inserted.

In-situ BSE/EBSD micrographs in **Figure 3.2 (a)-(f)** reveal the phase constitution evolution with increasing deformation level. At a global stress of 200.6 MPa, the monitored microstructure undergoes a strain induced FCC→HCP martensitic transformation (MT), resulting in a brighter orientation contrast (**Figure 3.2 (a)**). Upon further straining, both Regions 1 and 2 witness the same type of MT, forming a

~10 μm width HCP-martensite band (**Figure 3.2 (b)**). As global stress increases up to 368.7 MPa, these two regions demonstrate different micro-events: a spindle-shaped topography appears in Region 1, proved by EBSD phase map (**Figure 3.2 (c1)**), exhibiting an FCC structure, while HCP-martensite in Region 2 only thickens. This sort of clear distinctions in phase constitution evolution confirm that apart from the conventional FCC→HCP MT, a follow-up HCP→FCC MT is also activated in the present alloy, realizing a sequential FCC→HCP→FCC MT. Note the fact that the specimen is being constantly deformed in the plastic regime and the differences in crystallographic orientation between the newly formed FCC-phase and its parent counterpart (**Figure 3.2 (c3)**) clearly distinguish the sequential MT from classical stress-assisted reversible MT documented in pseudo-elastic materials where the removal of external load is indispensable [60–62]. Upon elevating global stress levels further (**Figure 3.2 (d)-(f)**), the sequential MT is also observed at multiple sites within the prior HCP-martensite bands (red arrows), during which no cracking presents, eliminating the potential interference from local unloading.
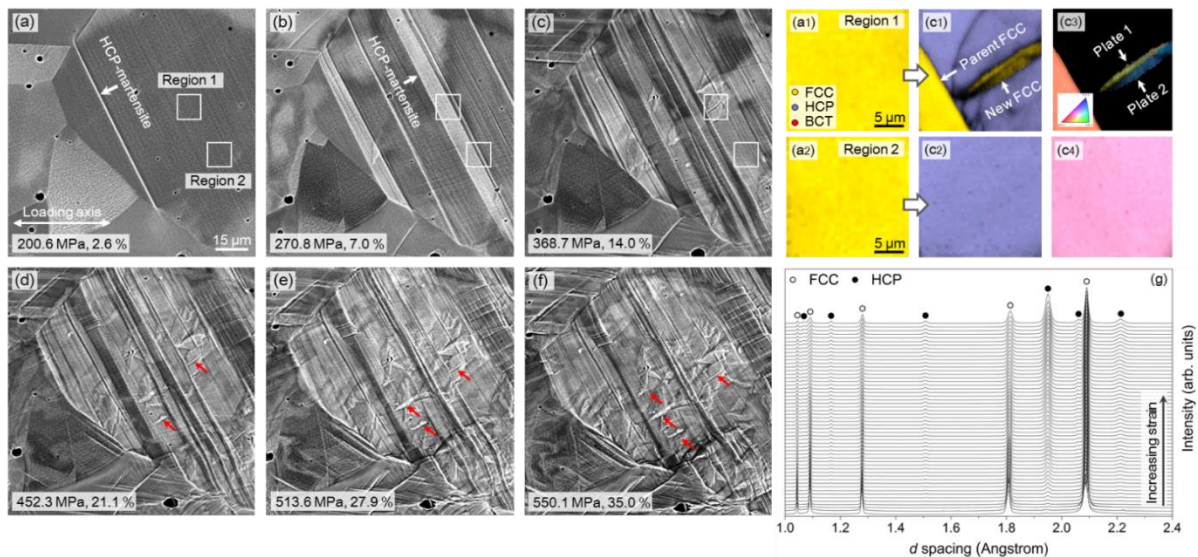
Figure 3.2: *In-situ* **observation of sequential FCC→HCP→FCC martensitic transformation.** (a)-(f) SEM micrographs for microstructural evolution at increasing deformation level; (a1), (a2), (c1), and (c2) EBSD phase maps for Regions 1 and 2; (c3) and (c4) the corresponding IPFs; (g) synchrotron X-ray diffractograms taken with 1 % engineering strain increment. To ensure clarity, high-magnification EBSD phase maps and inverse pole figures (IPF) are presented for two specific areas denoted as "Regions 1 and 2" in (a).

To further validate that this unique MT pathway does not involve any potential intermediate state [23,63], tensile experiments were also performed under synchrotron X-ray radiation. Diffractograms in

Figure 3.2 (g) reveal that in the undeformed state, the examined alloy consists of a major FCC-phase (~98 %) and minor amounts of thermally-induced HCP-phase (~2 %). Lattice constants for FCC and HCP-phases are determined as $a_{FCC} = 3.6140\,\text{Å}$ (undeformed), $a_{HCP} = 2.5524\,\text{Å}$, $c_{HCP} = 4.1445\,\text{Å}$ (~1 % strain). When applied stress increases, characteristic diffraction peaks for the HCP-phase arise and their intensities witness an increasing trend until fracture. Throughout the whole testing realm, neither additional peaks corresponding to a transitional structure nor FCC peak splitting is detected. These results are consistent with the *in-situ* SEM/EBSD observations, suggesting that the sequential MT is realized without the aid of any intermediate phase, and that the end product preserves the symmetry of the parent FCC-phase, but exhibiting a different crystallographic orientation. To further assess this kind of characteristic, we present in **Figure 3.3** detailed crystallographic characterizations of the region that undergoes sequential MT.
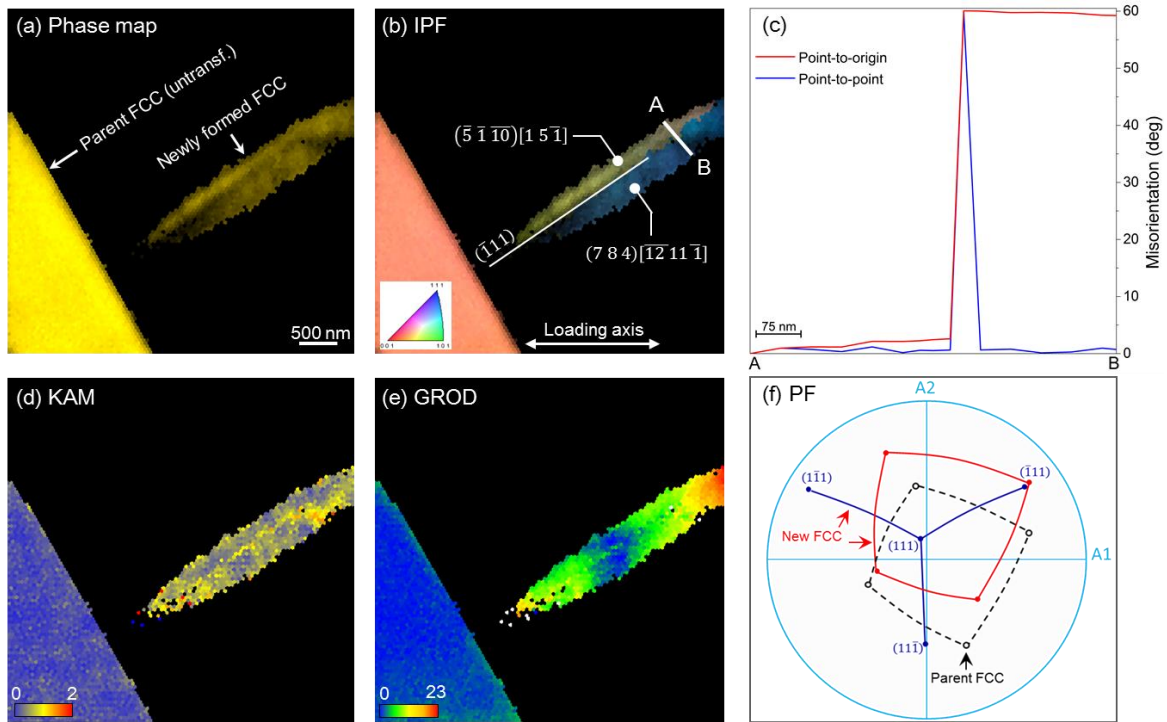
Figure 3.3: Crystallographic assessments of the sequential martensitic transformation region. (a) Phase map; (b) IPF; (c) and (f) confirmation of twin relationship and the presence of $\Sigma 3$ boundary; (d) and (e) kernel average misorientation (KAM) and grain reference orientation deviation (GROD) maps

It is seen from the IPF in **Figure 3.3 (b)** that the newly formed FCC phase exhibit a completely different crystallographic orientation relationship compared with the parent FCC-phase. **Figure 3.3 (b), (c),** and **(f)** confirms twin relationship and the presence of $\Sigma 3$ boundary within the newly formed FCC phase.

In addition, KAM and GROD maps demonstrated in **Figure 3.3 (d)** and **(e)** validate the occurrence of extensive plastic deformation [50] within the FCC phase formed through the sequential MT. To further explore the phase transformation processes, we next analyzed the phase fraction evolution during plastic deformation.

Assessments of phase fraction evolution analyzed from *in-situ* synchrotron diffraction and SEM/EBSD experiments are shown comparatively in **Figure 3.4**. In both cases, the HCP-phase fraction reveals a monotonic increasing trend with the elevating applied stress. Unlike previous experimental observations [29,34,64–66] and theoretical predictions [67–69] of strain-induced martensite formation kinetics in classical metastable alloys, synchrotron X-ray diffractograms reveal a clear inflection at a stress level of ~220 MPa in the HCP-phase fraction evolution curve follows by a plateau-like region terminating at ~300 MPa (**Figure 3.4 (a)**). The most plausible reason for such a momentarily stunted FCC→HCP transformation rate is that the formation of new FCC-phases exhibits a burst-type of nucleation but negligible growth kinetics. This says, at a certain applied stress level, large amounts of new FCC-phases will abruptly nucleate due to the HCP→FCC MT, which would as a net result, mitigate the nominal HCP-phase fraction increase. Because of the strong mechanical confinement from the adjacent prior HCP-martensite (**Figure 3.2 (c)**), these newly formed FCC-phases can scarcely thicken, and upon the consumption of all potential nucleation sites, their total fraction will reach to a stable extent, resulting in the expedited increase of nominal HCP-phase fraction. Microstructure-based phase fraction analysis (**Figure 3.4 (b)**) also confirms that the FCC-phase resulting from the sequential MT, although low in amount, indeed exhibits an incremental growth in its fraction until necking or macroscopic failure terminate the deformation. Note that this kind of almost linearly increasing new FCC-phase fraction seen in **Figure 3.4 (b)** is mostly ascribed to the fact that the corresponding nucleation procedure has not exceeded its saturation state before the incipience of plastic instability.

To explore whether this sequential MT can be activated to realize even higher FCC-phase fraction when plastic instability can be delayed or even prohibited, we have carried out a separate set of high-pressure torsion experiments where larger amounts of shear deformation can be imposed on the specimens. BSE micrographs (**Figure 3.5**) acquired at a local equivalent strain level of 42.5 % (kept equal to the fracture true strain during uniaxial tensile deformation) confirms that the presence of larger amounts of new

FCC-phase forming both within and at the junction of HCP-martensite bands (**Figure 3.5 (b)** and **(c)**).
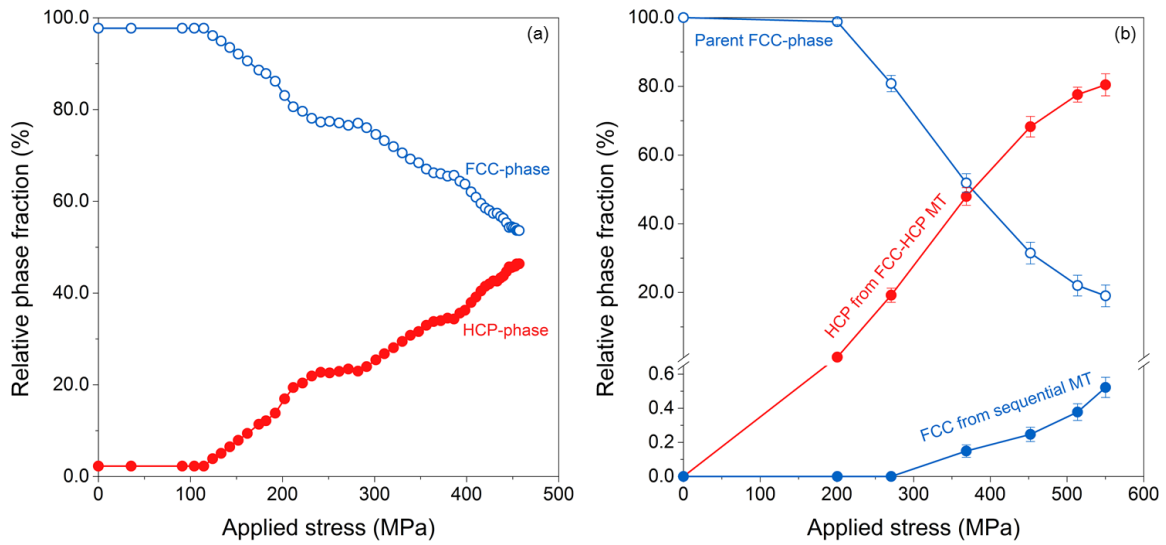
Figure 3.4: Phase constitution evolution as a function of increasing applied stress. (a) Results analyzed from *in-situ* synchrotron X-ray diffractograms; (b) results analyzed from *in-situ* SEM/EBSD experiment.
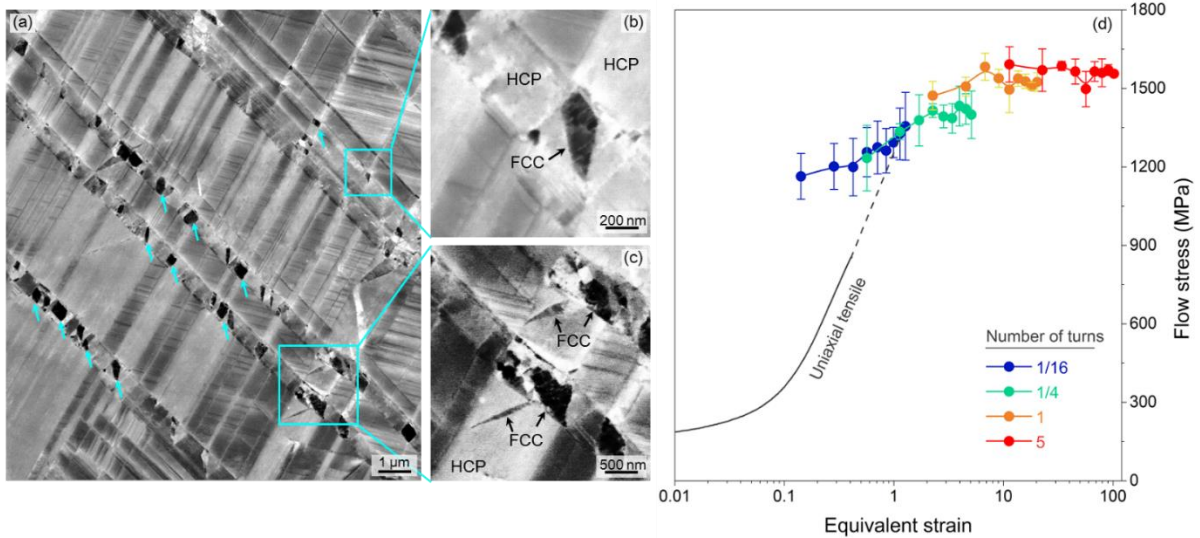
Figure 3.5: **Microstructure of the Fe$_{45}$Mn$_{35}$Co$_{10}$Cr$_{10}$ alloy underwent high-pressure torsion deformation.** (a) SEM micrograph taken at a local equivalent strain level of ~42.5 %; (b) electron channeling contrast imaging demonstrates the extensive dislocation density within the newly formed FCC phase; (c) magnified image showing the nucleation of new FCC-phase both within and at the junction of HCP-martensite bands; (d) derived flow stress evolution with respect to increasing torsion deformation.

Next, we focus on meso-scale strain evolution associated with the sequential MT. For clearer representations, only the transverse component (vertical to the loading axis) of the strain field (ε_y) is

depicted in **Figure 3.6 (a)-(d)**. As seen in the transverse strain maps where the global strain develops from 4.3 to 22.2 % (**Figure 3.6 (a)-(d)**), regions where sequential MT is activated exhibit pronounced localized compressive strain: ε_y reaches -8.9 % at 22.2 % global strain (see **Figure 3.7 (c)**). In contrast, lower compressive strains (-2.0~-3.0 % in ε_y) are generated in the rest of the microstructure that only undergoes FCC→HCP MT. Such distinctions indicate an eminent difference in compressive strain accommodation between FCC→HCP and HCP→FCC MTs, again suggesting that the latter MT is not accomplished by replicating the strain trajectory of the former one in reverse. Atomistic mechanisms regarding this sequential MT will be elaborated in detail below.
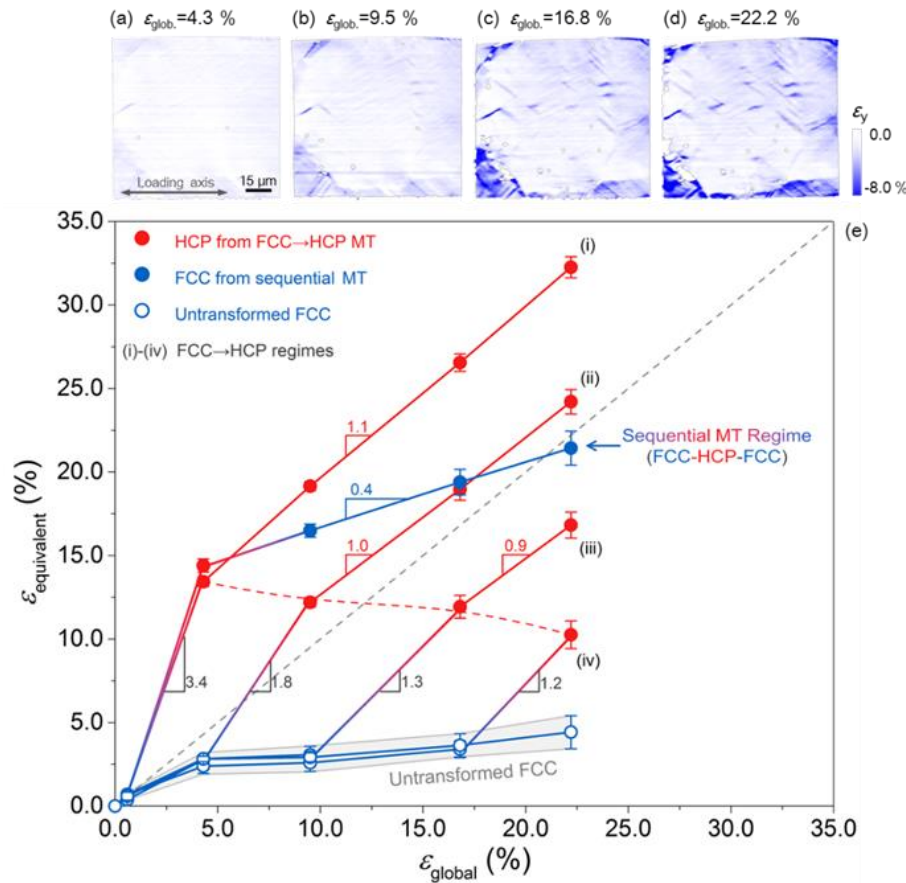
Figure 3.6: Microstructural-based strain evolution assessment. (a)-(d) transverse component of the two dimensional strain field calculated from displacement correlation algorithm; (e) site-specific local von Mises strain evolution with respect to increasing global strain level.

Figure 3.6 (e) provides the calculated von Mises equivalent strain ($\varepsilon_{equivalent}$) evolution with respect to increasing global strain (ε_{global}) for all microstructural constituents, including:

(1) untransformed FCC-phase regions;

(2) regions solely undergoing FCC→HCP MT;

(3) specific sites at which sequential MT takes place.

Note that this plot should be distinguished from the classical strain partition assessment plots in which phase constitution change is typically not considered [70,71]. Due to the asynchronous activation of various plastic deformation modules, four specific regions (marked as (i)-(iv)) where FCC→HCP MT takes place successively at various ε_{global} levels are also presented to eliminate the interference from strain accommodation through perfect dislocation glide in the parent FCC-phase.

At a global strain level of 4.3 %, FCC→HCP MT is activated within Region (i), leading to a drastic $\varepsilon_{equivalent}$ increase to ~13.4 %, suggesting the significant role of martensitic transformation strain in facilitating local plastic deformation. By comparing such transformation strains in Regions (i)-(iv), it can be concluded that although perfect dislocation glide-induced strain hardening in the parent FCC-phase imposes a slight suppression effect on transformation strain (the dashed red line and the indicated slope changes amongst (i)-(iv)), it is still the FCC→ HCP MT that acts as the major plastic strain carrier.
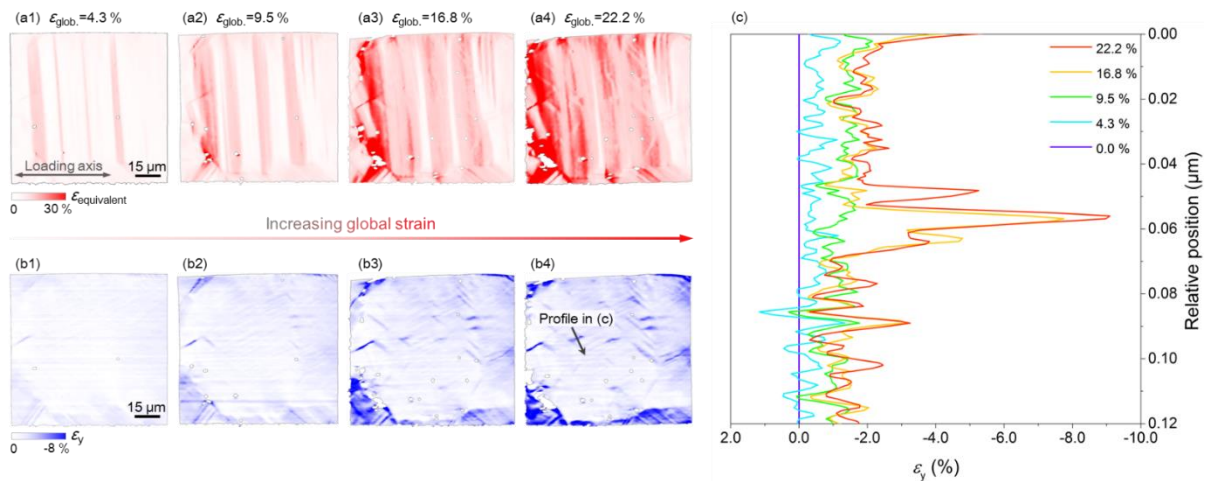
Figure 3.7: Complementary strain distribution analyses. (a1)-(a4) Von Mises equivalent strain evolution with respect to increasing global strain; (b1)-(b4) the corresponding transverse strain maps; (c) line profile along a specific site validating the pronounce compressive strain associated with the FCC→HCP→ FCC sequential martensitic transformation.

As global strain increases, the transformation product, HCP-martensite, subsequently reveals two kinds of local strain evolution characteristics depending on different deformation micro-events: In some regions HCP exhibit dislocation glide (portions extending further from the red dashed line). Here, the

slopes witness a slight drop down to ~1.0 (compared to the slopes during FCC→ HCP MT), suggesting an enhanced plastic deformation resistance. Yet, within regions (i)-(iv), $\varepsilon_{equivalent}$ values yield a linear-like increasing trend as a function of elevating global strains;

In other regions, HCP→FCC MT takes place. Here, the most significant slope inflection from 3.4 to 0.4 is observed, and the corresponding $\varepsilon_{equivalent}$ also exhibits the most moderate monotonic increase. These distinctions highlight the following implications regarding the sequential MT:

(1) the final transformation product, the FCC-phase, unlike typical BCT-phase that shows brittle-like characteristics [72,73], is able to realize further strain accommodation as deformation proceeds;

(2) this sort of final FCC-phase possesses the most exceptional resistance to plastic deformation amongst all microstructural constituents, which is mostly ascribed to its extensive dislocation density (**Figure 3.5**) inherited from two shear-dominant MTs;

(3) compared with the FCC→HCP MT, the sequential MT enables a more effective enhancement of local strain hardenability through the continuous formation of these highly-dislocated FCC-phases.

We note that albeit these evidence all support the potential enhancement of strain hardenability, systematic measurement of phase stress together with load-transfer evolution.

Section 3.2.2: Analyses and Discussion

Atomistic mechanisms for FCC→HCP MT has been well-documented in the literature, following the classical Olson-Cohen partial dislocation emission model [28] in which the nucleation of HCP-martensite is accomplished through the mono-directional gliding of $\frac{a}{6}\langle 112 \rangle_{\mathrm{FCC}}$-type of Shockley partials on every other $\{111\}_{\mathrm{FCC}}$ slip plane (**Figure 3.8 (a1)-(a4)**). This sort of mono-partial emission process results in triplex Burgers orientation relationships between HCP and FCC-phases: $\{111\}_{\mathrm{FCC}}//\{0001\}_{\mathrm{HCP}}$, $\langle 110 \rangle_{\mathrm{FCC}}//\langle 11\bar{2}0 \rangle_{\mathrm{HCP}}$, and $\langle 112 \rangle_{\mathrm{FCC}}//\langle 10\bar{1}0 \rangle_{\mathrm{HCP}}$ (**Figure 3.8 (a1)**). It could be hypothesized that by retracting the leading partials for them to re-associate with the trailing partials (or *vice versa*), the HCP→FCC MT can potentially be realized while simultaneously recovering the parent FCC-phase orientation (leading partials moving to trailing partials) or generating a $\Sigma 3$ boundary between them (trailing partials moving to leading partials). However, we argue that the sequential MT observed in the present study is unlikely to be accomplished through this mono-partial emission

scenario for the following reasons:

(1) the IPF shown in **Figure 3.2** and **Figure 3.3** reveals the distinctions in crystallographic orientation relationships between parent and newly formed FCC-phases, with no twin relation between them detected (**Figure 3.3 (f)** and **Figure 3.8 (b2)**);

(2) the meso-scale strain evolution chart (**Figure 3.6**) demonstrates the HCP→FCC MT neither counteracts nor shows the identical transformation strain of its previous HCP→FCC MT;

(3) the sequential MT procedure takes place completely in the quasi-static plastic deformation realm where any re-occurrence of the parent phase at bulk scale will violate the laws of energy dissipation.

Figure 3.8: Atomistic processes for the sequential FCC-HCP-FCC transformation. (a1)-(a5) the FCC-HCP transformation; (b1)-(b3) the HCP-(new)FCC transformation.

These observations, on the other hand, do imply it is the random partial emission (RPE) process [74,75] that assists the HCP→FCC MT. Such a mechanism involves synchronous activation of all possible partial dislocations, enabling stress delocalization while producing subtle macroscopic shape deformation in the parent phase, which is also rigidly in line with the much smaller $\varepsilon_{equivalent}$ increment with the HCP→FCC MT (**Figure 3.6 (e)**). As schematically illustrated in **Figure 3.8 (b3)**, by successively activating a_1, a_2, and a_3 type of partials on every other $\{0001\}_{HCP}$ plane, an FCC-structure can be consequently achieved, hence realizing the sequential FCC→HCP→FCC MT.

Next, we consider the energetics of the proposed RPE mechanism (**Figure 3.9**). By applying a Legendre transformation [76], we consider the total Gibbs free-energy functional G as the addition of internal Helmholtz free-energy $F^{int.}$ (quadratic approximation) and external work term (linear approximation) [44]:

$$G = F^{int.} - V(\sigma^{ext.} : \varepsilon) \tag{3.1}$$

where V, $\sigma^{ext.}$, and ε denote volume, applied stress field, and the corresponding strain field. Note that although both G and $F^{int.}$ are complex functionals involving various material parameters and boundary conditions, in the present thermodynamic formalism, only a fixed temperature T_0 (quasi-static straining) and changing deformation level ε are considered.
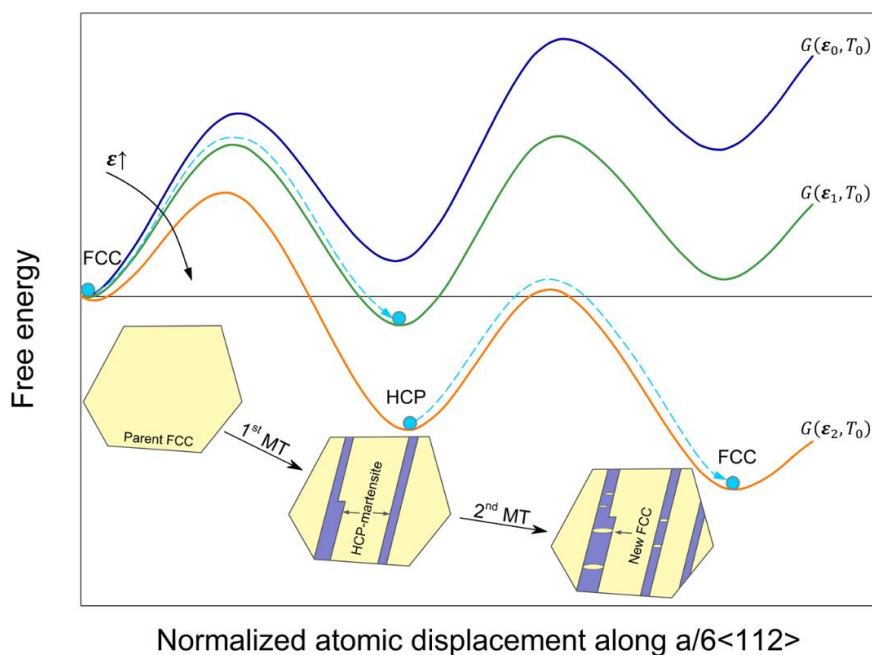
Figure 3.9: Considerations of the energy landscape evolution for the sequential martensitic transformation mechanisms.

Because neither plastic strain nor plastic stress is a state function, here we exploit the normalized atomic displacement along $\langle 112 \rangle$ direction as the reaction coordinate (horizontal axis). The blue curve marked as $G(\varepsilon_0, T_0)$ represents the energy landscape of the system at undeformed state (ε_0), where parent FCC-phase exhibits the minimum free-energy. At a deformation level of ε_1, a linearly approximated work term (although not depicted in the figure) modulates the energy landscape, enabling

the energetically favorable formation of HCP-phase, and also resulting in energy dissipation. As discussed earlier, if it is the partial re-association mechanism under mono-partial emission scenario that assists the new FCC-phase formation, the blue circle denoting the state of the system must navigate back to its original position, which under one consistent plastic loading condition, violates the law of energy dissipation. Rather, at an even higher deformation level ε_2 (where random partial emission is activated), the energy landscape can be significantly biased due to the imposition of an extensive amount of work, facilitating the formation of new FCC-phase in the system, which is consistent with the law of energy dissipation. Note that in the situation of random partial emission, each individual shear event still leads to an $|a/6\langle112\rangle|$ amount of atomistic displacement.

The last point to address is whether or not this sequential MT demonstrates any latent capability to promote strain hardenability. To ensure better statistical assessment, the evolution of representative $(111)_{FCC}$ and $(222)_{FCC}$ lattice strains in the loading direction together with the corresponding stacking fault probability is presented in **Figure 3.10**. As microscopic plastic incipience takes place ($\sim$120 MPa), both $(111)_{FCC}$ and $(222)_{FCC}$ planes reveal a significant relaxation in their lattice strains with monotonic incrementation in stacking fault probability, being well-recognized to result from the nucleation of strain-induced HCP-martensite [77,78]. More surprisingly, the determined lattice strains undergo another relaxation at an applied stress level of $\sim$300 MPa, upon which the stacking fault probability also reduces down to 0.0092, validating the annihilation of stacking faults during deformation.

The atomistic mechanisms (**Figure 3.8**), the *in-situ* EBSD analyses (**Figure 3.2**), and the phase constitution evolution (**Figure 3.4**) discussed above all suggest that this phenomenon be mostly ascribed to the appearance of HCP→FCC transformation. Such a peculiar lattice strain relaxation along the loading direction (corresponds to the plateau in **Figure 3.4 (a)**) indicates that the sequential MT enables stress alleviation, promoting deformation homogenization. On the other hand, aside from the creation of extensive FCC/HCP boundaries that dynamically refine the prior HCP bands, a higher magnification EBSD micrograph confirms the presence of a unique Σ3 boundary within the FCC-phase forms through the sequential MT (**Figure 3.5 (b)** and **(c)**). The formation of this sort of coherent boundary signifies the potential of strain hardenability promotion due to expedited dislocation multiplication and

enhanced dislocation-boundary interaction [79]. It should be pointed out that whether this $\Sigma 3$ boundary forms following the classical mechanical twinning mechanisms or *via* merging small lamellae of FCC that martensitically transform from different HCP basal planes, still requires further investigation.
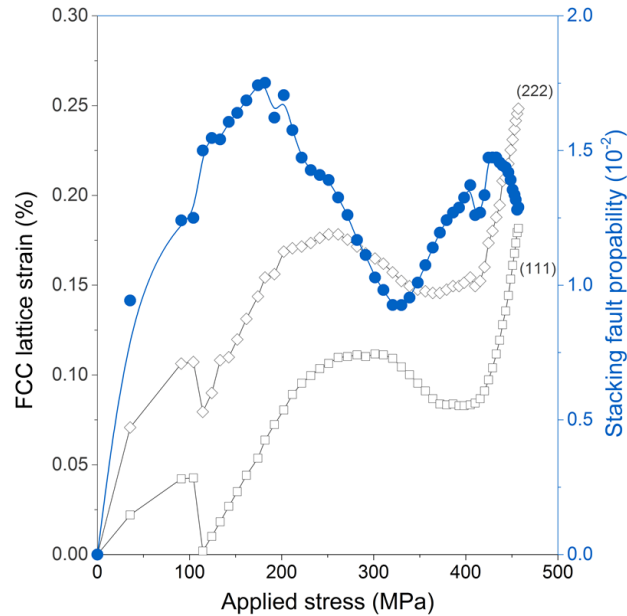
Figure 3.10: Lattice strain evolution during plastic deformation of the Fe$_{45}$Mn$_{35}$Co$_{10}$Cr$_{10}$ alloy

Section 3.2.3: Universality Considerations: Feasibility for Alloy Design

Sections 3.2.1 and 3.2.2 detail the observation of the FCC-HCP-FCC sequential transformation activated by monotonic plastic loading, and confirm the micro-mechanical benefits that it could potentially provide. However, a further proposition that would still require to be assessed is that whether or not such a mechanism can be generalized to other alloy systems. In order to explore this, we further design and assess the compositional dependency for this kind of phase transformation mechanism in a ternary FeMnCo system. Here, the primary focus is placed on the effect of Co content.

Ternary alloys with (Fe$_{60}$Mn$_{40}$)$_{100-x}$Co$_x$ (at. %) compositions were fabricated by vacuum arc melting, followed by cold-rolling, homogenization, and recrystallization treatment. For simplicity, we denote each ternary by its Co content (i.e. Co$_X$-alloy). One common issue during medium- and high-Mn containing ferrous alloys production is inevitable Mn loss due to evaporation during melting and oxidation during thermomechanical processing [80,81]. To assess the actual compositions of the

recrystallized alloys, energy dispersive X-ray spectroscopy (EDS) analyses (acquisition parameters chosen as 512×512 pixel^2 over 40×40 μm^2 area with a 64-frame binning setting) were conducted on the recrystallized alloys. **Tab. 3.1** comparatively reveals the conceived compositions and the ones determined by EDS, in which only subtle deviations are present. These results cross-validate the reliability of the compositional-dependency for mechanical metastability discussed next.

Table 3.1: Conceived and actual compositions for the four $(Fe_{60}Mn_{40})_{100-x}Co_x$ alloys (Unit: at. %)

Alloy category	Fe (conceived/actual)	Mn (conceived/actual)	Co (conceived/actual)
$(Fe_{60}Mn_{40})_{98}Co_2$	58.80/59.50 ±0.94	39.20/38.59 ±0.66	2.00/1.91 ±0.05
$(Fe_{60}Mn_{40})_{95}Co_5$	57.00/57.73 ±0.89	38.00/36.94 ±0.62	5.00/5.33 ±0.16
$(Fe_{60}Mn_{40})_{90}Co_{10}$	54.00/54.71 ±0.85	36.00/34.81 ±0.60	10.00/10.48 ±0.27
$(Fe_{60}Mn_{40})_{85}Co_{15}$	51.00/50.88 ±0.88	34.00/33.62 ±0.53	15.00/15.50 ±0.37

Microstructural investigation through backscatter diffraction (EBSD) and synchrotron X-ray diffraction (SXRD) confirm single FCC-phase microstructures in all four alloys together with random textures (**Figure 3.11 (a)-(d)**). These results suggest that Co content increase from 2 to 15 at. % exhibits a negligible influence on the formation tendency of HCP-martensite via thermal quenching. Although all four alloys were processed under the same conditions, a discernable grain size reduction can be seen within Co_{10} and Co_{15} alloys (**Figure 3.11 (c) and (d)**). While this phenomenon is not the main scope of the current research, it can be plausibly explained by the more sluggish recrystallization kinetics resulting from HCP-martensite formation during cold-rolling [44,82].

Figure 3.12 (a) reveals the SXRD patterns of the Co_{15}-alloy with respect to local plastic strain level. An evident mechanical metastability effect is also present, as featured by the discernable HCP peaks as local plastic strain increases. Similar characteristics are also observed in the Co_{10}-alloy (not shown here). SXRD results also confirm the absence of transitional structure in these two alloys. The Co_2 and the Co_5 alloys, on the other hand, both preserve single FCC phase constituents at all surveyed deformation levels, implicating their mechanical stability in response to plastic strain.
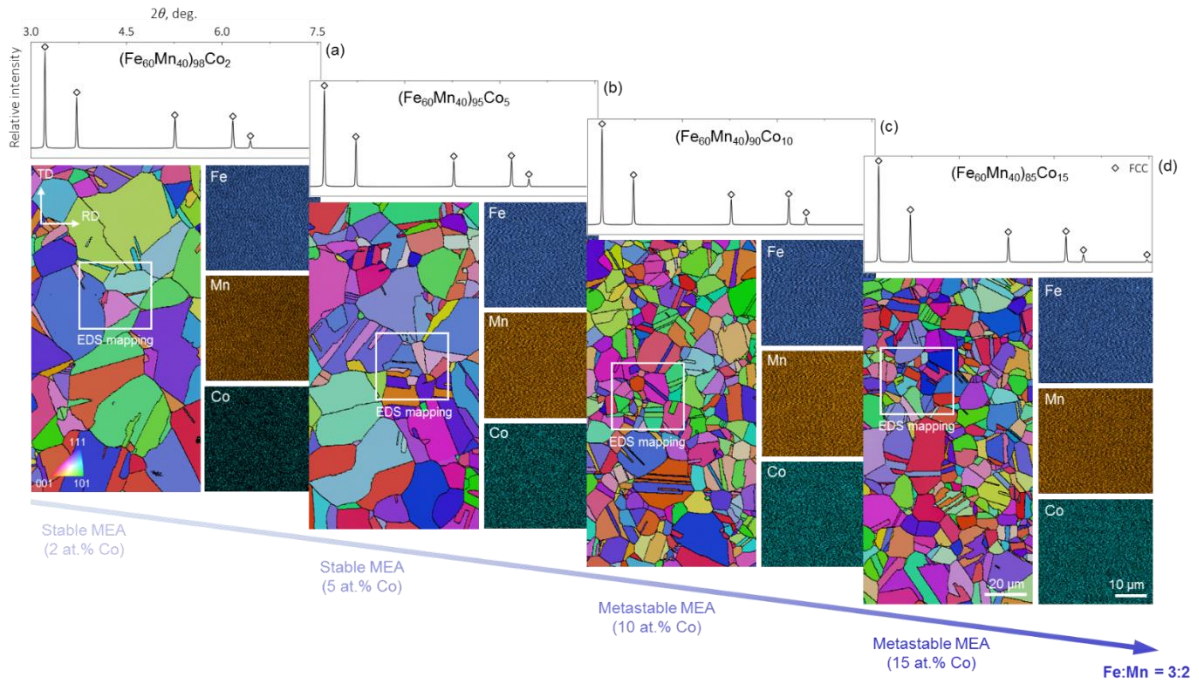
Figure 3.11: Fully recrystallized microstructures and phase constitutions of the ternary $(Fe_{60}Mn_{40})_{100-x}Co_x$ alloys. (a)-(d) alloys with the same Fe-to-Mn ratio but increasing Co content.
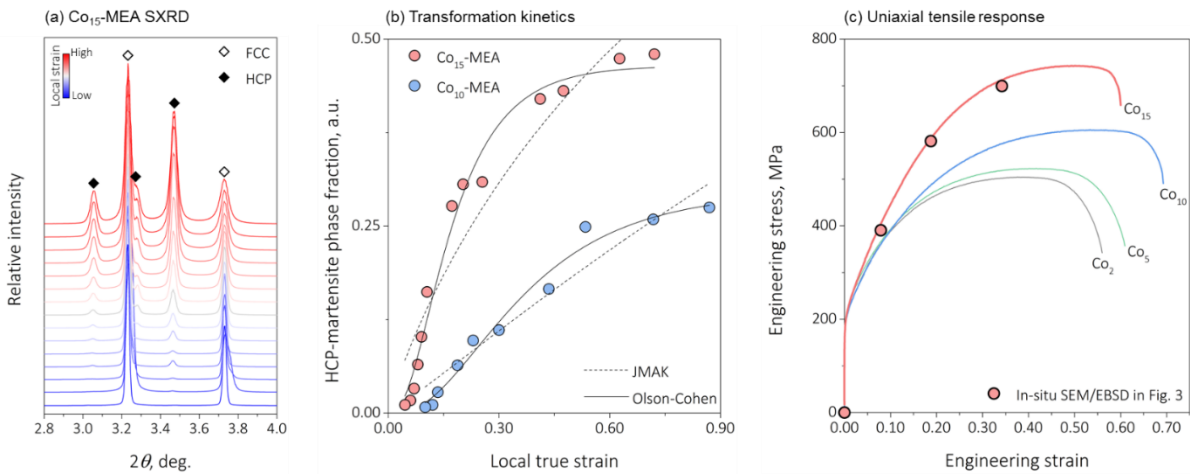
Figure 3.12: Explorations of mechanical metastability in the $(Fe_{60}Mn_{40})_{100-x}Co_x$ alloys. (a) Exemplary SXRD patterns of the Co_{15}-alloy; (b) phase transformation kinetics; (c) uniaxial tensile response.

The HCP-martensite phase fraction was determined from the SXRD diffractograms for the Co_{10} and the Co_{15} alloys using Rietveld refinement [83]. As seen in **Figure 3.12 (b)**, highly accelerated transformation kinetics exist in the Co_{15}-alloy: at similar local plastic train levels, the HCP-martensite fraction is roughly two times higher than the Co_{10}-alloy. It is therefore recognized that although the thermal stability of the FCC phase remains unaffected by the Co content (**Figure 3.11**), the mechanical stability, is correlated with the increasing Co content. The HCP-martensite fractions (f) in the Co_{10} and

the Co_{15} alloys are further assessed by two well-documented kinetic models. First, the classical Johnson-Mehl-Avrami-Kolmogorov (JMAK) model [84], in which the growth rate and the progression of transformation are independent and nucleation is homogenous (**Eq. (3.2)**). Second, the Olson-Cohen model [85], although primarily applied in α'-martensite formation, parameterizes the inhomogeneous nucleation contributed by plastic straining (**Eq. (3.3)**). In both equations, ε represents the plastic strain value. α in **Eq. (3.3)** is related with HCP-martensite band formation rate, while β describes the potency of HCP-martensite band intersection. The exponent n in **Eq. (3.3)** implies the density of HCP-band intersection and a higher n value suggests a burst-like development of HCP-band intersection.

$$f = 1 - \exp(-K\varepsilon^n) \tag{3.2}$$

$$f = 1 - \exp\left[-\beta\left(1 - \exp(-\alpha\varepsilon)\right)^n\right] \tag{3.3}$$

As seen from the dotted lines in **Figure 3.12 (b)**, both alloys exhibit discernable deviations from the JMAK predictions, implicating two possible kinetic mechanisms:

(1) HCP-martensite nucleation in these two alloys may not be ideally homogenous because plastic straining can be highly inhomogeneous at the microstructural level [86,87].

(2) a strong interdependency could exist between the transformation rate and the progression of the transformation, which is plausibly due to deformation hardening of the untransformed FCC phase [44].

In contrast, better correlations are seen in the Olson-Cohen model, as depicted by the solid lines in **Figure 3.12 (b)**. A much higher α value of 8.28 achieves in the Co_{15}-alloy than the Co_{10}-alloy ($\alpha = 4.25$), validating the higher HCP-martensite formation rate as Co content increases. The β factor, although moderate in both alloys, is slightly higher in the Co_{15}-alloy (0.62 versus 0.35) which indicates higher HCP-band intersection probability. Finally, a smaller n value presents in the Co_{15}-alloy (2.83 versus 3.03), implying the seemingly less burst-like development in HCP-band intersections. These quantitative assessments underpin the positive contribution of Co addition in expediting plastic strain-induced FCC-HCP transformation kinetics. Because of this, uniaxial tensile properties of the Co_{15}-alloy

stand out amongst all four alloys (**Figure 3.12 (c)**). It yields at ~195.3 MPa, then undergoes a salient strain hardening process, reaching an ultimate tensile strength of ~742.8 MPa with ~0.60 fracture elongation. Note that these properties were achieved in an un-optimized condition, aiming to study the compositional dependency of mechanical metastability. One interesting aspect of the Co_{15}-alloy is that provided the highly accelerated FCC-HCP transformation kinetics, the resultant ductility is not significantly impaired as some HCP-phase-rich metastable HEAs revealed [88]. This triggers a further assessment of the underlying phase transformation pathways and deformation micro-mechanisms.

Figure 3.13 details the *in-situ* scanning electron microscopy (SEM)/EBSD investigation of the strain-induced FCC-HCP martensitic transformation and subsequent deformation processes within the HCP-martensite. At the undeformed state, the selected area of interest solely consists of FCC-phase (**Figure 3.13 (a1)** and **(b1)**). To track the deformation micro-events in the HCP-martensite, magnified backscatter electron (BSE) micrographs of a local region (see the white box) are provided in **Figure 3.13 (c1)-(c4)**. Note that the spherical particles seen in the *in-situ* BSE micrographs are colloidal SiO_2 used for strain computation intended for analyses not discussed here. At a global stress of 390.4 MPa, plastic deformation takes place, which is indicated by noticeable surface steps (**Figure 3.13 (b2)** and **(c2)**). EBSD phase map acquired at the same region confirms the formation of HCP-martensite in both grains (**Figure 3.13 (a2)**), and only one HCP-martensite variant nucleates per grain. The thinner traces close to the bottom of **Figure 3.13 (b2)** are slip traces of perfect dislocations in the parent FCC-phase. As plastic straining increases, the nucleated HCP-martensite plates undergo growth and an increasing number of slip traces also start to appear. It is suggested by crystallographic calculation that the HCP-martensite variant belong to $(111)_{FCC}$ plane in the lower grain and $(11\bar{1})_{FCC}$ plane in the upper grain (also see **Figure 3.13 (d2)**). The perfect dislocation slip traces all belong to $(\bar{1}11)_{FCC}$ plane. The magnified BSE micrograph in **Figure 3.13 (c3)** also verifies the absence of other HCP-martensite variants (**Figure 3.14**).

When the global stress increases to 699.4 MPa, an extensive amount of plastic deformation has taken place. This can be qualitatively inferred from the grain's shape distortion (**Figure 3.13 (b4)**). In both grains, given the massive HCP-martensite, no evident cracking occurs in the grain interior, which implies the deformability of the HCP-martensite in the Co_{15}-alloy. An interesting spindle-like feature

forms in the upper grain interior (**Figure 3.13 (c4)**) exhibiting a convex surface topology. High magnification EBSD analysis verifies that such a feature reveals an FCC structure (**Figure 3.13 (d1)**).
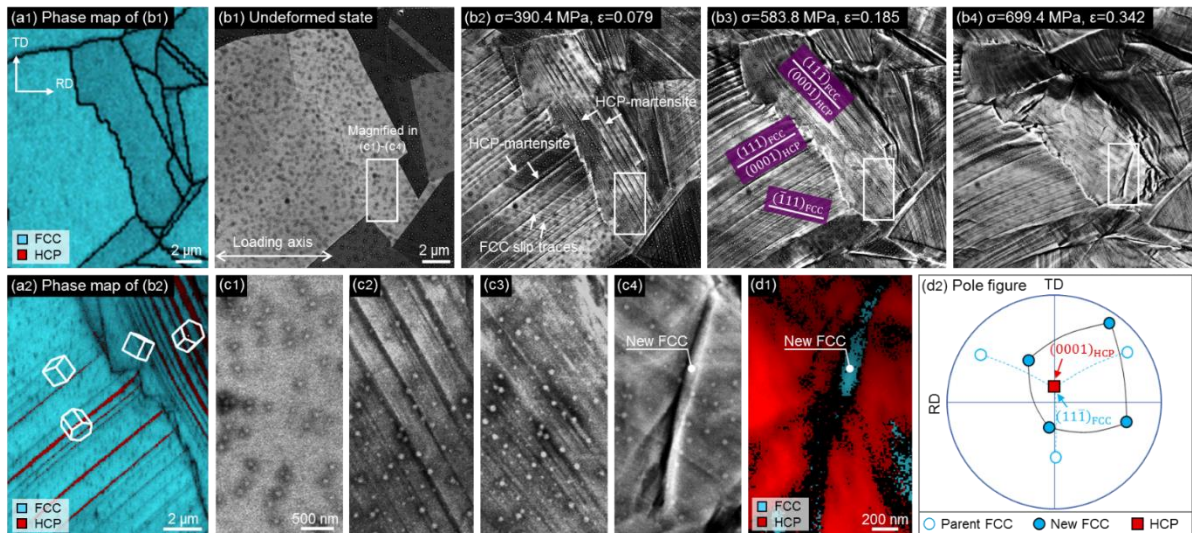
Figure 3.13: *In-situ* SEM/EBSD studies of martensitic transformation during plastic straining in the Co$_{15}$-alloy. (a1) and (a2) EBSD phase maps; (b1)-(b4) lower magnification BSE micrographs; (c1)-(c4) magnified BSE micrographs highlighting the FCC-HCP-(new)FCC transformation; (d1) EBSD phase map; (d2) pole figure
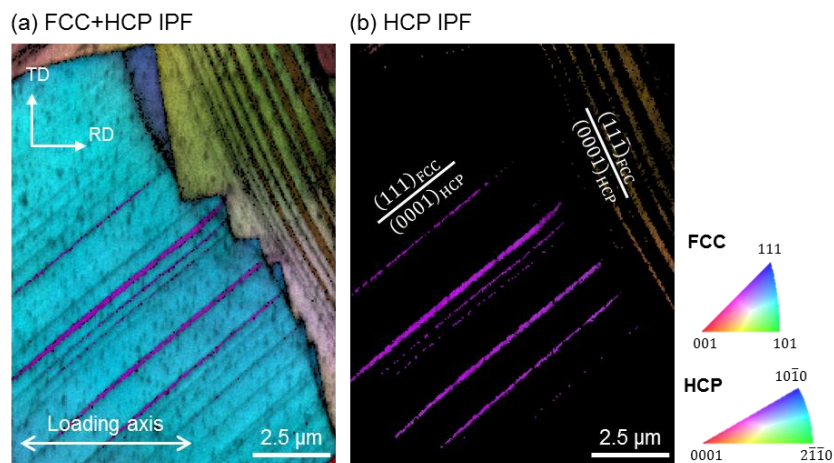
Figure 3.14: Complementary EBSD inverse pole figures. (a) Coupled IPF with both FCC and HCP phases; (b) independent HCP IPF.

However, according to pole figure (**Figure 3.13 (d2)**) its crystallographic orientation is different from the parent FCC-phase. Also similar to the results in the Fe$_{45}$Mn$_{35}$Co$_{10}$Cr$_{10}$ alloy explored in Section 3.2.1, no twin relationship is found between the new FCC and parent FCC phases. These *in-situ* analyses highlight that the strain-induced HCP-martensite within the Co$_{15}$-alloy is highly deformable, and can

even further transform, realizing the FCC-HCP-FCC transformation pathway, as revealed in the previous section (especially **Figure 3.8**). Note again, that this phenomenon should not be confused with pseudoelasticity or shape-memory effect. In the latter case, martensitic transformation is assisted by elastic stress and the reverse transformation, which recovers the parent phase orientation, is indispensable of load removal and/or temperature increase [62,89]. In contrast, the FCC-HCP-FCC martensitic transformation pathway reported here is achieved purely in the plastic region under a quasi-static monotonic loading condition.

To further assessed the atomistic details of the transformation, STEM analyses were carried out for HCP-martensite. The STEM samples were prepared by the FIB lift-out process in a region that demonstrates fully HCP-structure, as detailed in **Figure 3.15**. The FIB-sectioning direction was chosen based on surface trace analysis in order to get close to the targeted $[11\bar{2}0]_{\text{HCP}}$ zone axis for STEM imaging.
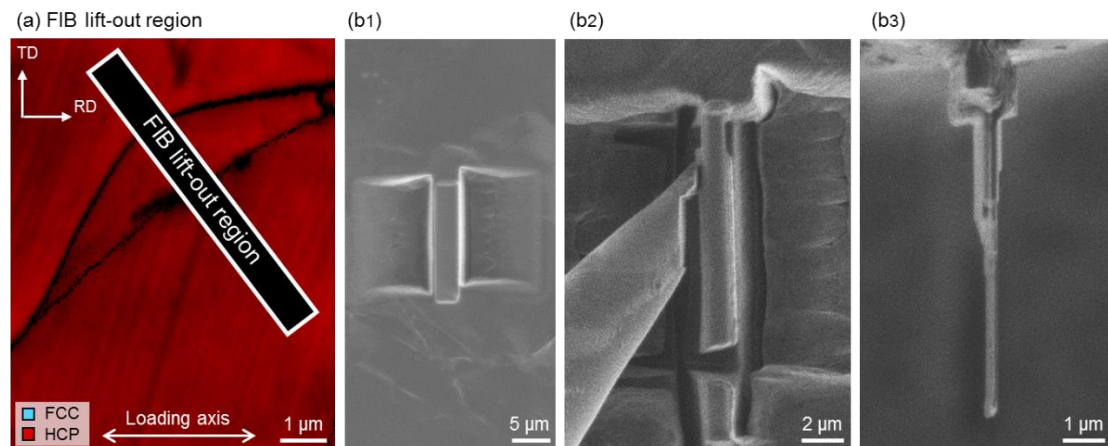
Figure 3.15: Details for the FIB-STEM sample preparation. (a) EBSD phase map of the selected region for lift-out; (b1)-(b2) FIB machining and lift-out processes

High-angle annular dark-field (HAADF)-STEM micrographs acquired along the $[11\bar{2}0]_{\text{HCP}}$ zone axis (**Figure 3.16 (a1)**) reveal the prototypical $...ABABABAB...$ stacking sequence of the HCP-martensite in a majority of the sample area (**Figure 3.16 (a3)**). A closer inspection of the atomistic structures in **Figure 3.16 (a3)** highlights the presence of basal stacking fault within the vast HCP region, suggesting the local atomic stacking sequence changes into $...ABABA|\boldsymbol{C}|BAB...$ (also see the colored atoms). Geometric phase analysis (GPA) [48] also cross-confirms the localized shear strain (ε_{xy} component)

elevation along the basal faulting plane (**Figure 3.16 (b2)**). This is ascribed to the $a/3 < 10\bar{1}0 >$-type of partial dislocation (see **Figure 3.8 (a5) and (b1)** as a reference) emission that enables the faulted $|C|$-layer. This observation is consistent with the partial emission mechanisms proposed in Section 3.2.2, which highlights the importance of partial dislocation emission with the strain-induced HCP-martensite.
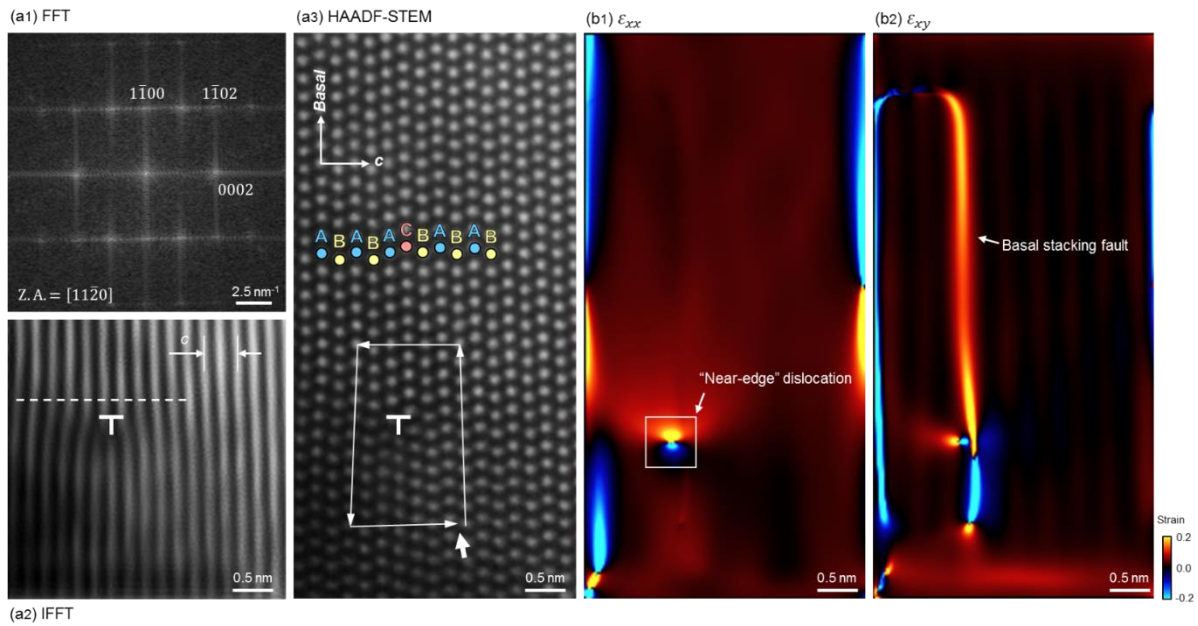
Figure 3.16: STEM characterization of the HCP-martensite in the Co$_{15}$-alloy. (a1) fast-Fourier transform micrograph; (a2) inverse fast-Fourier transform of (a1); (a3) HAADF-STEM micrograph; (b1) and (b2) atomic-level strain accommodations.

Before concluding the study in this section, one additional insight from the STEM characterization is also worth mentioning, that is the presence of dislocation within the HCP-martensite (**Figure 3.16 (a3)**). Based on definition, the Burgers circuit in **Figure 3.16 (a3)** shows that the "near-edge" dislocation core has both ⟨**c**⟩ and ⟨**a**⟩ components. Although cross-validation may be necessary via **g · b** analysis to check the residual contrast under the $[0002]_{HCP}$ reflection, the present observation is informative to better understand the favorable deformability of the HCP-martensite. Like all other HCP-metals, a stable plastic flow in HCP-martensite requires at least five independent slip systems [90]. In terms of perfect dislocations, basal-⟨**a**⟩ and prismatic-⟨**a**⟩ slip can maximally enable four independent slip systems. As such, additional plasticity mechanisms shall be involved to accommodate plastic strain along the non-basal directions [90,91], which was proved critical for promising deformability in numerous HCP-metals [87,92,93]. The mixed ⟨**c**⟩ and ⟨**a**⟩ property of the dislocation observed here

suggests deformation micro-events that enable effective plastic strain accommodation along the $[0001]_{HCP}$ axis, which in turn contributes to the deformability of the HCP-martensite (**Figure 3.13 (b3) and (b4)**). However, considering the debate over the actual slip pathways of non-basal dislocations [92–94], future *in-situ* TEM studies are needed to unambiguously resolve dislocation plasticity events in HCP-martensite. More detailed discussion on this direction is provided in Chapter 5.

Section 3.3: Thermally-driven HCP-FCC Reverse Transformations

The previous Sections present detailed microstructural design strategies using external plastic loading, aiming to trigger a further displacive phase transformation in the strain-induced HCP-martensite. Following this concept, another proposition can be asked: would it be possible to also employ external heat, activating an HCP-martensite to FCC reverse transformation? In addition to the general objectives stated in the introduction section, the study presented in this section is also motivated by the following two additional factors:

(1) HCP-martensite has been recognized to possess relatively low thermal stability. Lee et al [95], for example, reviewed that the austenite start temperature (A_s point) decreased monotonically from ~200 to ~150 °C as a function of increasing Mn content from 15 to 30 wt.%. Such a low transformation temperature range raises the possibility of feasible thermal processing opportunities similar to bake hardening (BH) treatment, which has not yet been explored;

(2) classical BH treatment in interstitial strengthened Fe- or Al-based alloys involves thermally-assisted segregation of interstitials to dislocation sites, creating a strengthening effect due to the enhanced solute pinning. [96,97]. However, it often inevitably results in cumulative ductility compensation because of the deficiency in dislocation multiplication, leading to the deterioration in strain hardening capability.

Section 3.3.1: Results

The metastable alloy utilized in this section is the $Fe_{45}Mn_{35}Co_{10}Cr_{10}$ alloy introduced in Section 3.2.1. To avoid redundancy, general characterization of its microstructure will not be presented again. With the occurrence of strain-induced martensitic transformation upon plastic incipience, the metastable $Fe_{45}Mn_{35}Co_{10}Cr_{10}$ alloy shows a desirable strain hardenability, enabling an ultimate tensile strength (UTS) of 568 MPa and a fracture elongation of 0.51 (the dark blue curve in **Figure 3.17 (a)**). Note that the absence of Portevin–Le Chatelier band [98] in **Figure 3.17 (a)** eliminates the contribution of interstitial atoms. The red curve in **Figure 3.17 (a)** reveals a comparative specimen which was pre-deformed to a global strain level of 0.14, unloaded and annealed at 200 °C for 20 min under high-purity argon protection then re-deformed. It is seen that this treated alloy possesses both enhanced strength

and cumulative ductility than its as-homogenized counterpart: UTS approaches 627 MPa (10.0 %
relative increase) with 0.58 cumulative fracture elongation (15.1 % relative increase). Moreover, the
treated alloy exhibits a more moderate drop in strain hardening rate as a function of increasing true
strain level, which indicates an enhanced resistance to plastic instability (highlighted by arrows in the
inset of **Figure 3.17 (b)**).
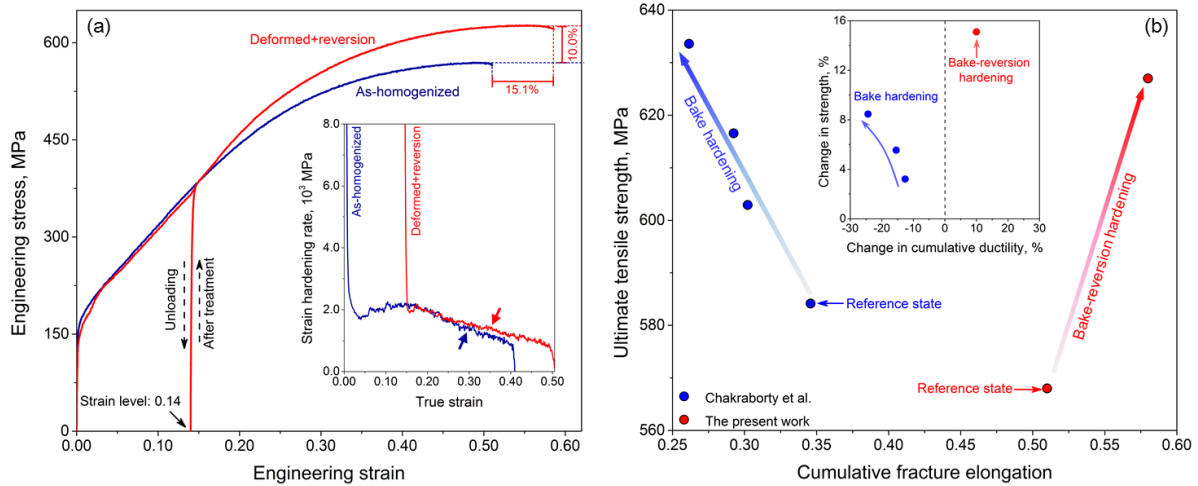
Figure 3.17: Bake-reversion hardening in the metastable Fe$_{45}$Mn$_{35}$Co$_{10}$Cr$_{10}$ alloy. (a) Engineering
stress-strain curves of as-homogenized and bake-reversion treated alloy with strain hardening rate plot
inserted; (b) comparison of strength-cumulative ductility synergy between a conventional bake-
hardenable Fe-based alloy [96] and the present alloy undergoes bake-reversion hardening.

Considering the low annealing temperature and similar to the bake hardening treatment, **Figure 3.17**
(b) presents a comparison of the variation in tensile properties with a bake hardenable Fe-based alloy
[96] (pre-strained and annealed at 170 °C for 20 min) that shows a similar UTS value to the present
alloy at its reference state. It is recognized that the interstitial-assisted BH mechanism within the Fe-
based alloy enables increasing UTS at various pre-strained levels, whereas the cumulative fracture
elongation witnesses a monotonic decreasing trend down to 24 % (inset of **Figure 3.17 (b)**). In contrast,
concurrent enhancement in UTS and cumulative fracture elongation is achieved in the metastable alloy
tested here. Next, we explore the origins of such a latent strengthening mechanism, specifically focusing
on the thermally-induced HCP-martensite to austenite reverse transformation.

We first focus on the evolution of phase constitution before and after reversion annealing. As shown in
Figure 3.18 (a1)-(d1), the parent FCC-phase is mechanically metastable. With increasing local strain

level, its fraction decreases from 83 % to 36 % as the local strain level evolves from 0.15 to 0.55 (quantitatively presented in **Figure 3.19 (a)**). This athermic FCC-HCP transformation upon deformation not only creates extensive HCP/FCC phase boundaries that suppress dislocation motion but also results in stress delocalization, which as a whole enables the desirable strength-ductility synergy (**Figure 3.17 (b)**). It is recognized from **Figure 3.18 (a2)-(d2)** and **Figure 3.20 (a)** that the 200 °C 20 min annealing treatment can actually revert strain-induced HCP-martensite back to FCC-austenite. Such a reverse austenitic transformation also demonstrates a sensitivity to local pre-strain level: complete reversion (FCC fraction over 99 %) only takes place at a relatively low strain level of 0.15, while a monotonic decreasing trend of FCC fraction is observed with increasing local strain level (**Figure 3.20 (a)**).
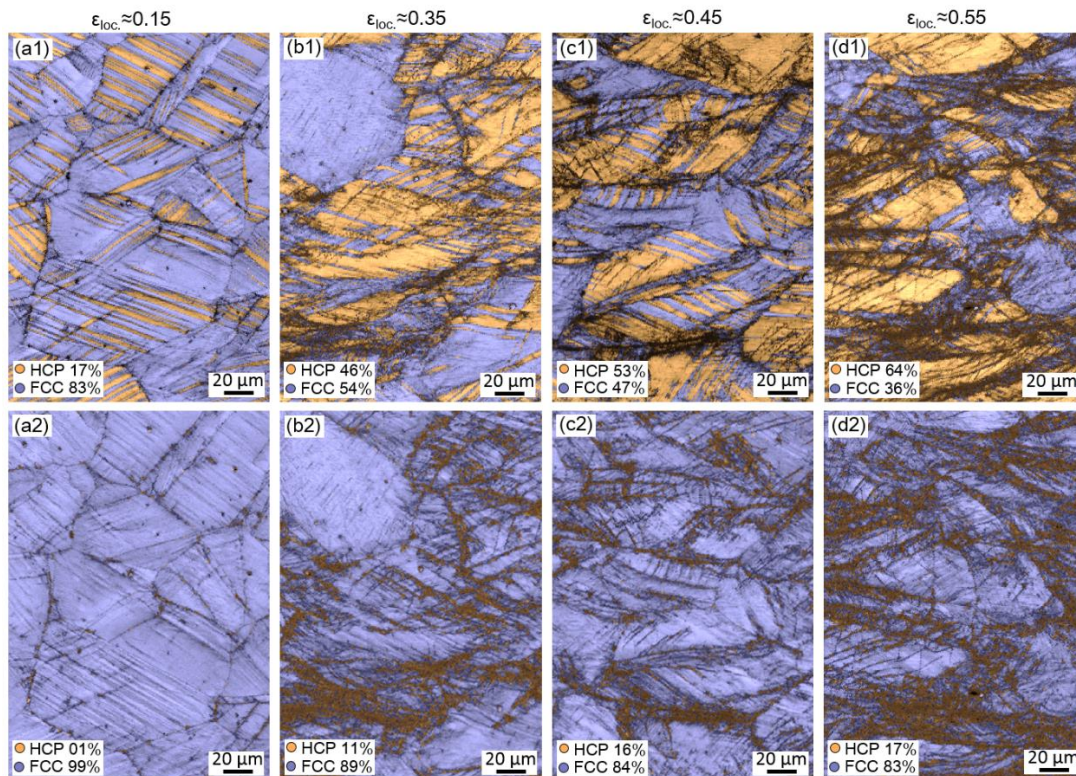
Figure 3.18: EBSD maps of phase constituent evolution with respect to increasing local strain level (with IQ value overlapped). (a1)-(d2) Deformed state; (a2)-(d2) same regimes after 200 °C, 20 min reversion annealing.

This sort of dependency can be understood from the following two aspects:

First, dislocation plasticity within the strain-induced HCP-martensite. Unlike the HCP-martensite reported in conventional Co-rich alloys that exhibits a brittle characteristic [99,100], the strain-induced HCP-martensite in the present $Fe_{45}Mn_{35}Co_{10}Cr_{10}$ alloy reveals a c/a ratio of 1.6238 [37] which

indicates a desirable propensity to undergo further plastic deformation after its nucleation. A separate *in-situ* SEM-based tensile experiment (**Figure 3.19**) further demonstrates the presence of slip steps within the strain-induced HCP-martensite, confirming the activation of extensive dislocation plasticity. With elevating local strain level, increasing amount of dislocations will be generated within the HCP-martensite, resulting in the hindered reverse transformation as shown in **Figure 3.20 (a)**;
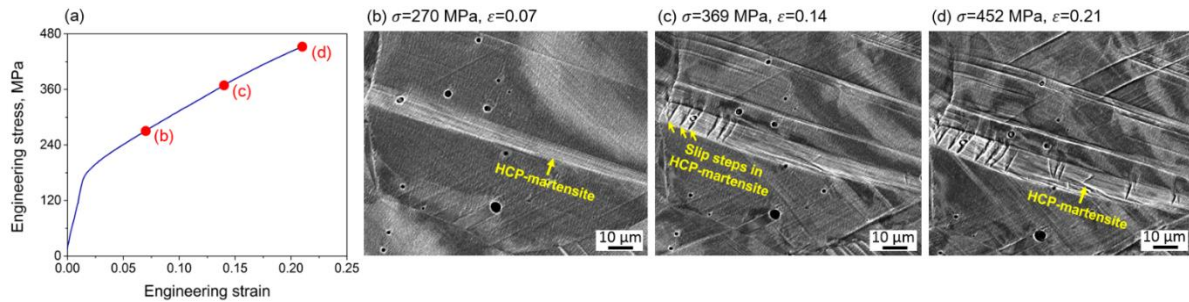
Figure 3.19: *In-situ* **SEM experiment proving the dislocation plasticity processes within the strain-induced HCP-martensite.** (a) Engineering stress-strain curve; (b)-(c) formation of the strain-induced HCP-martensite and validation of its dislocation plasticity
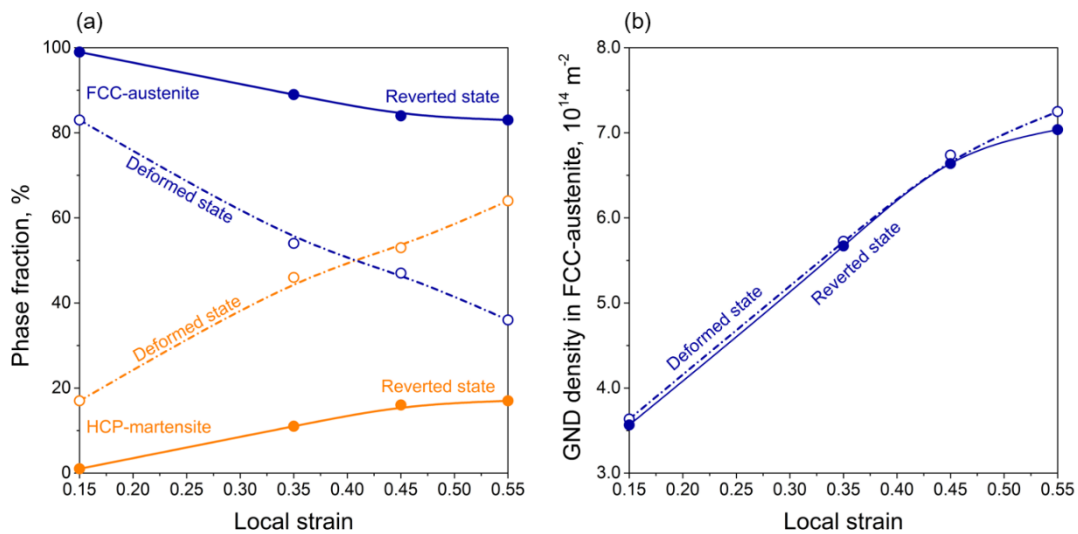
Figure 3.20: Quantitative assessment of the reverse transformation. (a) Phase constitution evolution before and after bake-reversion annealing (dark blue lines: FCC-austenite, orange lines: HCP-martensite); (b) average geometrically necessary dislocation (GND) density versus local strain level within the FCC-austenite (an FCC lattice constant of 3.61 Å measured from synchrotron X-ray diffraction [37] was adopted for the GND density computation).

Second, deformation hardening of untransformed FCC-austenite. On the other hand, plastic deformation of the FCC phase can either be activated by external loading or associated with the formation of HCP-

martensite. Through these two pathways, the untransformed FCC phase will undergo deformation hardening especially at extensive local strain levels (confirmed from low IQ values in **Figure 3.18 (c2) and (d2)**), giving rise to stronger mechanical suppression to the shear-assisted displacive reverse transformation (see discussion in the next section). The average geometrically necessary dislocation (GND) density within the FCC-austenite (**Figure 3.20 (b)**) preserves almost the same value before and after reversion annealing, indicating negligible recovery softening effect has taken place, which is also confirmed from the invariant yielding point in **Figure 3.17 (a)**.

Section 3.3.2: Analyses and Discussion

Results presented in the previous section underpin the activation of an HCP-to-FCC reverse transformation in the similar time scale and temperature range as the BH process, but leading to the improvement in both strength and ductility. This section will further explore the underlying mechanisms, starting with the reverse transformation kinetics.

It has been well-documented in the literature that martensite-to-austenite reverse transformation can exhibit either diffusional or displacive characteristics [82,101]. In the former case, A_s and A_f temperatures were reported to demonstrate elevating trend with respect to increasing heating rate, while in the latter situation, these two characteristic temperatures revealed nearly constant values regardless of heating rate [102]. **Figure 3.21 (a)** shows the DSC results of pre-deformed specimens tested at various heating conditions. All specimens clearly demonstrate endothermic peaks within the temperature range of 160-180 ^{o}C, confirming the comparatively low thermal stability of the strain-induced HCP-martensite. The measured A_s and A_f temperatures remain independent to increasing heating rate from 5 ^{o}C min^{-1} to 20 ^{o}C min^{-1} (**Figure 3.21 (b)**), exhibiting only slight decrease as the heating rate reaches 40 ^{o}C min^{-1}. The relatively low transformation temperature, the nearly constant A_s and A_f temperatures, and the composition fully consisting of substitutional alloying elements, all lead to the conclusion that the observed HCP-martensite-to-austenite transformation is accomplished by a shear-assisted displacive mechanism.

The kinematics of this reverse transformation can therefore be understood via the dislocation-based

Olson-Cohen model [28]: under external loading, HCP martensite forms due to the $\frac{a}{6} < 112 >$-type mono-directional glide of Shockley partials along every other $\{111\}_{FCC}$ plane. The thermal effect, on the other hand, compensates the activation energy for the backward shearing of these dissociated partials, completing the reverse transformation. Such a shear-assisted displacive mechanism also implies that extensively dislocated HCP-martensite and deformation hardened FCC-austenite will both exhibit more suppression effect on the reverse transformation, which is supportive to the decreasing FCC phase after reversion annealing as a function of increasing local strain level demonstrated in **Figure 3.20 (a)**.
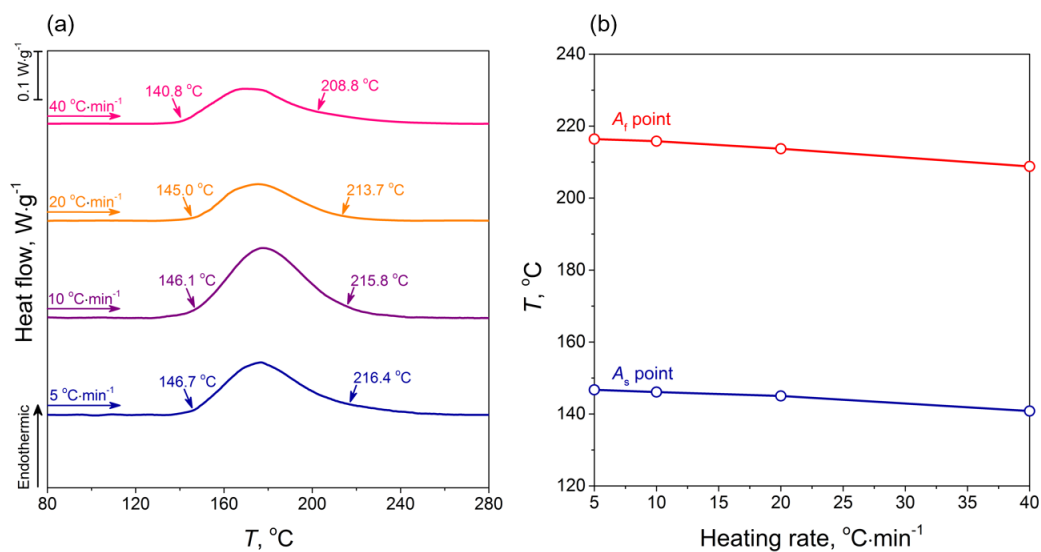
Figure 3.21: Kinetic features of the reverse transformation. (a) DSC curves at multiple heating rates; (b) measured A_s and A_f temperatures as a function of increasing heating rate.

We then consider the strengthening and ductilization mechanisms. As mentioned above, the dislocation-based kinematic theory implies the incipience of HCP-martensite formation is a competitive deformation module against perfect dislocation glide [21,28] (dislocation plasticity of parent FCC-austenite). In such a situation, HCP-martensite formation within grain interior usually obeys the mono-variant principle [21], namely nucleates on one of the $\{111\}_{FCC}$ family planes that exhibits the largest Schmid factor (SF) for the corresponded $\frac{a}{6} < 112 >$-type of partial dislocation shear. Whereas, inverse pole figure (IPF, **Figure 3.22 (a)**) taken in a deformed specimen after reversion annealing clearly evidences the formation of secondary HCP-variants (highlighted as A and B in **Figure 3.22 (a)** and **(b)**).
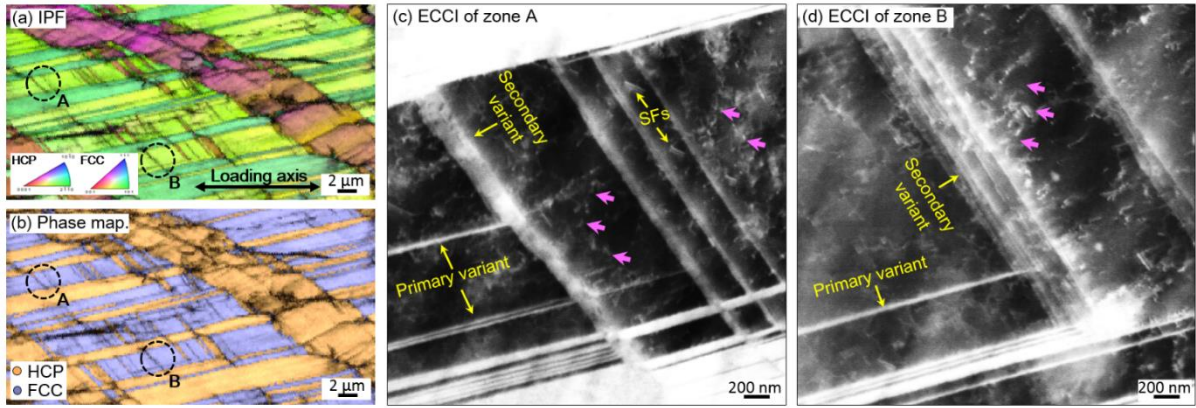
Figure 3.22: Microstructural characterization of the multi-variant configuration. (a) EBSD IPF map taken at a deformed specimen after reversion treatment (local strain level ~0.30, with IQ value overlapped); (b) phase map correspond to (a); (c) and (d) ECCI micrographs for defect characteristics of regimes A and B marked in (a) and (b) (SF: stacking fault).

We propose a kinematic-energetic model to clarify the formation mechanism of these secondary HCP-variants. The thermally-activated reverse motion of Shockley partials not only gives rise to the reversion transformation but also leads to the formation of emissary dislocations [90,103] jamming along the original FCC/HCP phase boundaries. As schematically depicted in **Figure 3.23 (a)**, the existence of one emissary dislocation will result in a localized shear displacement of ϑ of which the corresponding internal shear stress magnitude demonstrates an $\frac{1}{x}$ decay in between the dislocation core and the stress screening regimes [90]. Following the free-energy landscape concept proposed in Section 3.2.2 (especially, **Figure 3.9** and **Eq. (3.1)**), the internal Helmholtz free energy of the present alloy can be sketched as the grey line in **Figure 3.23 (b)**, where the two local minima represent the parent FCC phase and the secondary HCP-variant.

When external loading is applied to an as-homogenized alloy (**Figure 3.17 (a)**), the strain-induced primary HCP-variants tend to follow the Schmid criterion. However, the energy landscape along the secondary $\frac{a}{6} < 112 >$ direction will only be slightly altered, and almost no secondary HCP-variant can form in the grain interior due to the less-preferred energy state (dark blue line marked as "without dislocations" in **Figure 3.23 (b)**). While in the case of a pre-strained and reversion annealed alloy (**Figure 3.17 (a)**), as discussed in **Figure 3.23 (a)**, the internal stress field brought about by the large amount emissary dislocations can potentially exhibit a positive shear component in the secondary $\frac{a}{6} <$

112 > direction, which is in equivalent to providing an extra driving force to the work term in **Eq. (3.1)**. The net result of this gives rise to a more negative slope in the linearly approximated work term that significantly biases the energy landscape, leading to the energetically favorable nucleation of secondary HCP-variant that even violates the Schmid criterion (red line marked as "with dislocations" in **Figure 3.23 (b)**).
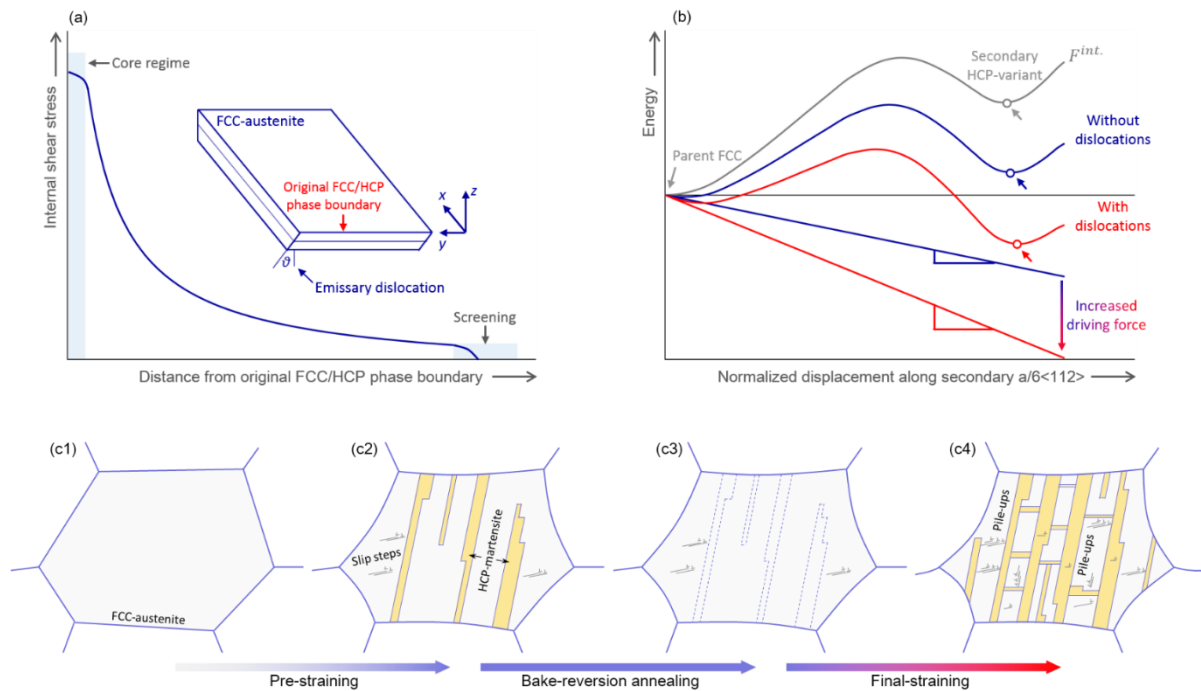
Figure 3.23: Kinematic-energetic considerations for secondary HCP-variant formation and the corresponding strengthening and ductilization mechanisms. (a) Internal stress field generated by an emissary dislocation at the original FCC/HCP phase boundary; (b) energy landscape of dislocation-assisted secondary HCP-variant formation (y-axis can also be considered as generalized stacking fault energy [104,105]); (c1)-(c4) phenomenological model elucidating the mechanisms of bake-reversion hardening.

This kind of multi-variant configuration can lead to both strength and cumulative ductility improvement through the following two-fold mechanisms:

(1) improved stress delocalization capability: As phenomenologically confirmed from the strain hardening rate (inset of **Figure 3.17 (a)**), the reversion annealed alloy exhibits a more moderate decrease in strain hardening rate as deformation proceeds. This implies that the nucleation and growth of the secondary variant facilitates the transformation rate, which adds on to the beneficial effect of reliving local stress concentration and thereby more efficiently promotes deformation

homogenization;

(2) enhanced phase boundary-dislocation interactions: **Figure 3.22 (c)** and **(d)** reveal the defect characteristics associated with the formation of primary and secondary variants (regimes A and B marked in **Figure 3.22 (c)** and **(d)**). Dislocation pile-ups can be observed near the HCP-martensite plates (highlighted by pink arrows), indicating the strong impingement of mobile dislocation with FCC/HCP phase boundaries. Moreover, the nucleated secondary variant also intersects with the primary variant, which drastically decreases the mean free path of perfect dislocation glide, contributing to the increased UTS achieved within the bake-reverted alloy (sometimes also known as, an expedited dynamic Hall-Petch effect).

The microstructure development resulting from pre-straining, bake-reversion annealing, and final straining can be summarized as **Figure 3.23 (c1)-(c4)**. In a mechanically metastable HEA, the strain-induced FCC-austenite to HCP-martensite transformation is stimulated upon pre-straining (**Figure 3.23 (c1)-(c2)** and **Figure 3.18 (a1)-(d1)**). Due to the relatively low thermal stability of the strain-induced HCP-martensite, a 200 ºC, 20 min baking treatment can activate a shear-assisted displacive HCP-to-FCC reverse transformation (**Figure 3.23 (c3)**, **Figure 3.18 (a2)-(d2)**, and **Figure 3.21 (b)**), leaving behind emissary dislocations (dashed-line in **Figure 3.23 (c3)**) along the original FCC/HCP phase boundaries. This sort of bake reversion annealing treatment facilitates the nucleation of secondary HCP-variant that intersects with primary HCP-variant upon further loading (**Figure 3.23 (c4)**), which contributes to the simultaneous enhancement in strength and cumulative ductility (**Figure 3.17 (b)** and **(c)**).

Section 3.4: Conclusions

In summary this Chapter revealed phase transformation-based strategies to further improved the mechanical performances of metastable FeMnCoCr-type alloys. Two transformation pathways, i.e. plastic strain-induced FCC-HCP-FCC sequential transformation, and thermally-driven HCP-FCC reverse transformation were systematically explored and the corresponding mechanisms were also discussed. Major findings of this chapter are summarized as follows:

(1) By studying the $Fe_{45}Mn_{35}Co_{10}Cr_{10}$ alloy using *in-situ* μ-DIC and *in-situ* synchrotron X-ray diffraction, a peculiar FCC-HCP-(new)FCC sequential martensitic transformation chain was identified. This interesting transformation takes place purely at the plastic region under a monotonic loading condition. Through μ-DIC analyses and crystallographic calculation, the random partial emission mechanisms are recognized to be the plausible atomistic processes to achieve the transformation. μ-DIC results further suggest that although the final FCC-phase exhibits extensive dislocation density, it still accommodates plastic strain as deformation proceeds.

(2) The validity of the FCC-HCP-FCC sequential transformation was further explored in the $(Fe_{60}Mn_{40})_{100-x}Co_x$ alloys. In this ternary metastable alloy system, the first FCC-HCP transformation kinetics shows a positive dependency on the Co content. The FCC-HCP-FCC sequential transformation is validated in the $(Fe_{60}Mn_{40})_{85}Co_{15}$ alloy, in which the proposed random partial emission processes are consistent with the *in-situ* experimental observations. Furthermore, STEM results confirm the presence of basal stacking fault within the strain-induced HCP martensite, proving the operation of partial dislocation emission. A near-edge dislocation with mixed $\langle c \rangle$ and $\langle a \rangle$ components is also identified, which also implies the capability of non-basal plastic strain accommodation of the HCP-martensite.

(3) By further exploring the thermal stability of the strain-induced HCP-martensite, a latent strengthening mechanism that can also be achieved through a thermally-drive HCP-FCC reverse transformation. This kind of reverse transformation exhibits a displacive characteristic that can be activated at a relatively low temperature similar to the traditional BH treatment regime for a short period, but results in a simultaneous improvement in both strength and cumulative ductility. The analyses

suggest that the bake-reversion-hardening effect can be attributed to the improved stress delocalization capability and the enhanced phase boundary–dislocation interaction, which jointly brought about by the nucleation of secondary HCP-martensite variant.

Chapter 4: Plasticity Micro-mechanism-based Solutions

Portions of this chapter are based on:

[1] <u>S.L. Wei</u> et al., Deformation faulting in a metastable CoCrNiW complex concentrated alloy: A case of negative intrinsic stacking fault energy? **Acta Materialia**, 2020, 200: 992-1007.

Section 4.1: Motivations

The previous Chapter aims to explore phase transformation-based microstructural design concepts, primarily aims for FCC-HCP martensitic transformation. In an atomistic standpoint, such a displacive transformation is accomplished thourgh the emission of glissile Shockley partials on every other {111} planes. Such a mechanism, if takes place in a correlative mode, will eventually result in the formation of blocky HCP-martensite, which is the origin of micro-damage formation, as revealed in **Chapter 1**.

In light of this, a fundamental proposition could be asked: is it possible to delay the formation of blocky HCP-martensite, such that its detrimental effect can be mitigated? In other words, if the blocky HCP-martensite can be refined to infinitely thin, the aforementioned damage processes would be intrinsically resolved. The atomistic nature of FCC-HCP phase transformation therefore enables a "natural" solution by itself: HCP-martensite can indeed be one atomic-layer thin, which is then a layer of intrinsic stacking fault in FCC structure formed by single-step gliding of one glissile Shockley partial. It could be therefore expected that stacking fault formation by itself may become the major plasticity carrier once they are sufficiently stable.

To explore this proposition, an alloy solely undergoing FCC-HCP transformation is indispensable. Amongst the very few systems (He, Fe, Co, Tl, Pb, and Yb) that can undergo direct FCC-HCP transformation throughout the periodic table [106,107], Fe- and Co-based alloys have created profound interest in exploring improved mechanical performances and the underlying deformation micro-events [108–110]. The most conspicuous feature that distinguishes Co-rich system from others lies in its absence of body-centered cubic (BCC) structure in the corresponding phase diagram [107,111]. This kind of feature therefore inspires the selected model alloy system for **Chapter 4**, which is a metastable $Co_{60}Cr_{25}Ni_{10}W_5$ complex concentrated alloy (CCA).

Section 4.2: Results

Section 4.2.1: Uniaxial Tensile Response and Deformation Substructures

The quaternary CCA exploited for the present study exhibits a nominal composition of $Co_{60}Cr_{25}Ni_{10}W_5$ at. %. Its microstructure at the undeformed state is shown in **Figure 4.1**. This alloy demonstrates an equiaxed grain morphology with an average grain size of ~34 μm (**Figure 4.1 (a)** and **(b)**, excluding annealing boundaries), with a single FCC phase constitution. Further EDS elemental mapping taken across multiple grain boundaries confirms that all the four principal alloying elements exhibit spatially uniform distributions (**Figure 4.1 (c1)-(c4)**). As such, the influence of compositional inhomogeneity on the deformation modes can be excluded at the meso-scale.
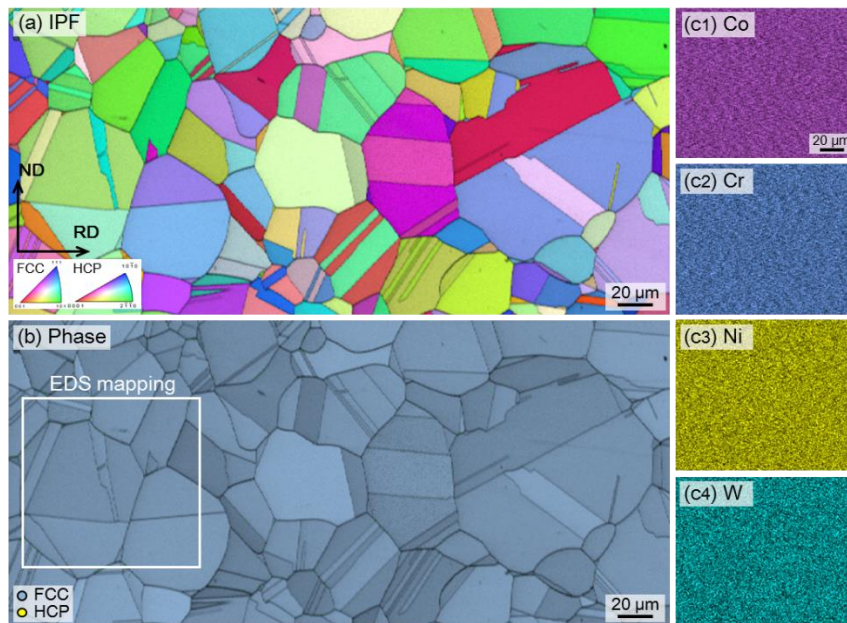
Figure 4.1: Microstructure of the $Co_{60}Cr_{25}Ni_{10}W_5$ alloy at the undeformed state. (a) EBSD inverse pole figure (IPF) showing the equiaxed grain morphology; (b) phase map confirming the single FCC-phase constitution; (c1)-(c4) EDS elemental mapping for Co, Cr, Ni, and W at the selected region denoted in (b), here the same scale bar is applied.

Figure 4.2 reveals the uniaxial tensile property of the $Co_{60}Cr_{25}Ni_{10}W_5$ CCA: it yields at ~498 MPa, followed by a pronounced strain hardening process (**Figure 4.2** (b)), reaching an ultimate tensile strength of ~1100 MPa and a fracture elongation of ~61.2 %. Compared with the commercial solid-solution or precipitation strengthened superalloys [112] with similar chemical constitutions, as well as the metastable FeMnCoCr HEAs [44,113] where extensive mechanically-induced martensitic

transformation takes place, a more improved strength-ductility is indeed achieved in the present CCA. Such intriguing mechanical properties render careful explorations of the underlying deformation micro-events, which will be detailed next, starting with post-mortem ECCI/EBSD analyses.
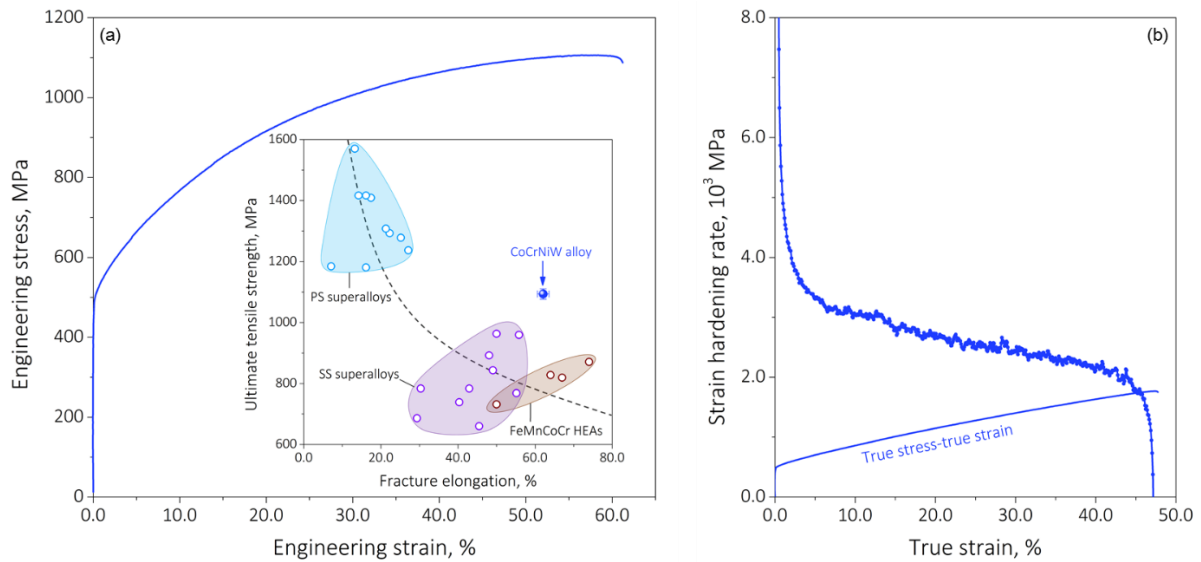
Figure 4.2: Mechanical response under uniaxial tensile loading. (a) Engineering stress-strain curve; (b) strain hardening rate chart. The inset of (a) demonstrates an Ashby comparison amongst the present $Co_{60}Cr_{25}Ni_{10}W_5$ CCA and commercial superalloys [112] as well as the latest metastable FeMnCoCr HEAs [44,113]. Abbreviation adopted: precipitation-strengthened (PS); solid-solution strengthened (SS).

Unlike the typical electron channeling contrast produced by the surface network of perfect dislocations in FCC crystals, ECCI micrographs here clearly reveal the presence of mono-layered planar-like features already at the low local strain levels (**Figure 4.3 (a)** and **(b)**). Here, a brief discussion of the imaging technique is required to clarify the underlying assumptions and uncertainties. It should be noted that while the ECCI technique demonstrates salient advantages in resolving crystalline defects with a broad view-of-field, inaccuracies or artifacts may potentially arise from its deficiency in enabling quantitative diffraction analysis of local sites [114]. To unambiguously distinguish the defect category, we present in **Figure 4.4** quantitative contrast profile assessments together with systematic comparisons to other representative deformation substructures, including perfect dislocations (both wavy and planar morphologies) and mechanically-induced martensite.
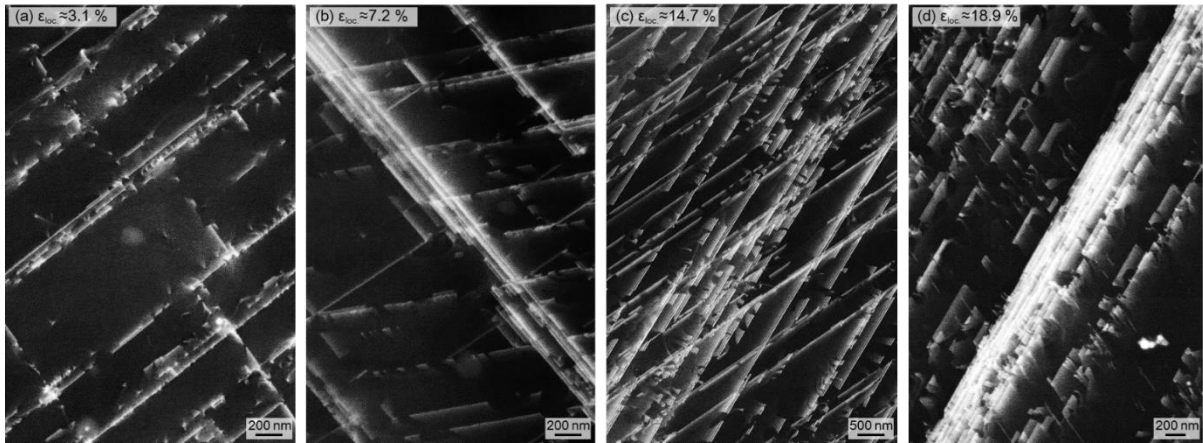
Figure 4.3: ECCI characterization of deformation substructures. (a)-(d) Stacking faults structures evolution with respect to increasing local strain level.
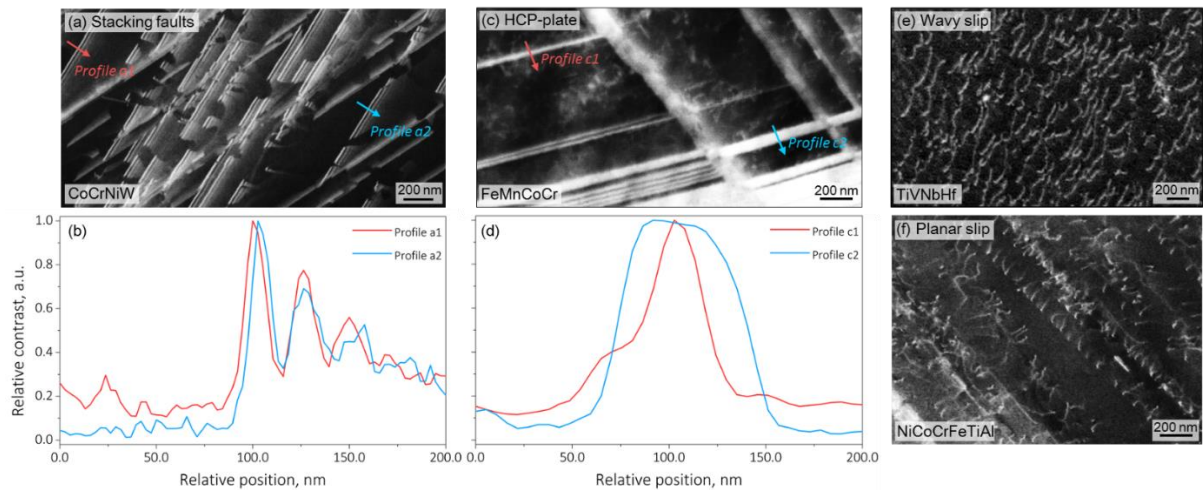
Figure 4.4: Comparison of deformation substructures identified by ECCI analyses. (a) and (b) Stacking faults; (c) and (d) thin HCP-martensitic plates [44]; (e) and (f) wavy [43] and planar [115] perfect dislocations.

Two distinctive features are subsequently recognized for the present planar-like structures, evidencing the fact that they are stacking faults: (1) compared with perfect dislocations, the channeling contrast they produce exists in a much wider planar regime (**Figure 4.4 (a), (b), (e)**, and **(f)**); and (2) the channeling contrast seen in **Figure 4.3** exhibits asymmetric characteristics, namely, a straight bright edge on one side with a smoothly fading contrast on the other, differing from the symmetric contrast produced by thin twins or martensitic plates (**Figure 4.4 (c), (d)** and Ref. [114]). With elevating local strain level, these stacking faults not only reveal an increasing trend in their densities but also the activation of different faulting systems (**Figure 4.3 (c)** and **(d)**). The latter, is confirmed from the intersections of unparalleled faulting plane traces (**Figure 4.3 (c)**). These results validate that in contrast

to the negligible role of perfect dislocation glide, stacking faults prevail in the present alloy at the examined deformation levels, which consolidates the quantification of their evolutionary features based on synchrotron X-ray diffraction technique (see next section).

By coupling EBSD and ECCI analyses in the region with an even higher local strain level of ~25.2 %, it is shown that at the length-scale of grain-size (**Figure 4.5 (a1)**), no clear trait of characteristic misorientation change that corresponds to mechanical twins or blocky HCP-martensite is observed from the inverse pole figure (IPF, **Figure 4.5 (b1)**) or phase map (**Figure 4.5 (c1)**). ECCI micrograph taken at a higher resolution again verifies that stacking faults belong to the $(1\bar{1}1)$ plane are densely populating in the grain interior, which diminishes the channeling condition.
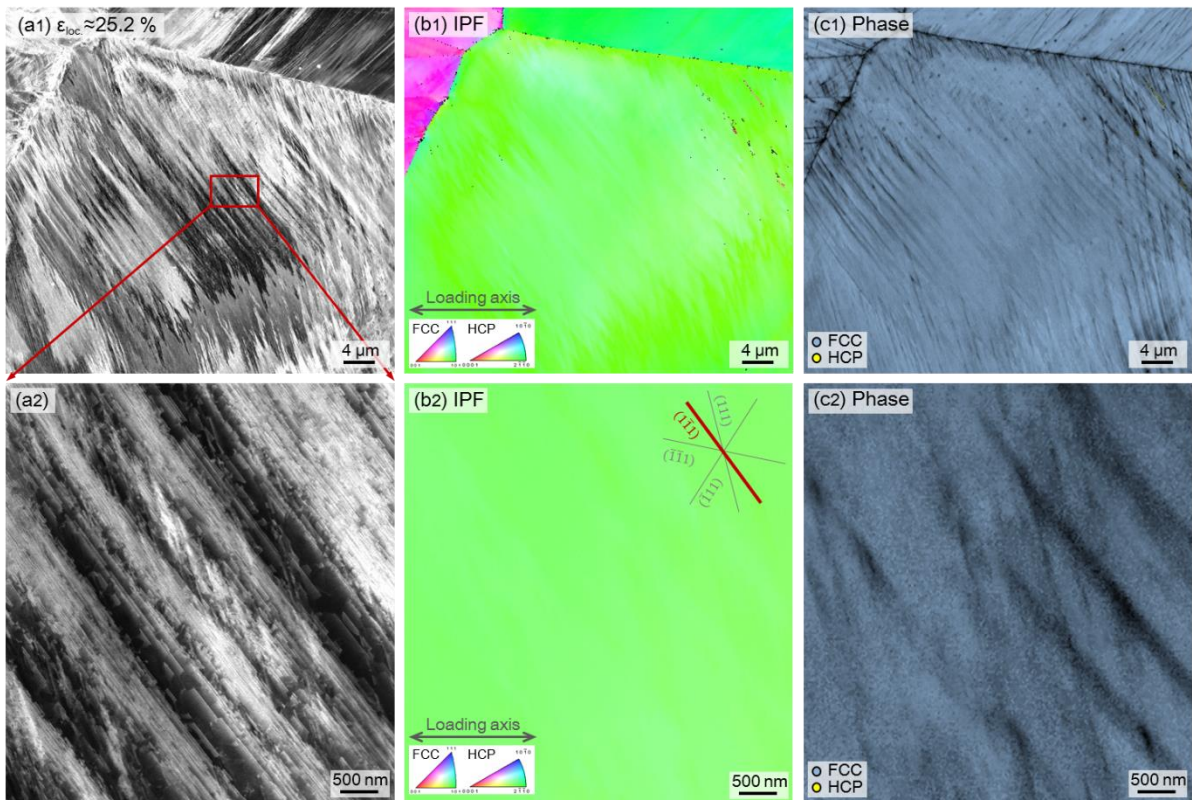
Figure 4.5: Coupled EBSD and ECCI analyses for stacking faults at a comparatively high local strain level of ~25.2 %. (a1) and (a2) Lower and higher magnification ECCI micrographs; (b2) and (b2) EBSD IPF maps eliminating the formation of nano-twins; (c1) and (c2) EBSD phase maps confirming the FCC structure in the observed region.

The corresponding EBSD results (**Figure 4.5 (b2)** and **(c2)**) also suggest the absence of twins or martensite in this region at the spatial resolution limit of ~30 nm. The foregoing deformation

substructures, if compared with perfect dislocation-mediated plasticity in conventional FCC-metals or mechanically metastable ones that exhibit twinning or martensitic transformation at a similar deformation level, can be concluded that it is the formation of an extensive amount of stacking faults that acts as the predominant mechanism accommodating macroscopic plastic strain. As such, in the following text, we exploit the term "deformation faulting" to comply with the mechanistic origin of this micro-event and the literature [116–118].

Section 4.2.2: *In-situ* Deformation Investigation via Synchrotron X-ray Diffraction

To assess the evolutionary characteristic of stacking faults and thereby to also quantify their roles in plastic deformation, the $Co_{60}Cr_{25}Ni_{10}W_5$ CCA was subjected to *In-situ* synchrotron X-ray analyses. **Figure 4.6** provides the integrated diffraction patterns along axial (parallel to loading axis) and radial (vertical to loading axis) directions with respect to elevating deformation level until macroscopic fracture, general features of which are briefly summarized in three respects, followed by more detailed discussions:

(1) while FCC-phase is maintained as the major phase constituent, additional peaks correspond to HCP-structure starts to appear at relatively higher strain levels (~25.0 % engineering strain);

(2) owing to the Poisson's contraction effect, diffraction peaks at the axial direction (**Figure 4.6 (a)**) shift to lower 2θ region (higher d-spacing) while the corresponding radial diffraction peaks (**Figure 4.6 (b)**) witness an opposite shifting trend;

(3) as plastic straining proceeds, the diffraction peaks exhibit distinctive variation in their intensities. Intriguingly, the intensity of the $(220)_{FCC}$ peak decreases and eventually vanishes at the later stage of deformation.

The variation in phase constitution during plastic deformation suggests that the present $Co_{60}Cr_{25}Ni_{10}W_5$ CCA exhibits mechanical metastability. To unambiguously quantify the phase fraction evolution and to complement the foregoing characterization by ECCI (**Figure 4.3** and **Figure 4.5**), we have evaluated the contents of these two present phases by both post-mortem EBSD analysis and Rietveld refinement of the two-dimensional *In-situ* diffractograms. As seen in **Figure 4.7**, the HCP-phase does not witness any discernable increase in its fraction before the deformation level exceeds ~40.0 % strain. The *In-situ* synchrotron X-ray diffraction results (**Figure 4.7 (e)**) confirm that the total HCP-phase fraction only

reaches ~6.0 % at ~65.0 % strain which is approximately the elongation-to-fracture (see the stress-strain curve in **Figure 4.2** (a)). It is also recognized from the EBSD phase maps that the HCP-phase mostly nucleates at grain boundaries (**Figure 4.7 (b)** and **(c)**) without eminently growing into blocky morphologies even at a comparatively high local strain level of ~70.8 %.
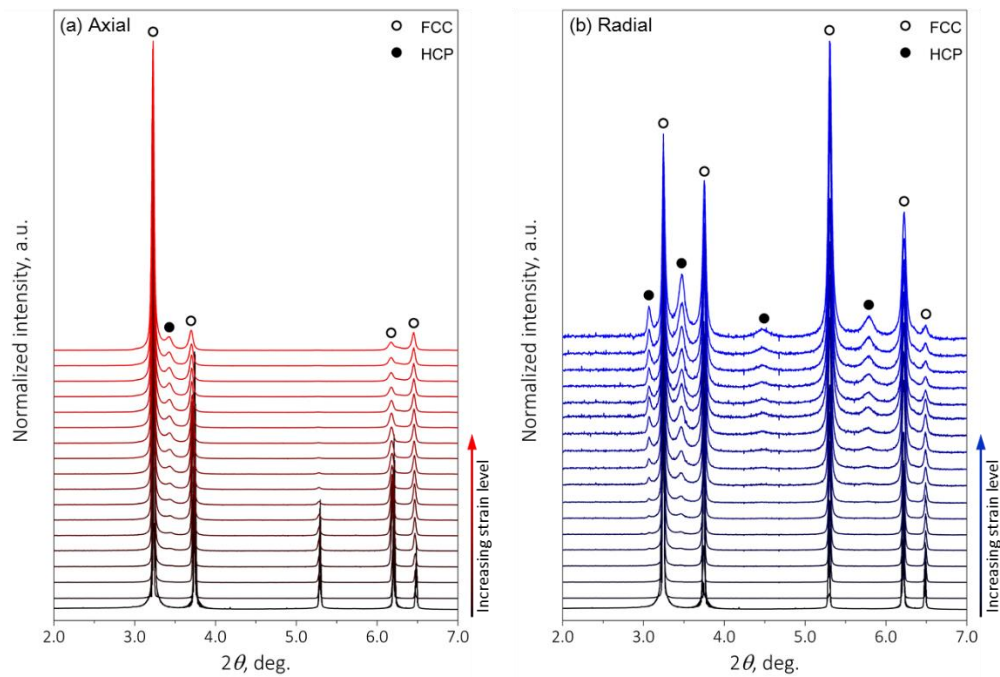
Figure 4.6: One-dimensional diffraction patterns integrated along (a) axial and (b) radial directions.
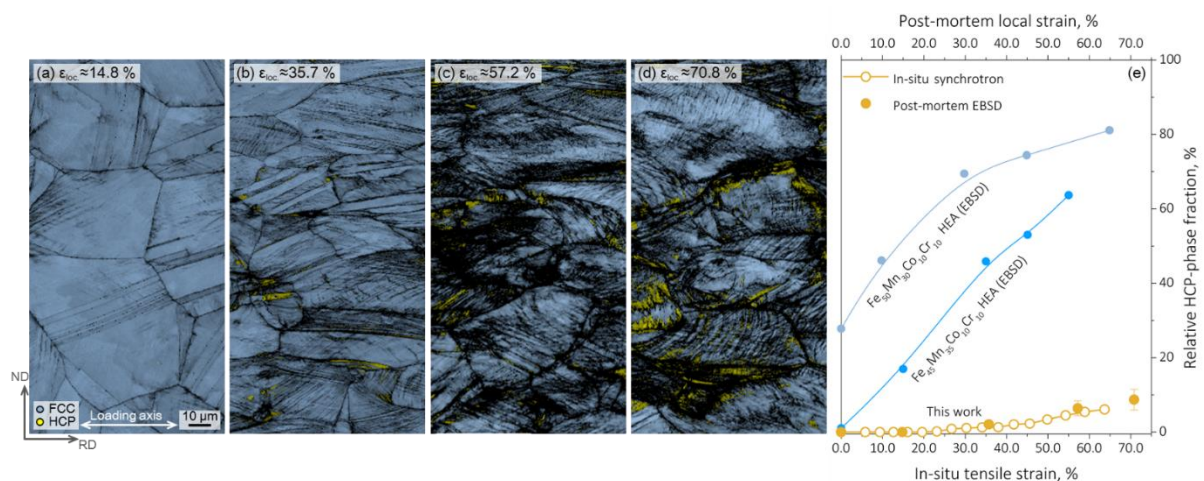
Figure 4.7: Assessment of phase stability during plastic deformation. (a)-(d) Post-mortem EBSD phase maps acquired at increasing local strain levels (the same scale bar is applied); (e) phase fraction variation as a function of deformation level. data for the FeMnCoCr HEAs are taken from the literature [44,113].

In comparison with typical quaternary FeMnCoCr-type HEAs [44,113] where the strain-induced FCC-to-HCP martensitic transformation is dominant in the whole plastic realm, the evidently low HCP-phase fraction with minute dimension, the highly sluggish formation rate, and the fact that it only operates at the later deformation stage, all lead to the conclusion that the prototypical mechanically-induced phase transformation is largely impeded and playing a minor role in the present $Co_{60}Cr_{25}Ni_{10}W_5$ CCA. As such, by combining the foregoing EBSD/ECCI characterizations (**Figure 4.3** and **Figure 4.5**) and the *In-situ* synchrotron X-ray measurement, it is therefore conclusive that deformation faulting indeed acts as the major micro-mechanism in accommodating external plastic strain. Atomistic correlation between faulting and the FCC-to-HCP martensitic transformation as well as the insights into metastable alloy design will be discussed in Section 4.3.

The peak shift due to external plastic loading is next exploited to calculate apparent lattice strain via:

$$\varepsilon_{hkl}^{app.} = \frac{d_{hkl} - d_{hkl}^o}{d_{hkl}^o}$$

(4.1)

where d_{hkl} and d_{hkl}^o respectively denote the d-spacing of plane hkl at a certain deformation level and the undeformed state. In the axial direction (**Figure 4.8** (a)), except for 311 plane, lattice strains in all other planes reveal a monotonic increasing trend as a function of elevating global tensile strain. Amongst them, 200 plane exhibits the most pronounced resistant to plastic deformation, which is characterized by the highest lattice strain throughout the experimental realm, being consistent with the typical behavior of FCC-metals [119,120]. 220 plane, in contrast, reveals the lowest lattice strain, suggesting the strongest propensity for plastic incipience. The corresponding intensity, on the other hand, also ceases to vanish as the global strain reaches ~30.0 %, which is largely ascribed to the deformation texture developed during plastic straining [118,119,121]. To uncover the mechanism for the anomaly drop of the lattice strain in the 311 plane (**Figure 4.8** (a)), we have assessed its sub-reflection units by de-convoluting the experimentally measured diffraction pattern at a representative higher strain level. The peak analysis results are demonstrated in **Figure 4.9**.
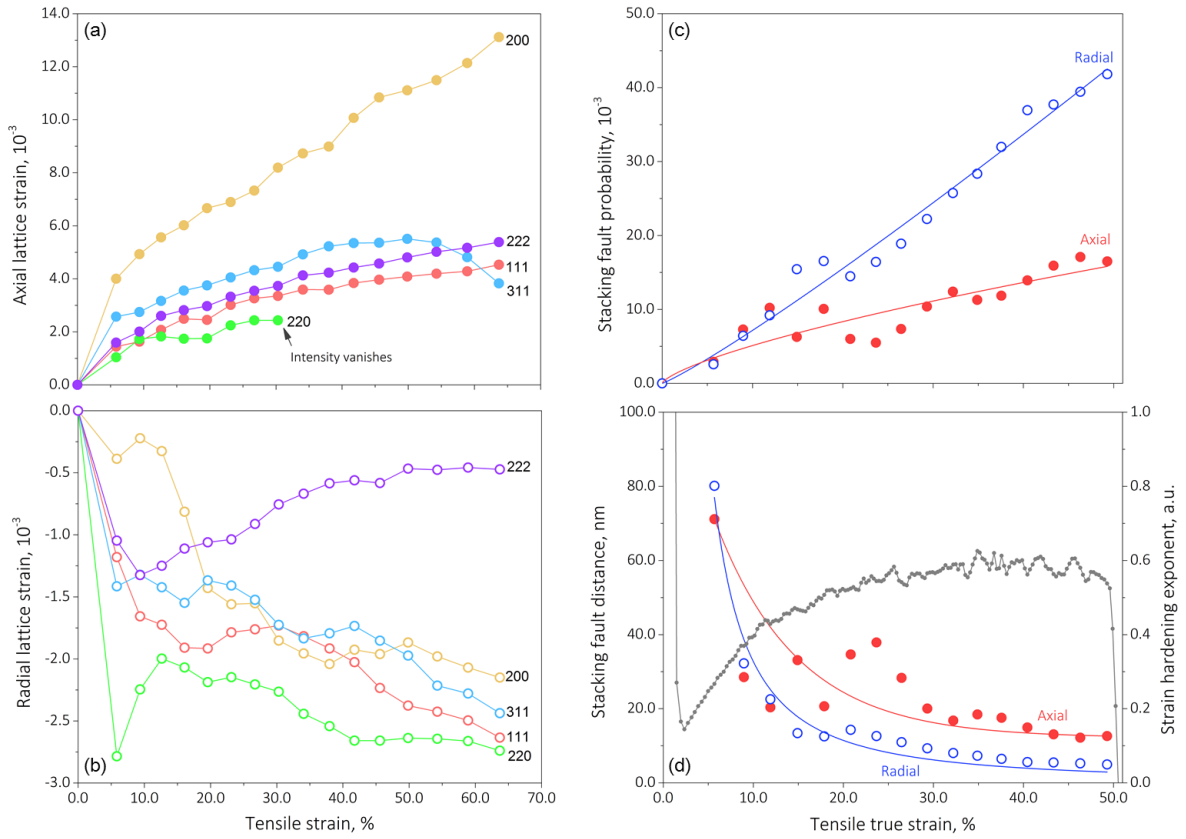
Figure 4.8: Quantitative analyses of the in-situ synchrotron X-ray diffractograms. (a) and (b) Axial and radial lattice strain evolution with as a function of increasing deformation level; (c) radial and axial stacking fault probability versus tensile true strain; (d) correlation between stacking fault distance reduction and strain hardening rate elevation.
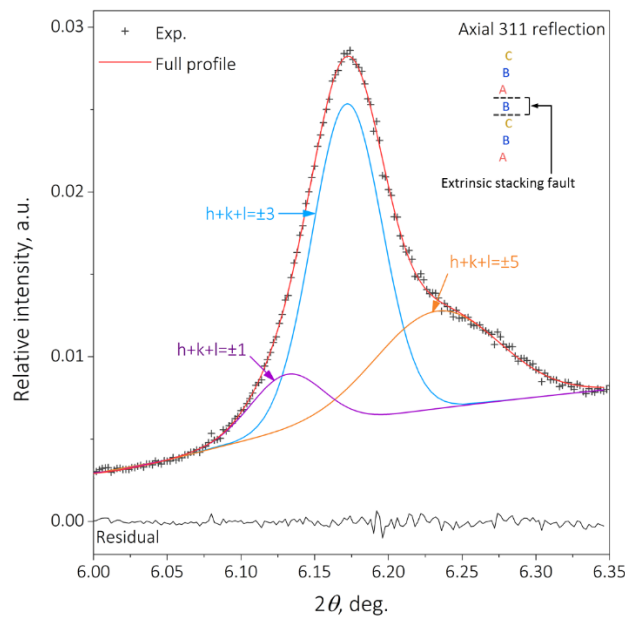
Figure 4.9 Peak analysis for the anomaly lattice strain drop in the 311 plane. Here the diffractogram was taken at a global strain level of ~65 %.

Figure 4.9 clearly reveals the asymmetry broadening of the 311 peak, which is characterized by the presence of a shoulder-like feature towards the higher 2θ region (lower d-spacing). To understand the origin of this broadening phenomenon, we de-convoluted the experimentally measured diffraction peak considering all possible sub-reflection units with: $h + k + l = \pm 5;\ \pm 3;\ \pm 1$. Since the full-width at half-maximum (FWHM) of the broadened component [122–124] is linearly proportional to $|h + k + l|$, it is recognized that the shoulder-like feature corresponds to sub-reflection unit with $h + k + l = \pm 5$. This sort of characteristic is consistent with the asymmetry broadening effect owing to the formation of substantial amounts of extrinsic stacking faults [122], which structurally involves sequential glide of Shockley partials on neighboring {111} planes (see the inset as a guide). As a result of this, the nominal 311 peak shifts to the higher 2θ region, phenomenologically leading to the decrease of d_{311}, which in turn causes the anomaly drop of lattice strain.

The presence of stacking faults also gives rise to the asymmetric evolution of lattice strains in 111 and 222 planes for both axial and radial directions, namely, the noticeable difference in the corresponding lattice strains provided their identical crystallographic symmetry. Note that while the Poisson's contraction effect renders negative lattice strain along the radial direction (**Figure 4.8** (b)), the distinction between $\varepsilon_{111}^{app.}$ and $\varepsilon_{222}^{app.}$ is still unambiguously resolved. In fact, according to diffraction theory [123,125], the lattice strain $\varepsilon_{hkl}^{app.}$ determined from apparent peak shift is comprised of two components:

$$\varepsilon_{hkl}^{app.} = \varepsilon_{hkl}^{sym.} - \frac{\sqrt{3}}{4\pi} \frac{\sum_b h+k+l}{(u+b)(h^2+k^2+l^2)} P_{sf} \tag{4.2}$$

in which, $\varepsilon_{hkl}^{sym.}$ originates from macroscopic straining and exhibits an elastic characteristic (regardless of crystalline defects), whereas, the inelastic portion $-\frac{\sqrt{3}}{4\pi} \frac{\sum_b h+k+l}{(u+b)(h^2+k^2+l^2)} P_{sf}$ is owing to the presence of stacking faults. Here u and b represent the number of unbroadened and broadened sub-reflection units in plane hkl, and P_{sf}, the stacking fault probability, is a direct measurement of the fraction for uncorrelated stacking faults within the tested specimen. Since $\varepsilon_{111}^{sym.}$ and $\varepsilon_{222}^{sym.}$ are identical in 111 and 222 planes, the corresponding P_{sf} can be expressed as an explicit function of the apparent lattice strains:

$$P_{sf} = \frac{32\pi}{3\sqrt{3}}\left(\varepsilon_{222}^{app.} - \varepsilon_{111}^{app.}\right) \tag{4.3}$$

As presented in **Figure 4.8** (c), the calculated P_{sf} of both axial and radial directions demonstrates a significant increase with respect to elevating deformation level, respectively reaching 15.8×10⁻³ and 42.3×10⁻³ before macroscopic failure takes place. Theses P_{sf} quantities are particularly higher than those determined from FCC-structured alloys where perfect dislocation glide [118] operates as the major plastic deformation mode, suggesting the salient role of extensive stacking fault formation (also see **Figure 4.3** and **Figure 4.5** as reference). It should be pointed out that since synchrotron X-ray appears rather deficient in unambiguously distinguishing the contribution between perfect and partial dislocations, the *a priori* condition of solely applying **Eq. (4.3)** in the analyses lies in the validation of negligible activity of perfect dislocations via complementary experiments. A rationally reliable verification exploited in the present study is the ECCI characterizations presented in **Figure 4.3** and **Figure 4.5** as well as later **Figure 4.13** and **Figure 4.14**, in which stacking faults formation prevails at various deformation levels, while perfect dislocation glide is almost completely suppressed. Interestingly, while the P_{sf} in the present alloy is almost comparable to that of metastable HEAs which exhibit pronounced strain-induced FCC-to-HCP martensitic transformation [52,77], the resultant HCP-phase fraction, however, remains an order of magnitude lower. Since P_{sf}, by definition [125], also reflects the frequency of finding a deformation fault along the close packing 111 planes in FCC stacking sequence, a microstructure-related quantity, the average stacking fault distance, can also be determined as:

$$d_{sf} = d_{111}/P_{sf} \tag{4.4}$$

where d_{111} is the apparent spacing of 111 planes at a given deformation level. Along both axial and radial directions, the d_{sf} values demonstrate ~80 nm at a comparatively moderate strain level, followed by an evident decrease down to ~10 nm at the later stage of deformation (**Figure 4.8** (d)), complying with the qualitative trend revealed by ECCI analyses (**Figure 4.3** and **Figure 4.5**). The associated strain hardening exponent ($n = \partial \ln\sigma^{true}/\partial \ln\varepsilon^{true}$), on the other hand, exhibits an eminent

increase up to ~0.5 within the true strain realm of 0.0-20.0 %, where the d_{sf} also witnesses the most pronounced reduction. This kind of latent correlation demonstrates the strain hardening caused by the faulting mechanism, for which a more detailed mechanistic consideration is provided in Section 4.2.2.

Section 4.3: Analyses and Discussion

Section 4.3.1: Intrinsic Stacking Fault Energy in Metastable FCC alloys

This section will explore the fundamental origin for the operating deformation faulting activity. The section is developed into two portions. First, theoretical considerations will be detailed regarding the correlation between intrinsic stacking fault energy and deformation micro-mechanisms in metastable FCC alloys. Second, experimental verifications will be presented to further support the proposed mechanisms.

The activation of plastic deformation modes in bulk FCC-structured alloys, including perfect dislocation glide, mechanically-induced twinning or martensitic transformation has been well-documented to exhibit a close correlation to intrinsic stacking fault energy (γ_{iSFE}). From an atomistic standpoint, the γ_{iSFE} quantifies the propensity of nucleating an intrinsic stacking fault via dissociating a perfect $a/2\langle 110 \rangle$ dislocation into two paired $a/6\langle 112 \rangle$ glissile Shockley partials. The mobility and thereby the interactions amongst these partials serve as the operative unit in triggering deformation twinning or martensitic transformation. Thus far, numerous investigations of Al- Cu- and Fe-Mn-based alloys have rendered empirical indications [126,127] of the operating deformation mode implied by the magnitude of γ_{iSFE}:

(1) for comparatively low $\gamma_{iSFE} < 20 \ mJ/m^2$, mechanically-induced FCC-HCP or FCC-HCP-BCT martensitic transformation occurs;

(2) for medium γ_{iSFE} in $20{\sim}40 \ mJ/m^2$ range, deformation twinning operates;

(3) for high $\gamma_{iSFE} > 40 \ mJ/m^2$ perfect dislocation glide becomes predominant.

Unlike the foregoing three situations, the present $Co_{60}Cr_{25}Ni_{10}W_5$ CCA reveals an evident faulting response, which phenomenologically suggests that the formation of stacking faults should be the most effective micro-mechanism in leading to energy dissipation during plastic deformation. Clearly, this sort of peculiar deformation response leads to a more dedicated assessment of the γ_{iSFE}. Since the present investigation was carried out at ambient temperature, and considering the fact that the chemical complexity may impede precise *ab-initio* calculations, we next assess the γ_{iSFE} in the viewpoint of thermodynamics. Structurally, the nucleation of a mono-layered intrinsic stacking fault in bulk FCC-

crystals is in equivalent to creating an HCP stacking unit along with coherent FCC/HCP interfaces. The γ_{iSFE}, in this regard, is considered as the excess free-energy, according to the Olson-Cohen model [28]:

$$\gamma_{iSFE} = 2\rho_{111}\Delta G^{FCC \to HCP} + 2\sigma^{FCC/HCP} \tag{4.5}$$

where ρ_{111}, $\Delta G^{FCC \to HCP}$, and $\sigma^{FCC/HCP}$ respectively denote the atomic density of the 111 faulting plane, the Gibbs free-energy difference between FCC and HCP phases, and the coherent interfacial energy. Here, since $\rho_{111} = \frac{4}{\sqrt{3}}\frac{1}{a^2 N_A}$ and $\sigma^{FCC/HCP} \sim 7.5 \ mJ/m^2$ for coherent interfaces [28] are both fixed constants, the only factor in **Eq. (4.5)** remains to be determined is the $\Delta G^{FCC \to HCP}$. Considering the chemical complexity of the present system, we estimate this quantity by adopting a sub-regular solution formalism [128,129]:

$$\Delta G_{total}^{FCC \to HCP} = \Delta G_{p.m.}^o + \Delta G^{ex.} \tag{4.6}$$

Here, $\Delta G_{p.m.}^o$ represents the Gibbs free-energy difference between FCC and HCP phases at the reference state, which takes the form of weighted average amongst all the alloying elements:

$$\Delta G_{p.m.}^o = \sum_i x_i \Delta G_i^{FCC \to HCP} \tag{4.7}$$

where x_i is the atomic fraction of the ith element and $\Delta G_i^{FCC \to HCP}$ the corresponding Gibbs free-energy difference between FCC and HCP structures. The total excess free energy term $\Delta G^{ex.}$ in **Eq. (4.6)** is modeled as the summation of binary ($\Delta G_{bin.}^{ex.}$) and ternary ($\Delta G_{tern.}^{ex.}$) interactive terms as well as the magnetic contribution ($\Delta G_{mag.}^{ex.}$):

$$\Delta G^{ex.} = \Delta G_{bin.}^{ex.} + \Delta G_{tern.}^{ex.} + \Delta G_{mag.}^{ex.} \tag{4.8}$$

Specifically, for binary excess free-energy:

$$\Delta G_{bin.}^{ex.} = \sum_{i,j} x_i x_j \Omega_{ij}^{FCC \to HCP} \tag{4.9}$$

Where the interactive coefficient Ω_{ij} takes the polynomial form:

$$\Omega_{ij} = \sum_{m=0}^{l} L_{ij,m}(x_i - x_j)^m \qquad (4.10)$$

Similarly, the ternary excess free-energy is modeled via:

$$\Delta G_{tern.}^{ex.} = \sum_{i,j,k} G_{ijk}^{E,FCC \to HCP} \qquad (4.11)$$

Considering the Co-rich characteristic of the present CCA, magnetic contribution to the total excess free-energy should also be taken into account:

$$\Delta G_{mag.}^{ex.} = G_{mag.}^{HCP} - G_{mag.}^{FCC} \qquad (4.12)$$

Here magnetic free-energy of a certain phase k is calculated via the Hillert-Jarl model [130]:

$$G_{mag.}^{k} = RT\ln(1 + \beta^k)\Gamma(t) \qquad (4.13)$$

Here β^k is the Bohr magneton number which takes the form of the following polynomial:

$$\beta^k = \sum_i \beta_{\Theta,i} x_i + \sum_{i,j} \sum_{m=0}^{l} \beta_{ij,m}(x_i - x_j)^m \qquad (4.14)$$

In **Eq. (4.13)**, t represents the normalized Curie temperature at a given temperature T:

$$t = \frac{T}{T_c^k} \qquad (4.15)$$

The intrinsic Curie temperature of phase k can be calculated as:

$$T_c^k = \sum_i T_{\Theta,i} x_i + \sum_{i,j} \sum_{m=0}^{l} T_{ij,m} (x_i - x_j)^m \tag{4.16}$$

Where $\Gamma(t^k)$ is a step-wise function depending on the dimensionless Curie temperature [130]:

If $t^k > 1$:

$$\Gamma(t^k) = -\left(\frac{t^{-5}}{10} + \frac{t^{-15}}{315} + \frac{t^{-25}}{1500}\right)\Big/A \tag{4.17}$$

If $t^k \leq 1$:

$$\Gamma(t^k) = 1 - \left[\frac{79t^{-1}}{140B} + \frac{474}{140B}(B^{-1} - 1)\left(\frac{t^3}{6} + \frac{t^9}{135} + \frac{t^{15}}{600}\right)\right]\Big/A \tag{4.18}$$

In Eqs. (4.17) and (4.18) $A = 2.34$ and $B = 0.28$ for FCC and HCP phases [130,131]. The following **Table 4.1** to **Table 4.4** summarizes the analytical format of individual terms exploited in the sub-regular solution model (see **Eqs**. **(4.6)**-**(4.8)**) as well as the referencing details.

Table 4.1: Thermodynamic parameters adopted for reference state Gibbs free-energy difference calculation.

Term	Equation	Ref.
$\Delta G_{Co}^{FCC \to HCP}$	$-427.59 + 0.615T$	[132]
$\Delta G_{Cr}^{FCC \to HCP}$	$-2846 - 0.163T$	[132]
$\Delta G_{W}^{FCC \to HCP}$	$-4550 - 0.629T$	[132]
$\Delta G_{Ni}^{FCC \to HCP}$	$1046 + 1.255T$	[132]

Table 4.2: Thermodynamic parameters adopted for binary excess free-energy calculation. N.A. denoted the quantities that to the best of our literature search, are not available.

Term	Equation	Ref.
$\Omega_{CoCr}^{FCC \to HCP}$	$-4621.59 + 7.32T + (7341.73 - 7.93T)(x_{Co} - x_{Cr})$	[131]
$\Omega_{CoW}^{FCC \to HCP}$	$-2191.38 + 4.34T + (4068.16 - 3.56T)(x_{Co} - x_W) + (7624.18 - 4.53T)(x_{Co} - x_W)^2$	[133,134]
$\Omega_{CoNi}^{FCC \to HCP}$	$-820 - 1.648T$	[135]
$\Omega_{CrNi}^{FCC \to HCP}$	$27 + 12.10T + (-19895 + 16.384T)(x_{Cr} - x_{Ni})$	[136]
$\Omega_{CrW}^{FCC \to HCP}$	--	N.A.
$\Omega_{WNi}^{FCC \to HCP}$	--	N.A.

Table 4.3: Thermodynamic parameters adopted for ternary excess free-energy calculation. N.A. denoted the quantities that to the best of our literature search, are not available.

Term	Equation	Ref.
$G_{CoCrW}^{E,FCC\rightarrow HCP}$	$(-5000x_{Co})x_{Co}x_{Cr}x_W$	[136]
$G_{CoCrNi}^{E,FCC\rightarrow HCP}$	$(-28Tx_{Cr})x_{Co}x_{Cr}x_{Ni}$	[135]
$G_{CoWNi}^{E,FCC\rightarrow HCP}$	--	N.A.
$G_{CrWNi}^{E,FCC\rightarrow HCP}$	--	N.A.

Table 4.4: Thermodynamic parameters adopted for the magnetic contribution to the excess free-energy. Approximation is taken to the second order

Term	Equation	Ref.
$T_{c,Co}^{FCC}$	1396	[132]
β_{Co}^{FCC}	1.35	[132]
$T_{c,Co}^{HCP}$	1396	[132]
β_{Co}^{HCP}	1.35	[132]
$T_{c,CoCr}^{FCC}$	$1396x_{Co} - 1109x_{Cr} - 9392.53x_{Co}x_{Cr} + 8383.04(x_{Co} - x_{Cr})x_{Co}x_{Cr}$	[131]
β_{CoCr}^{FCC}	$1.35x_{Co} - 2.46x_{Cr}$	[131]
$T_{c,CoCr}^{HCP}$	$1396x_{Co} - 1109x_{Cr} - 5828.68x_{Co}x_{Cr} + 4873.95(x_{Co} - x_{Cr})x_{Co}x_{Cr}$	[131]
β_{CoCr}^{HCP}	$1.35x_{Co} - 2.46x_{Cr}$	[131]
$T_{c,CoNi}^{FCC}$	$1396x_{Co} + 633x_{Ni} + 411x_{Co}x_{Ni} - 99(x_{Co} - x_{Ni})x_{Co}x_{Ni}$	[135]
β_{CoNi}^{FCC}	$1.35x_{Co} + 0.52x_{Ni} + 1.046x_{Co}x_{Ni} + 0.165(x_{Co} - x_{Ni})x_{Co}x_{Ni}$	[135]
$T_{c,CoNi}^{HCP}$	$1396x_{Co} + 633x_{Ni} + 411x_{Co}x_{Ni} - 99(x_{Co} - x_{Ni})x_{Co}x_{Ni}$	[135]
β_{CoNi}^{HCP}	$1.35x_{Co} + 0.52x_{Ni} + 1.046x_{Co}x_{Ni} + 0.165(x_{Co} - x_{Ni})x_{Co}x_{Ni}$	[135]
$T_{c,CoW}^{FCC}$	$1396x_{Co}$ $- 3520.31x_{Co}x_W - 4796.2(x_{Co} - x_W)x_{Co}x_W - 813.66(x_{Co} - x_W)^2x_{Co}x_W$ $+ 5699.83(x_{Co} - x_W)^3x_{Co}x_W$	[133,134]
β_{CoW}^{FCC}	$1.35x_{Co} - 2.93x_{Co}x_W - 4.77(x_{Co} - x_W)x_{Co}x_W - 4.55(x_{Co} - x_W)^2x_{Co}x_W$ $+ 10.14(x_{Co} - x_W)^3x_{Co}x_W$	[133,134]
$T_{c,CoW}^{HCP}$	$1396x_{Co} - 3159.19x_{Co}x_W - 4023.37(x_{Co} - x_W)x_{Co}x_W$ $+ 200.52(x_{Co} - x_W)^2x_{Co}x_W + 5538.65(x_{Co} - x_W)^3x_{Co}x_W$	[133,134]
β_{CoW}^{HCP}	$1.35x_{Co} - 2.93x_{Co}x_W - 4.77(x_{Co} - x_W)x_{Co}x_W - 4.55(x_{Co} - x_W)^2x_{Co}x_W$ $+ 10.14(x_{Co} - x_W)^3x_{Co}x_W$	[133,134]

The corresponding calculation results are illustrated as a function of temperature in **Figure 4.10 (a)** and **(b)**. Clearly, the $\Delta G_{total}^{FCC\rightarrow HCP}$ exhibits a negative quantity with a slight monotonic increase within the ambient temperature range (**Figure 4.10 (a)**), suggesting the thermodynamically metastable feature of the present FCC-phase. Amongst all the constitutions considered in the sub-regular solution model, it is also recognized that the $\Delta G_{p.m.}^o$ term, which reflects the intrinsic ideal mixing tendency of the alloying elements, demonstrates the most predominant contribution. The higher order non-linear interactions, including $\Delta G_{bin.}^{ex.}$, $\Delta G_{tern.}^{ex.}$, and $\Delta G_{mag.}^{ex.}$, on the other hand, render comparatively minor

effects. The resultant γ_{iSFE} calculated from **Eq. (4.5)** also reveals a negative value at ambient temperature (**Figure 4.10 (b)**), reaching $-53.35 \; mJ/m^2$ at 25 ℃, being well accord with the ground state *ab-initio* prediction by Tian et al. [137] Notably, these calculation results seem contradictory with classical dislocation theory that persists an always positive γ_{iSFE}. We assert, however, negative γ_{iSFE} also exhibits a salient physical revelation, which will be detailed next from the perspectives of thermodynamics, structure, and mechanics.
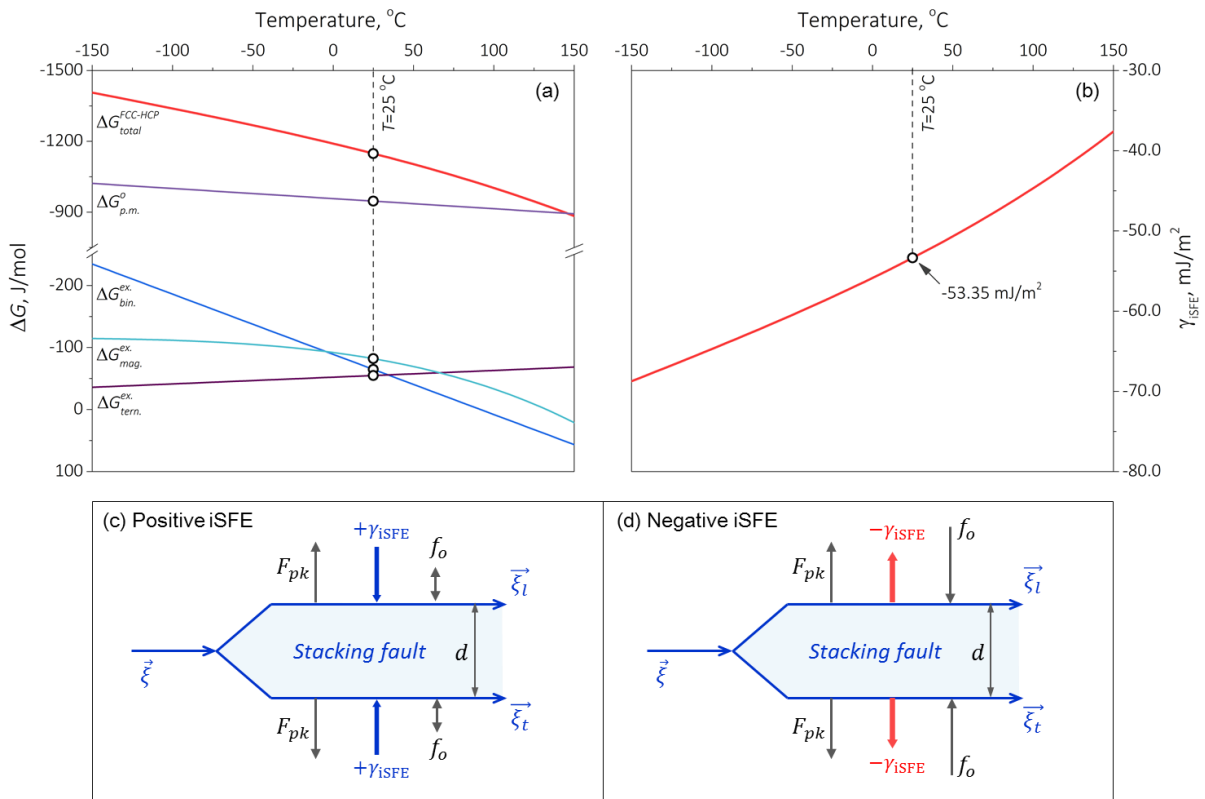
Figure 4.10: Thermodynamic assessment of the Co₆₀Cr₂₅Ni₁₀W₅ CCA. (a) Phase stability assessment in the sub-regular solution formalism; (b) estimating of intrinsic stacking fault energy as a function of temperature; (c) and (d) stress-free equilibrium considering positive and negative intrinsic stacking fault energies.

Thermodynamically, according to **Eq. (4.5)** γ_{iSFE} is exactly the excess formation energy associated with the nucleation of stacking faults. Classically, a positive γ_{iSFE} implies that creation of a faulted 111 player in FCC stacking sequence will lead to free-energy elevation even after overcoming the kinetic energy barrier assisted by external loading [28]. This kind of free-energy increase will cease to be alleviated by the immediate formation of more stable bulk phase or structure in a sense to comply with the law of energy dissipation for plasticity. As such, creation of mono-layered stacking faults

(namely, deformation faulting) can barely become predominant in the plastic deformation for alloys that exhibit positive γ_{iSFE}. Instead, features like HCP-martensite or twins, whose formation can be aided by stacking faults will become prevalent, and this, as discussed earlier, has been well-verified in classical Fe-Mn-based alloys. A negative γ_{iSFE}, on the other hand, suggests that the faulted 111 layer is more energetically favorable than the perfect FCC stacking sequence. That stated, mechanically nucleating even a mono-layered stacking fault is already a micro-plasticity event that dissipates strain energy. Under this energetic framework, it is expected that extensive amounts of uncorrelated stacking faults can become thermodynamically stable in the plastic regime, microscopically giving rise to the deformation faulting response as demonstrated in **Figure 4.3**, **Figure 4.5**, and **Figure 4.8**. Only at comparatively higher deformation levels, i.e. when the energy dissipation caused by individual faulting unit can no longer compensate the free-energy increase due to the interaction amongst the stacking faults (see next section), will the formation of other bulk structures start to take place. This is also the phenomenological reason why compared to the Fe-Mn-based alloys with positive γ_{iSFE}, blocky HCP-martensite nucleation in the present $Co_{60}Cr_{25}Ni_{10}W_5$ CCA is significantly delayed (**Figure 4.7 (e)**).

Structurally, the proposition that needs to be addressed is whether or not the extended dislocation still complies with the stress-free equilibrium criterion in light of a negative γ_{iSFE}? As schematically shown in **Figure 4.10 (c)** and **(d)**, such a structure consists of one layer of stacking fault enclosed by a leading $(\vec{\xi_l})$ and a trailing $(\vec{\xi_t})$ glissile Shockley partial that dissociate from a perfect dislocation $(\vec{\xi})$. Since the elastic strain energy in the FCC crystal, according to the Frank's criterion [90], is alleviated by the creation of Shockley partials, the underlying Peach-Kohler interaction always results in a repulsive force ($F_{pk} \propto 1/r$, r is the separation distance) between two paired partials. In the case of positive γ_{iSFE} (**Figure 4.10 (c)**, for most stable FCC alloys), as the creation of a stacking fault leads to free-energy increase, the resultant interactive effect gives rise to an attractive force, tending to shrink the stacking fault. By presuming that the lattice frictional force (f_o) is negligibly small, the stress-free equilibrium is therefore achieved between the repulsive Peach-Kohler force and the attractive force originating from the stacking fault, enabling an equilibrium stacking fault width (d) [90]:

$$d = \frac{G}{2\pi\gamma_{iSFE}}\left[(\vec{b_l}\cdot\vec{\xi_l})(\vec{b_t}\cdot\vec{\xi_t}) + \frac{(\vec{b_l}\times\vec{\xi_l})(\vec{b_t}\times\vec{\xi_t})}{1-\nu}\right] \tag{4.19}$$

where, $\vec{b_l}$ and $\vec{b_t}$ are the Burgers vectors of the leading and the trailing partials, G and ν denoted the shear modulus and the Poisson's ratio of the alloy. Practically, **Eq. (4.19)** has also revealed broad application in determining γ_{iSFE} via high-resolution TEM experimentation [138–141]. In the case of negative γ_{iSFE} (**Figure 4.10** (d)), by contrast, a repulsive force is then associated with the formation of stacking fault, exhibiting the trend to extend its width. Critically, the stress-free equilibrium described by **Eq. (4.19)** breaks down. However, as seen in the experimental results in **Figure 4.3** and **Figure 4.5** (and later **Figure 4.13** and **Figure 4.14**), stacking fault structures do reach mechanical equilibrium even when the external load is removed. We therefore assert that in metastable FCC alloys with negative γ_{iSFE}, it is the lattice frictional force that serves to balance the foregoing two repulsive forces, preserving the finite partial separation width. While a quantitative validation of such a hypothesis for the current CCA requires dedicated modeling effort, previous theoretical investigation by Baudouin et al. [142] does confirm the significant role of lattice frictional force in the equilibrium stacking fault width. It is worthwhile noting that γ_{iSFE} determination of metastable FCC alloys on the theoretical basis of **Eq. (4.19)** or its variations may largely deviate from the actual scenario, leading to contradictory explanations of the operative deformation micro-mechanisms.

Mechanically, the negative γ_{iSFE} is of fundamental significance, straightforwardly in the viewpoint of generalized stacking fault energy (GSFE) [105,143], or more broadly, the deformation energy landscape [144]. The essence of GSFE lies in the description of energy change per unit area upon shearing a certain crystal along an intended strain path [105]. As such, the resultant energy-atomistic displacement curve, if achieved along the $\{111\}\langle112\rangle$ path, measures the energy landscape of nucleating a partial dislocation, along which the energy corresponds to $|a/6\langle112\rangle|$ is the γ_{iSFE} discussed above. Under this theoretical framework, a negative γ_{iSFE} thus implies:

(1) operation of partial dislocation glide becomes predominant;

(2) after overcoming an energy barrier, namely the unstable stacking fault energy γ_{uSFE}, the faulted crystal becomes more stable compared to its defect-free counterpart, being compatible with the thermodynamic understanding;

(3) successive formation of stacking faults (in equivalent to correlated mono-layered HCP stacking) will tend to destabilize the original metastable FCC structure, giving rise to the formation of HCP-

phase.

It is worthwhile noting that, consistent with the foregoing thermodynamic calculation (**Figure 4.10 (b)**), ground state GSFE computation [137] of individual alloying effect for Ni, Cr, or W in a Co-matrix all demonstrates negative γ_{iSFE} with less 50 at. % content, which is supportive of both the observed deformation substructures (**Figure 4.3** and **Figure 4.5**) and the metastability nature of the present alloy. Still, as implied by the GSFE formalism, whether or not faulting can become the most predominant deformation micro-mechanism also relies on the energy barrier term (γ_{uSFE}). A more recent simulation work by Jo et al. [145] proposed $\gamma_{iSFE}/(\gamma_{uSFE} - \gamma_{iSFE})$ as an inherent indicator for the operative deformation mode, in which a nominally negative value signifies the occurrence of significant faulting event, being consistent with our experimental observation. From a continuum mechanics perspective, such a latent correlation has also been established via the classical dislocation theory, according to Lagerlof et al. [146]:

$$\tau_c = \frac{2\alpha G b_p}{D} + \gamma_{iSFE}/b_p \tag{4.20}$$

here, τ_c is represents the critical resolved stress for nucleating a glissile Shockley partial ($\tau_c \sim |\nabla\gamma|_{max}$ in the viewpoint of GSFE) which is an explicit function of dislocation category (α), shear modulus (G), grain size (D), magnitude of Burgers vector (b_p), and γ_{iSFE}. Evidently, negative γ_{iSFE} exhibits the trend to mitigate τ_c, which in turn facilitates the nucleation of partial dislocations.

By clarifying the thermodynamic, structural, and mechanical implications γ_{iSFE}, we now propose the following three assertions regarding the deformation response for metastable FCC alloys with significantly negative γ_{iSFE}:

(1) compared with perfect dislocation glide, operation of glissile Shockley partials becomes predominant, giving rise to deformation faulting;

(2) the extension of stacking fault via the emission of glissile partials exhibits a mechanically irreversible characteristic;

(3) the bulk FCC phase will demonstrate a somewhat metastable feature, but the formation of blocky-HCP structure is presumably delayed.

The foregoing postulates (1) and (3) can be naturally deduced from the structural and thermodynamic discussion proposed above, and their validity has already been confirmed in the Results section. Intriguingly, the second postulate which is drawn from a thermodynamic-mechanical aspect, enables the design of an in-situ ECCI experiment for validation. The experiment consists of assessing the variation in stacking fault length during elastic tension loading-unloading cycle, intended to examine whether or not the creation of stacking faults is indeed an energetically favored micro-event as dictated by the negative γ_{iSFE} and **Eq. (4.19)**.

However, before detailed experimental investigation, a few points regarding the exploited ECCI technique need to be noted. As discussed earlier, while in-situ mechanical testing coupled with ECCI enables the elucidation of deformation substructure evolution with a broader view-of-field, potential artifacts or inaccuracies in the current investigation may potentially arise from three major respects:

(1) tensile stage or sample tilting can alter the imaging condition, causing an overestimation of stacking fault density, which is owing to the variation in channeling contrast;

(2) the polycrystallinity nature of the investigated alloy can render heterogeneous local stress distribution, leading to the deviation from global stress state, which in turn diversifies the local stacking fault activity;

(3) interstitial elements can give rise to Suzuki segregation [90,147], also contributing to the irreversible extension of the stacking fault.

For (1), we present below a systematic evaluation of the systematic error calibration results. In **Figure 4.11** a representative area of interest is employed for ECC-imaging to clarify how the imaging condition would be affected with respect to sample and/or stage misalignment. Both positive (**Figure 4.11 (a1)**-**(a4)**) and negative (**Figure 4.11 (c1)**-**(a4)**) tilting are intentionally carried out in the *z-o-y* plane, and the corresponding ECCI micrographs are recorded. In comparison to the optimal imaging condition shown in **Figure 4.11** (b), the tilted conditions shown in **Figure 4.11 (a2)-(a4)** and **Figure 4.11 (c2)-(c3)** all reveal apparently diminished channeling contrast, for which quantitative assessments are presented in **Figure 4.12**. It is recognized from the statistical assessment that any sample and/or stage tilting within $\pm 1.5^{\circ}$ will only lead to the underestimation of the total stacking fault density (defined as: $\rho_{sf} = \sum length\ of\ the\ stacking\ fault\ traces / A_{obv.}$). This rationally eliminates the artifact of stacking

fault density increase owing to the variation in channeling condition during the in-situ ECCI testing.
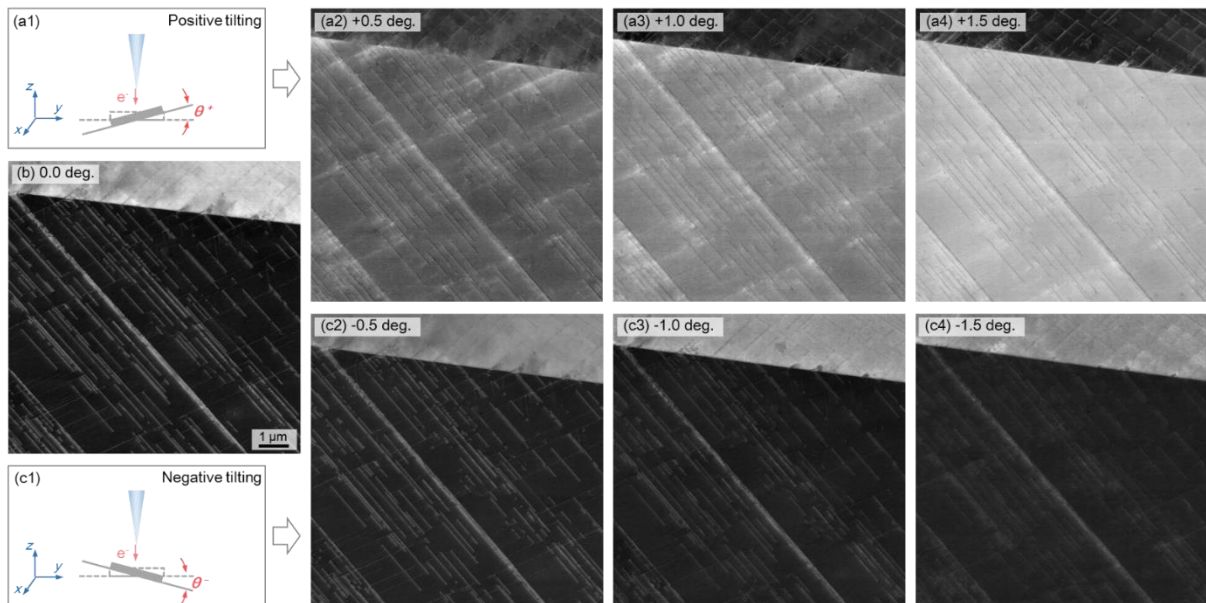
Figure 4.11: Clarification of systematic error during ECCI analysis. (a1)-(a4) ECCI micrographs during positive stage tilting; (b) ECCI micrograph of the selected area of interest without tilting; (c1)-(c4) ECCI micrographs during negative stage tilting.
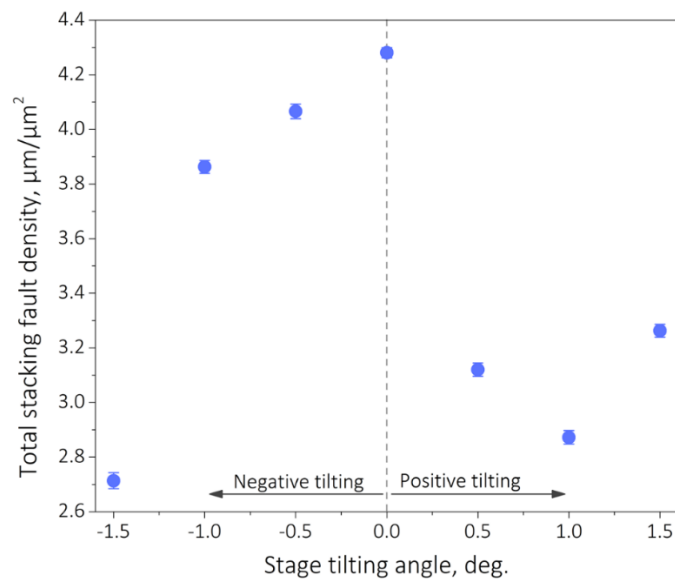
Figure 4.12: Stacking fault density change due to the variation in electron channeling condition.

For (2), we will combine the statistical assessment of stacking fault density change at the length-scale of grain size (**Figure 4.13**) and the representative local stacking fault activity (**Figure 4.14**) so as to ensure the reliability of the results.

For (3), since the present alloy consists of purely substutional elements and tensile testing results in **Figure 4.2** confirm the absence of Portevin-Le Chatelier band [148] or yield-dropping [149], it is therefore suggestive that the effect of interstitial atoms on the corresponding mechanical response is negligible.

Figure 4.13 reveals the global statistical assessment of stacking fault density change upon one loading-unloading cycle. Here, stacking faults were introduced into the specimen by applying a ~2.0 % pre-strain (corresponding engineering stress is ~577 MPa), then the surface steps were removed by metallographic polishing to achieve ECCI characterization. The maximum stress level reached in the loading-unloading experiment was controlled as 463.7 MPa, being well below the yielding point in a sense to avoid macroscopic yielding. We note that in the present statistical analysis, we determine the stacking fault density (ρ_{sf}), as the length of the plane traces per unit observational area ($A_{obv.}$):

$$\rho_{sf} = \sum length\ of\ the\ stacking\ fault\ traces/A_{obv.} \qquad (4.21)$$

At the undeformed state (**Figure 4.13 (a)**), the total ρ_{sf} achieves 3.77 $\mu m/\mu m^2$ (due to pre-strain), which then demonstrates a monotonic increasing trend with respect to elevating stress level, reaching up to 4.31 $\mu m/\mu m^2$ at 463.7 MPa applied stress (**Figure 4.13 (b)**). During the unloading portion of the experiment, the total ρ_{sf} reveals an almost invariant characteristic regardless of the removal of the external load to various extents (**Figure 4.13 (d)**). The corresponding ρ_{sf} at the fully unloaded state (**Figure 4.13 (c)**) maintains 4.29 $\mu m/\mu m^2$. These results suggest that in compatible with the assertion (2) proposed earlier, the stacking fault extension in the present alloy does reveal an irreversible nature from a global perspective, supporting the characteristic of a negative γ_{iSFE}. To more comprehensively assess the stacking fault activity, we next focus on the local behavior of two stacking fault ribbons during the foregoing loading-unloading cycle.

It is recognized from crystallographic calculations (details see **Table 4.5**) that the two stacking fault ribbons (marked with yellow and cyan arrows in **Figure 4.14 (a)**) investigated here both belong to the $(\overline{1}\overline{1}1)$ faulting plane (**Figure 4.14 (e)**), with a maximum Schmid factor (m) of 0.417 for the

corresponding glissile partials. At the undeformed state, the length of their traces respective achieve 391.3 (yellow, SF1) and 122.3 nm (cyan, SF2).
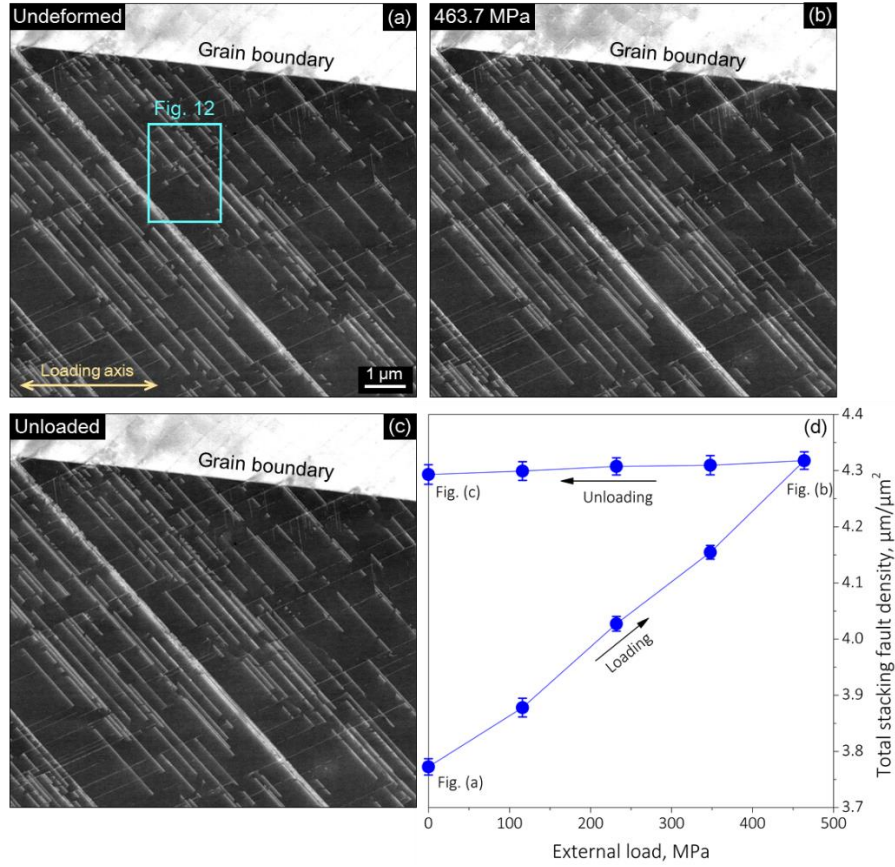
Figure 4.13: Statistical assessment of stacking fault density change during one elastic loading-unloading cycle. (a)-(c) in-situ ECCI micrographs acquired at deformed, maximum stress, and unloaded states (the same scale bar is applied); (d) the corresponding stacking fault density change.

Table 4.5: Schmid factor calculation results for the in-situ ECCI characterization

Faulting plane	Slip direction of glissile partials	m
	$[11\bar{2}]$	0.247
(111)	$[\bar{2}11]$	0.093
	$[1\bar{2}1]$	**0.340**
	$[211]$	0.046
$(\bar{1}11)$	$[12\bar{1}]$	0.057
	$[1\bar{1}2]$	**0.104**
	$[21\bar{1}]$	0.168
$(1\bar{1}1)$	$[121]$	0.057
	$[\bar{1}12]$	**0.225**
	$[2\bar{1}1]$	**0.417 (max)**
$(\bar{1}\bar{1}1)$	$[\bar{1}21]$	0.138
	$[112]$	0.279

As the applied stress level increases to 238.1 MPa, SF1 undergoes a noticeable extension in its trace length, reaching 231.8 nm (**Figure 4.14 (b)**). Such a monotonic increasing trend keeps on evolving as the applied stress elevates (**Figure 4.14 (b)-(d)**), and its eventual length achieves 1845.3 nm towards the end of the loading half-cycle (**Figure 4.14 (d)** and **(f)**), which is approximately 5 times the length of the undeformed state. SF2 also witness a similarly monotonic increase in its length (**Figure 4.14 (a)-(d) and (f)**), exhibiting 1131.3 nm at 463.7 MPa applied stress.

When the external load is gradually removed (**Figure 4.14 (g)-(j)**), both SF1 and SF2 preserve their lengths regardless of the deceasing stress level, and no discernable shrinkage within the faulted region is detected, again validating the irreversible extension hypothesis. It should be noted that the present results are of distinctive contrast when compared with a most recent report by Habib et al. [150] in an Fe-Cr-N steel with a widely-documented [151,152] positive γ_{iSFE}, in which clear reversible extension of the stacking faults was revealed by in-situ ECCI characterization. Thus far, the global statistical assessment along with the local stacking fault activity investigation compatibly verifies the foregoing assertion (2) drawn from the physical foundations of negative γ_{iSFE}.
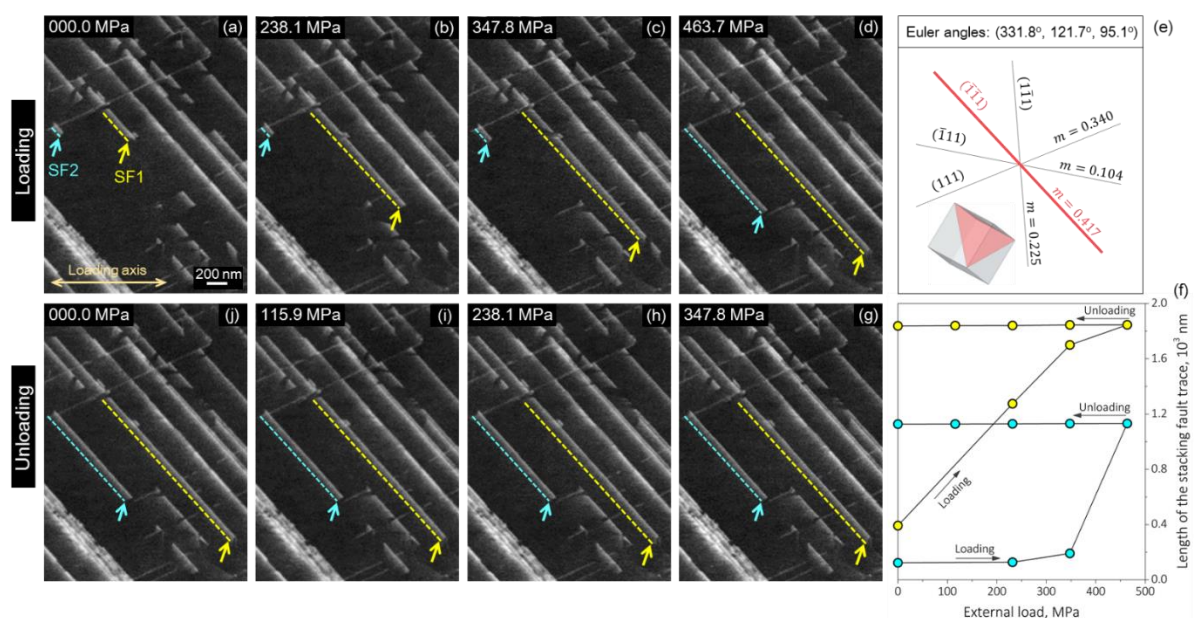
Figure 4.14: In-situ ECCI analysis of local stacking fault activity. (a)-(d) elastic loading; (g)-(j) unloading; (e) faulting plane trace and the corresponding Schmid factor for the selected region (calculation details are referred to **Table 4.5**); (f) stacking fault length change during one loading-unloading cycle. The same scale bar is applied to (a)-(d) and (g)-(j).

Section 4.2.2: Strain Hardening Micro-Mechanisms

As typical planar defects in crystalline solids, stacking faults have been documented to render substantial strengthening effect particularly in light of their interaction with glissile perfect dislocations. Exemplary experimental investigations of Cu-Al dilute alloys [153] and CoCrNiFeNb concentrated alloys [154], as well as molecular dynamics (MD) simulation [155], all verify that the presence of stacking faults can significantly impede the perfect dislocations from crossing the faulting plane, which in turn leading to stress elevation. In the foregoing regards, physical analogy of stacking faults are largely taken as grain or twin boundaries, in which the spacing between them is ascribed to the mean free-path for glissile perfect dislocations [156], and as such, the classical Hall-Petch-like concept is often applied to elucidate the strain hardening contribution [153,157–159]. Contradictorily, both in-situ and post-mortem ECCI characterizations confirm the negligible content of perfect dislocations in the present $Co_{60}Cr_{25}Ni_{10}W_5$ CCA (**Figure 4.3** and **Figure 4.14**), leading to a more detailed consideration of the underlying strain hardening micro-mechanisms. By closely examining the deformation substructure by ECCI, we propose the following two mechanistic origins that enable strain hardening.

(1) the intersection between unparalleled stacking faults which leads to the formation of sessile dislocations;

(2) the elastic repulsion between parallel stacking faults to be the two mechanistic origins that enable strain hardening.

Figure 4.15 (a) and **(b)** present the stacking fault structures at local strain levels of ~14.7 % and ~18.9 %. At these deformation levels, it is revealed by ECCI micrographs that stacking faults belong to unparalleled {111} faulting planes are nucleated (marked as trace 1 and 2), and exhibit the trend to intersect with one another. Evident node-like features can be clearly observed along the intersected regions, which are characterized by the shattered stacking fault ribbons (marked with pink arrows in **Figure 4.15 (a)**). This kind of node structures, if consider the unparalleled geometry of the activated faulting system, can be reasonably ascribed to the reaction amongst the glissile partials. Following the Thompson tetrahedron's convention [90], we phenomenologically sketch one such possibility in **Figure 4.15 (c)**. Owing to the negative γ_{iSFE} in the present $Co_{60}Cr_{25}Ni_{10}W_5$ CCA, perfect dislocations CB and DB dissociate into glissile Shockley partials following plastic incipience respectively via: $CB \rightarrow \delta C + B\delta$ and $DB \rightarrow D\gamma + \gamma B$ on the corresponding faulting plane $\overline{d}$ and c. As the stacking faults

extend due to the increase of applied stress, reaction between partials γB and $B\delta$ takes place, leading to the formation of a stair-rod sessile partial $\gamma\delta$, jamming along the intersection between faulting plane $\bar{d}$ and c. Since the Burgers vector of edge dislocation $\gamma\delta$ yields $a/6\,[110]$, whose glide plane is neither $\bar{d}$ or c, a strong Lomer-Cottrell locking effect [160] is therefore expected to occur at the intersection ΛK, effectively contributing to strain hardening and simultaneously giving rise to the node-like structures associated with shattered faults seen in **Figure 4.15 (a)** as well as the localized pinning spots in **Figure 4.15 (b)**.
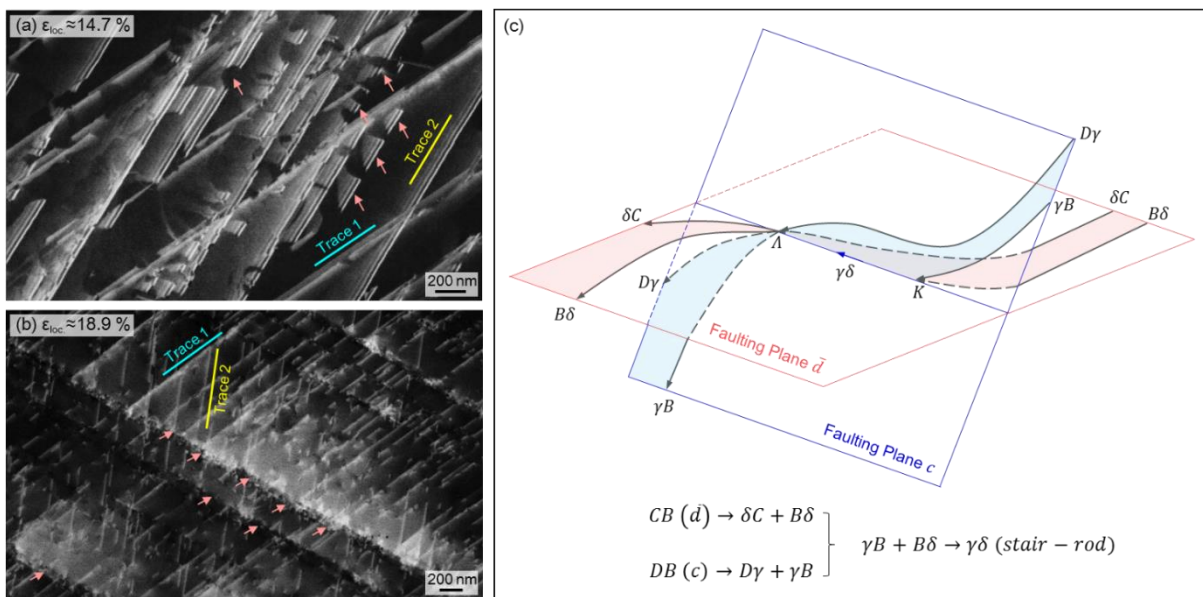
Figure 4.15: ECCI micrographs for representative unparalleled stacking faults. (a) shattered stacking faults (local stain level ~14.7 %); (b) local pinning spots at the junction between stacking faults (local strain level ~18.9 %); (c) schematic of the dislocation reaction associated with the intersected stacking fault ribbons.

We note that although the foregoing analysis considers a Lomer-Cottrell locking mechanism, which from the standpoint of Frank's energy criterion [90], enables the most significant energy dissipation, other similar micro-event, especially Hirth locking has also been proved to possess exceptional strain hardenability according to MD simulation [116], its energy dissipation rate, however, is comparatively less pronounced. In addition, while jogs formation from the reaction between partially associated unparalleled stacking faults may also contribute to strain hardening [161,162], the negative γ_{iSFE} and thereby the irreversible formation of the stacking faults (**Figure 4.14**) in the present CCA would significantly retard the association procedure, rendering this mechanism less probably to occur.

However, more quantitative elucidation of the corresponding energy landscape deems further simulation effort.

Section 4.2.3: Considerations of Alloy Design Strategies

Comparison between the present $Co_{60}Cr_{25}Ni_{10}W_5$ CCA and the latest metastable FeMnCoCr HEAs evidently reveals the improved strength-ductility synergy due to the operation of extensive deformation faulting response (**Figure 4.2 (a)** and **Figure 4.7 (e)**). Although the strain-induced FCC-HCP martensitic transformation within the latter also promotes strain hardenability, its mechanistic limitation largely associates with the blocky HCP-martensite because:

(1) limited slip system and plastic anisotropy of the HCP-structure retards effective plastic strain accommodation [91,163];

(2) strain incompatibility occurring at the junction between HCP-martensite and FCC grain boundaries immediately facilitates micro-cracking [37].

A micro-mechanical revelation of this dilemma can be understood from the fact that blocky HCP-phase formation is a procedure that renders almost complete exhaustion of "local ductility" [164], sacrificing the capability of delocalizing any stress concentrator onwards. Mechanistically, it can be therefore deduced that if individual HCP-band can be ideally refined to infinitely thin and remains thermodynamically stable, the foregoing "local ductility" exhaustion dilemma can be potentially mitigated. Intriguingly, as shown earlier, such an idealized scenario is feasibly achieved by the present deformation faulting response (see *structural consideration* in Section 4.2.1), and the corresponding γ_{iSFE} ensures the thermodynamic stability of the stacking faults (see *thermodynamic consideration* in Section 4.2.1).

In the theoretical framework of microstructural metastability engineering, we note that complete tunable design of faulting CCAs/HEAs may not only rely on negative γ_{iSFE}, but also requires mechanical stability of the stacking faults. In this regard, it is therefore suggestive that multi-layered GSFE computation [144] is indispensable in elucidating the full deformation energy landscape, especially considering the correlation between individual faulting unit and the mechanical energy barrier for HCP-phase as well as mechanical twin nucleation. As such, we assert that in addition to the profuse focus on strain-induced martensitic transformation or mechanical twinning, deformation faulting, or ideally

speaking, faulting-mediated plasticity can also become a mechanistically-driven design strategy for advancing metastable CCAs/HEAs development.

Section 4.4: Conclusions

With the aids of in-situ synchrotron X-ray diffractometry and in-situ ECCI technique, this chapter has systematically explored the deformation micro-mechanisms of a metastable $Co_{60}Cr_{25}Ni_{10}W_5$ CCA with primary focus on the role of stacking faults, and major findings are concluded in the following respects:

(1) In contrast to perfect dislocation glide or strain-induced FCC-HCP martensitic transformation, it is recognized that the nucleation and thereby multiplication of stacking faults is acting as the major plasticity carrier in the present CCA. Results of in-situ synchrotron X-ray diffraction experiment validate a direct correlation between the increase of stacking fault probability and the elevation of strain hardening exponent, indicating that the deformation faulting mechanism by itself enables macroscopic strain hardening;

(2) By quantitatively exploring the relative phase stability through thermodynamic modelling, we show that this sort of less-explored deformation faulting response is mechanistically related to a negative intrinsic stacking fault energy. Its physical foundations are theoretically assessed in the aspects of thermodynamics, structure, and mechanics, supported by in-situ ECCI analyses which verifies the irreversible extension of stacking faults during elastic loading-unloading cycle;

(3) Unlike the classical Hall-Petch-type concept which ascribes strain hardening to stacking fault-glissile perfect dislocation interaction, we reveal that in the absence of perfect dislocation, two micro-events are essential in rendering strain hardenability, namely, the nucleation of sessile dislocation via intersected unparalleled stacking faults and the elastic repulsion between parallel stacking faults;

(4) Through the comparison between the present CCA and the metastable FeMnCoCr-type HEAs where strain-induced FCC-HCP martensitic transformation is predominant, it is suggestive that the present deformation faulting micro-mechanism can effectively alleviate the drastic exhaustion of local ductility in the latter case, demonstrating the potential in avoiding early-stage damage nucleation. We also note that future simulation effort aiming at the elucidation of the entire deformation energy landscape would expedite the mechanistically-driven metastable CCAs/HEAs design, magnifying the benefits of deformation faulting response.

Chapter 5: Discussion and Future Directions

The previous **Chapter 3** and **Chapter 4** respectively discuss the potential microstructural design strategies on the basis of phase transformations and plastic deformation micro-mechanisms. The contents presented in this chapter are further considerations of the intriguing results revealed in the previous two chapters that may be worth exploring for future studies. Two such topics are proposed: first, plastically deformable strain-induced HCP-martensite; and second, local intrinsic stacking fault energy modulated by chemical short range ordering.

Like all other HCP-metals, crystal structure of the strain-induced HCP-martensite is intrinsically more anisotropic especially compared with FCC-metals. As implied by the von Mises criterion [90], a stable plastic flow generally requires the activation of five independent slip systems. However, the two slip modes in HCP-martensite (basal-$\langle \mathbf{a} \rangle$ and prismatic-$\langle \mathbf{a} \rangle$ slip), which presumably exhibit the lowest critical resolved shear stress (CRSS) magnitudes can only enable four independent slip systems. Thus, additional deformation mechanisms shall be activated, especially, to accommodate the plastic strain along the $\langle \mathbf{c} \rangle$-direction. The results shown in **Section 3.2** underpin the feasibility to activate displacive HCP-FCC phase transformation in the HCP-martensite by partial dislocation glide on the basal plane. This kind of mechanism, as revealed earlier, can exhibit the potential to promote plastic strain accommodation capability of the HCP-martensite. In light of this, it is also suggested that the following two potential mechanisms may also be considered for future work:

(1) Activating non-basal slip. This kind of concept is considered based on the STEM observation shown in **Figure 3.16**. By characterizing the structure of the strain-induced HCP-martensite at atomic length scale, it is revealed that dislocations with mixed $\langle \mathbf{a} \rangle$ and $\langle \mathbf{c} \rangle$ components can also be activated by plastic straining. It can be therefore anticipated that if $\langle \mathbf{c} + \mathbf{a} \rangle$ dislocation slip mode can also be easily activated in the strain-induced HCP-martensite, the resultant plastic strain accommodation along the $\langle \mathbf{c} \rangle$-axis can be effectively improved. In fact, decades of effort in promoting plastic deformability of Mg alloys, have highlighted the importance of the c/a ratio of the HCP-lattice in affecting the activity of $\langle \mathbf{c} + \mathbf{a} \rangle$ dislocations [91]. The critical role of c/a ratio lies in its direct link with the lattice spacing. The hard-sphere model documented in textbooks reveals an ideal c/a ratio of 1.633, above which, the

lattice spacing of the basal plane increases, and *vice versa* [165]. Consequently, the CRSS that dislocations need to overcome is structurally related with the c/a ratio, as implied by the Peierls model [90]. In this pure Peierls-type framework, the most effective way to activate more $\langle \mathbf{c} + \mathbf{a} \rangle$ dislocations in strain-induced HCP-martensite, is to reduce the atomic packing density of non-basal planes of the HCP-lattice by adjusting alloying element content. It should be noted that, the choice of optimal alloying element, also requires more dedicated considerations because of the potential influence on strain-induced HCP-martensite formation potency.

(2) Activating mechanical twinning. In addition to $\langle \mathbf{c} + \mathbf{a} \rangle$ dislocation slip, an alternative way to accommodate non-basal plastic strain is to introduce mechanical twinning in strain-induced HCP-martensite. Common tension twinning modes documented in the literature in HCP-metals, for example, $\{10\bar{1}2\}\langle\bar{1}011\rangle$ and $\{11\bar{2}1\}\langle11\bar{2}6\rangle$ modes may both accommodate shear strain along the $\langle \mathbf{c} \rangle$ axis[91]. In this sense, two strategies may be considered to increase the twinning potency of strain-induced HCP-martensite. Intrinsically, similar to the concept to promote $\langle \mathbf{c} + \mathbf{a} \rangle$ dislocation slip, compositional adjustment is primarily suggested. Extrinsically, when the composition is fixed, crystallographic texture optimization of the parent FCC-phase is also recommended. This is because, the formation of HCP-martensite, according to **Chapter 1** and **Chapter 3**, is a displacive phase transformation, but highly yields the Schmid's law (i.e. follow the maximum resolved shear stress direction). Thus, if the parent FCC-phase texture can be adjusted in a way that the specific HCP-martensite variant whose $\langle \mathbf{c} \rangle$ axis is parallel to the loading axis is preferentially formed, the following twinning potency for either $\{10\bar{1}2\}\langle\bar{1}011\rangle$ or $\{11\bar{2}1\}\langle11\bar{2}6\rangle$ mode can be promoted. This is because, when the loading axis is parallel with the $\langle \mathbf{c} \rangle$ axis, the resolved shear stress on basal and prismatic planes are minimized [87]. In such a way that a multi-stage metastability engineering concept for strain-induced HCP-martensite may be realized.

Considering the twinning mode in HCP-metals, one additional factor worth being considered is the shear-shuffle competition in the $\{10\bar{1}2\}\langle\bar{1}011\rangle$ mode. Unlike other extension twinning mode in HCP-metals, because of the atomic packing, the $\{10\bar{1}2\}\langle\bar{1}011\rangle$ twin, theoretically can be achieved either by shear (see **Figure 5.1 (a)**) or basal-prismatic atomic shuffle transformation [166–168] (see **Figure 5.1 (b)**). Earlier molecular dynamics (MD) and density functional theory (DFT) simulation highlight

the more predominant role of atomic shuffle in the $\{10\bar{1}2\}\langle\bar{1}011\rangle$ twinning mode for Mg [166,169]. This kind of argumentation was recently supported by *in-situ* HRTEM investigations on Mg, and Re [170,171]. However, detailed atomistic processes regarding potential $\{10\bar{1}2\}\langle\bar{1}011\rangle$ twinning mode in strain-induced HCP-martensite would still require dedicated effort. If shuffle, rather than shear, is confirmed to be the major mechanism, in a macroscopic viewpoint, the plastic strain accommodation of the $\{10\bar{1}2\}\langle\bar{1}011\rangle$ twinning mode in strain-induced HCP-martensite is also worth exploring.
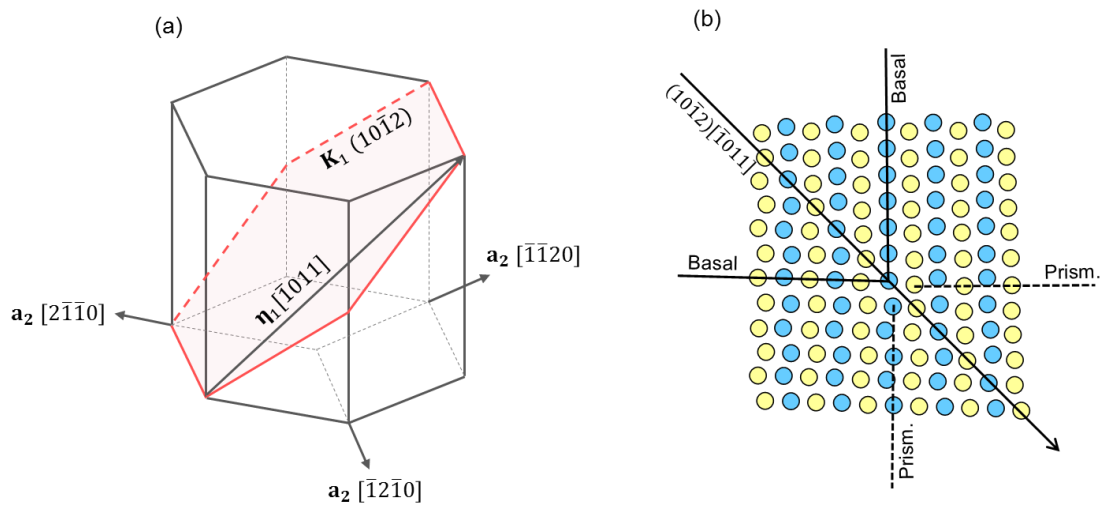
Figure 5.1: $\{10\bar{1}2\}\langle\bar{1}011\rangle$ twinning mode in HCP-metals. (a) Crystallographic elements; (b) atomic details close to twin boundary.

The second future direction suggested for future study is the consideration of local intrinsic stacking fault modulated by chemical short range ordering, which is motivated by the investigations in **Chapter 4**. In **Figure 4.13** it is seen that given the uniaxial tensile loading with moderate plastic strain level, the stacking fault distribution within the grain interior is highly heterogeneous. Unlike typical slip traces that would populate homogenously within any given grains at a similar plastic deformation level, the stacking fault formation tends to prefer a certain spatial pathway. While there may be the effect of local stress state deviation, however, the other possibility should not be ignored, which is the spatial variation of alloying element distribution. In the latter situation, it is anticipated that the local chemical environment may exhibit an evident deviation from the nominal composition of the alloy system (i.e. local chemical ordering), which can alter the intrinsic stacking fault energy and consequently affect the mechanical faulting event. This kind of phenomenon is worth considering in both theoretical and practical aspects for future work:

(1) Theoretically, the GSFE evaluation of the deformation landscape in FCC-alloys will need to take local chemical effects into account. Recent DFT and MD studies have both confirmed that, the variation of local chemical composition can cause a salient difference in the resultant intrinsic stacking fault energy [172,173]. In fact, recent TEM characterization research also underpinned that the partial dislocation separation width in some concentrated alloy systems can demonstrate noticeable spatial variation [141]. These results imply that intrinsic stacking fault energy estimation based on **Eq. (4.5)** may need further modification to take into account the contribution of local chemical ordering effect. In addition, for alloy system where the intrinsic stacking fault energy is negative, more dedicated effort is also necessary, because the role of the lattice friction force is not trivial and may further complicate the intrinsic stacking fault energy evaluation.
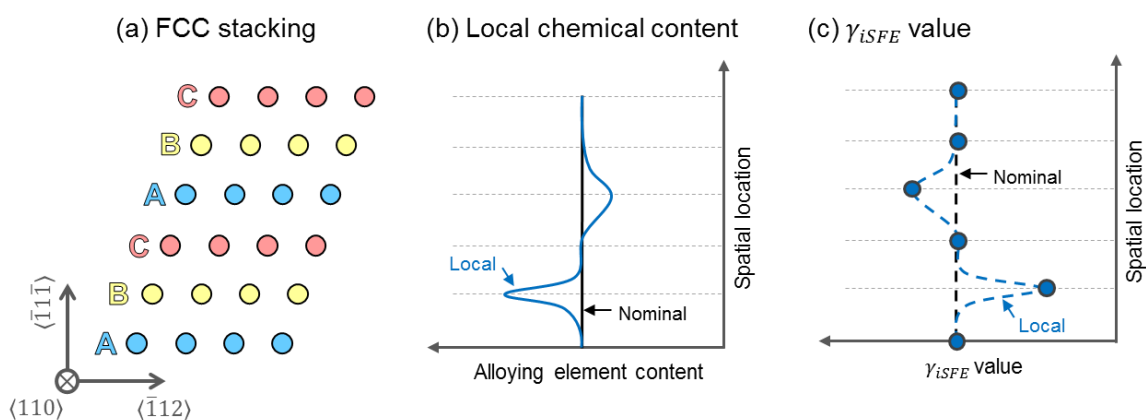
Figure 5.2: Local chemical effect on intrinsic stacking fault energy. (a) Schematic of FCC stacking sequence; (b) deviation of local chemical content from nominal composition; (c) resultant effect on local intrinsic stacking fault energy.

(2) Practically, the local chemical ordering effect on mechanical faulting potency may also open up a space for microstructural design via local phase transformations. Such a concept will be most feasible when external heat is applied to alloys that can exhibit mechanical faulting. It is anticipated that the mechanical faults, as planar defects, can act as preferential segregation sites for alloy elements during relatively low temperature annealing. If the chemical composition of the alloy can be meticulously designed, this kind of strategy will enable the development of thin but layer-like precipitation phases, nucleating within the grain interior. Although dedicated effort is also needed to optimize both the

composition and the thermomechanical processing condition, recent STEM investigation of crept Ni-based superalloys does confirm the stacking-fault driven χ-phase (D0$_{19}$ structure) nucleation [174].

Chapter 6: Conclusions

The major aim of the thesis is to assess potential microstructural design solutions to improve the mechanical performances of metastable concentrated FCC-alloys that exhibit strain-induced martensitic transformation. With integrated *in-situ* experimentation and theoretical calculations, two general concepts are explored in details, respectively aiming at phase transformations and plasticity micro-mechanisms. The following conclusions are drawn for the present thesis:

(1) *In-situ* SEM/EBSD/µ-DIC investigations of a metastable $Fe_{45}Mn_{35}Co_{10}Cr_{10}$ confirms that under plastic loading, the strain-induced HCP-martensite can further undergo an HCP-FCC transformation. The final FCC-phase, provided its extensive defect density, can still accommodate plastic strain. Coupled crystallographic calculation and STEM characterization indicate that the random partial emission processes in the strain-induced HCP-martensite is plausibly responsible for this peculiar phase transformation pathway. The universality of this kind of FCC-HCP-FCC phase transformation is further validated a metastable ternary $(Fe_{60}Mn_{40})_{85}Co_{15}$ alloy.

(2) By considering the thermal stability of the strain-induced HCP-martensite, bake reversion hardening strategy is also assessed. The shear-assisted HCP-FCC reverse transformation is proved to activate latent strain hardenability. The coupled EBSD/ECCI investigations confirm the underlying mechanisms are due to the more effective stress delocalization processes and the enhanced phase boundary– glissile dislocation interaction, which jointly brought about by the nucleation of secondary HCP-martensite variant. It is recommended that this sort of bake-reversion hardening mechanism that achieves in the same time scale and temperature range as conventional bake-hardening treatment, can be further generalized as a low-temperature annealing method to improve the mechanical performances of other Fe-Mn-type metastable alloys.

(3) To reduce the potency of block HCP-martensite formation, a mechanical faulting approach is also considered. Through coupled *in-situ* synchrotron X-ray diffraction study and *in-situ* ECCI analyses, the strain hardening contribution from mechanical-induced stacking faults are clarified. It is also recognized from thermodynamic modeling that the observed extensive stacking fault formation is largely associated

with a negative intrinsic stacking fault energy. The theoretical revelations of the negative intrinsic stacking fault energy are introduced considering thermodynamics, structure, and mechanics. Systematic *in-situ* ECCI experiment is also conducted and the results are consistent with the proposed hypotheses. Future alloy design activates are suggested to maximize the strain hardening contribution from mechanical faulting in Co-rich metastable alloys by either fine tuning the Co-content or considering interstitial alloying element addition.

(4) In a conceptual viewpoint, the present thesis also propose to envisage a general methodology for alloy design. In contrast to the existing approaches that are based on "known phenomena", it is suggested that new design guidelines can also be obtained from *in-situ* experiments. Under this framework, two general future directions are also proposed and their feasibilities are discussed. In light of plastic strain-induced phase transformation, it is suggested that future studies could focus on deformable strain-induced HCP-martensite by activating $\langle \mathbf{c} + \mathbf{a} \rangle$ dislocation slip or mechanical twinning modes. In that sense, a multi-stage metastability engineering concept can be proposed for strain-induced HCP-martensite. For plasticity, micro-mechanism, future explorations of local chemical ordering effect on intrinsic stacking fault energy is suggested. In a practical viewpoint, this direction may also enable the design of local phase transformation aided by mechanical faults, which might open up a new path to achieve fine-scale precipitates.

References

[1]   W. Ostwald, On chemical energy, J. Am. Chem. Soc. 15 (1893) 421–430. doi:10.1038/scientificamerican06011920-563asupp.

[2]   D. Turnbull, Metastable structures in metallurgy, Metall. Trans. B. 12 (1981) 217–230. doi:10.1007/BF02654454.

[3]   R.W. Cahn, The Coming of Materials Science, (2001) 586. doi:http://dx.doi.org/10.1007/s00405-013-2626-6.

[4]   R.O. Ritchie, The conflicts between strength and toughness, Nat. Mater. 10 (2011) 817–822. doi:10.1038/nmat3115.

[5]   M. Cohen, G.B. Olson, C.P. Clapp, Proceedings of the International Conference on Martensitic Transformation, (1979).

[6]   J.W. Christian, G.B. Olson, M. Cohen, Classification of displacive transformations: What is a martensitic tansformation, J. Phys. IV. 5 (1995) 3–10. doi:10.1051/jp4.

[7]   L. Kaufman, M. Cohen, Thermodynamics and kinetics of martensitic transformations, Prog. Met. Phys. 7 (1958) 165–246. doi:10.1016/0021-9681(79)90124-3.

[8]   H.K.D.H. Bhadeshia, Thermodynamic extrapolation and martensite-start temperature of substitutionally alloyed steels, Met. Sci. 15 (1981) 178–180. doi:10.1179/030634581790426697.

[9]   K. Ishida, Effect of alloying elements on the critical driving force of martensitic transformation in iron alloys, Scr. Metall. 11 (1977) 237–242. doi:10.1016/0036-9748(77)90061-8.

[10] T.Y. Hsu, H.B. Chang, On calculation of Ms and driving force for martensitic transformation in Fe-C, Acta Metall. 32 (1984) 343–348. doi:10.1016/0001-6160(84)90107-X.

[11] G.B. Olson, A.L. Roitburd, In Martensite, ASM Int. (1992) 149–152.

[12] G.B. Olson, M. Cohen, A perspective on martensitic nucleation, Annu. Rev. Mater. Sci. 11 (1981) 1–30.

[13] E.C. Bain, N.Y. Dunkirk, The Nature of Martensite, Trans. AIME. 70 (1924) 25–47.

[14] M.S. Wechsler, On the theory of martensitic transformations. The generalized lattice invariant shear and the degeneracy of solutions for the cubic to tetragonal transformation, Acta Metall. 7 (1959) 793–802. doi:10.1016/0001-6160(59)90095-1.

[15] H.K.D.H. Bhadeshia, Geometry of crystals, polycrystals, and phase transformations, 2017. doi:10.1201/9781315114910.

[16] J.S. Bowles, J.K. Mackenzie, The crystallography of martensite transformations I, Acta Metall. 2 (1954) 129–137. doi:10.1016/0001-6160(54)90102-9.

[17] J.K. Mackenzie, J.S. Bowles, The crystallography of martensite transformations II, Acta Metall. 2 (1954) 138–147. doi:10.1016/0001-6160(54)90103-0.

[18] G.B. Olson, M. Cohen, A mechanism for the strain-induced nucleation of martensitic transformations, J. Less-Common Met. 28 (1972) 107–118. doi:10.1016/0022-5088(72)90173-7.

[19] I. Müller, H. Xu, On the pseudo-elastic hysteresis, Acta Metall. Mater. 39 (1991) 263–271.

[20] I. Tamura, T. Maki, H. Hato, Morphology of strain-induced martensite and the transformation-induced plasticity in Fe-Ni and Fe-Cr-Ni alloys, Trans. Iron Steel Inst. Jap. 10 (1970) 163–172.

[21] J.R. Patel, M. Cohen, Criterion for the action of applied stress in the martensitic transformation, Acta Metall. 1 (1953) 531–538. doi:10.1016/0001-6160(53)90083-2.

[22] P. Chowdhury, D. Canadinc, H. Sehitoglu, On deformation behavior of Fe-Mn based structural

alloys, Mater. Sci. Eng. R Reports. 122 (2017) 1–28. doi:10.1016/j.mser.2017.09.002.

[23] H. Fujita, T. Katayama, In-situ observation of strain-induced FCC-HCP-BCT and FCC-BCT Martensitic Transformations in Fe-Cr-Ni alloys, Mater. Trans. 33 (1992) 243–252.

[24] J. Liu, C. Chen, Q. Feng, X. Fang, H. Wang, F. Liu, J. Lu, D. Raabe, Dislocation activities at the martensite phase transformation interface in metastable austenitic stainless steel: An in-situ TEM study, Mater. Sci. Eng. A. 703 (2017) 236–243. doi:10.1016/j.msea.2017.06.107.

[25] X.S. Yang, S. Sun, H.H. Ruan, S.Q. Shi, T.Y. Zhang, Shear and shuffling accomplishing polymorphic fcc γ → hcp ε → bct α martensitic phase transformation, Acta Mater. 136 (2017) 347–354. doi:10.1016/j.actamat.2017.07.016.

[26] X.S. Yang, S. Sun, T.Y. Zhang, The mechanism of bcc α′ nucleation in single hcp ε laths in the fcc γ → hcp ε → bcc α′ martensitic phase transformation, Acta Mater. 95 (2015) 264–273. doi:10.1016/j.actamat.2015.05.034.

[27] J.W. Christian, V. Vitek, Dislocations and stacking faults - Christian, V fek.pdf, Reports Prog. Phys. 33 (1970) 308–400.

[28] G.B. Olson, M. Cohen, A General Mechanism of Martensitic Nucleation, Metall. Trans. A. 7 (1976) 1897–1904. doi:10.1007/BF02659822.

[29] G.B. Olson, M. Cohen, Kinetics of Strain Induced Martensitic Nucleation, Metall. Trans. A. 6 A (1975) 791–795. doi:10.1007/BF02672301.

[30] D. Pandey, S. Lele, On the Study of the FCC-HCP martensitic transformation using a diffraction approach: I. FCC-to-HCP transformation, Acta Metall. 34 (1986) 405–413. doi:10.1016/B978-0-12-519850-9.50010-7.

[31] Z.H. Guo, Y.H. Rong, S.P. Chen, T.Y. Hsu, J.M. Hong, X.N. Zhao, Reverse Transformation Characteristics of Thermally Induced HCP Martensite in an Fe-Mn-Si Based alloy, Mater. Trans. 40 (1999) 193–198.

[32] B. Jiang, T. Tadaki, H. Mori, T.Y. Hsu, In-situ TEM observation of γ→ε martensitic transformation during tensile straining in an Fe-Mn-Si shape memory alloy, Mater. Trans. JIM. 38 (1997) 1072–1077. doi:10.2320/matertrans1989.38.1072.

[33] Z. Li, K.G. Pradeep, Y. Deng, D. Raabe, C.C. Tasan, Metastable high-entropy dual-phase alloys overcome the strength-ductility trade-off, Nature. 534 (2016) 227–230. doi:10.1038/nature17981.

[34] S. Harjo, N. Tsuchida, J. Abe, W. Gong, Martensite phase stress and the strengthening mechanism in TRIP steel by neutron diffraction, Sci. Rep. 7 (2017) 2–4. doi:10.1038/s41598-017-15252-5.

[35] M. Koyama, T. Sawaguchi, K. Tsuzaki, Premature fracture mechanism in an Fe-Mn-C austenitic steel, Metall. Mater. Trans. A Phys. Metall. Mater. Sci. 43 (2012) 4063–4074. doi:10.1007/s11661-012-1220-7.

[36] S.M. Lee, S.J. Lee, S. Lee, J.H. Nam, Y.K. Lee, Tensile properties and deformation mode of Si-added Fe-18Mn-0.6C steels, Acta Mater. 144 (2018) 738–747. doi:10.1016/j.actamat.2017.11.023.

[37] S. Wei, J. Kim, C.C. Tasan, Boundary micro-cracking in metastable Fe 45 Mn 35 Co 10 Cr 10 high-entropy alloys, Acta Mater. 168 (2019) 76–86. doi:10.1016/j.actamat.2019.01.036.

[38] N. Stanford, D.P. Dunne, Effect of Si on the reversibility of stress-induced martensite in Fe-Mn-Si shape memory alloys, Acta Mater. 58 (2010) 6752–6762. doi:10.1016/j.actamat.2010.08.041.

[39] J.Y. Kang, H. Kim, K. Il Kim, C.H. Lee, H.N. Han, K.H. Oh, T.H. Lee, Effect of austenitic

texture on tensile behavior of lean duplex stainless steel with transformation induced plasticity (TRIP), Mater. Sci. Eng. A. 681 (2017) 114–120. doi:10.1016/j.msea.2016.11.001.

[40] M.M. Wang, C.C. Tasan, D. Ponge, D. Raabe, Spectral TRIP enables ductile 1.1 GPa martensite, Acta Mater. 111 (2016) 262–272. doi:10.1016/j.actamat.2016.03.070.

[41] D. Raabe, D. Ponge, O. Dmitrieva, B. Sander, Nanoprecipitate-hardened 1.5 GPa steels with unexpected high ductility, Scr. Mater. 60 (2009) 1141–1144. doi:10.1016/j.scriptamat.2009.02.062.

[42] W. Pantleon, Resolving the geometrically necessary dislocation content by conventional electron backscattering diffraction, Scr. Mater. 58 (2008) 994–997. doi:10.1016/j.scriptamat.2008.01.050.

[43] S. Wei, S.J. Kim, J.Y. Kang, Y. Zhang, Y. Zhang, T. Furuhara, E.S. Park, C.C. Tasan, Natural-mixing guided design of refractory high-entropy alloys with as-cast tensile ductility, Nat. Mater. (2020). doi:10.1038/s41563-020-0750-4.

[44] S. Wei, M. Jiang, C.C. Tasan, Interstitial-Free Bake Hardening Realized by Epsilon Martensite Reverse Transformation, Metall. Mater. Trans. A Phys. Metall. Mater. Sci. 50 (2019) 3985–3991. doi:10.1007/s11661-019-05344-4.

[45] L. Dieterle, B. Butz, E. Müller, Optimized Ar +-ion milling procedure for TEM cross-section sample preparation, Ultramicroscopy. 111 (2011) 1636–1644. doi:10.1016/j.ultramic.2011.08.014.

[46] X. Sang, J.M. LeBeau, Revolving scanning transmission electron microscopy: Correcting sample drift distortion without prior knowledge, Ultramicroscopy. 138 (2014) 28–35. doi:10.1016/j.ultramic.2013.12.004.

[47] X. Sang, A.A. Oni, J.M. Le Beau, Atom column indexing: Atomic resolution image analysis through a matrix representation, Microsc. Microanal. (2014). doi:10.1017/S1431927614013506.

[48] M.J. Hÿch, E. Snoeck, R. Kilaas, Quantitative measurement of displacement and strain fields from HREM micrographs, Ultramicroscopy. 74 (1998) 131–146. doi:10.1016/S0304-3991(98)00035-7.

[49] D. Yan, C.C. Tasan, D. Raabe, High resolution in situ mapping of microstrain and microstructure evolution reveals damage resistance criteria in dual phase steels, Acta Mater. 96 (2015) 399–409. doi:10.1016/j.actamat.2015.05.038.

[50] S.-S. Rui, L.-S. Niu, H.-J. Shi, S. Wei, C.C. Tasan, Diffraction-based misorientation mapping: A continuum mechanics description, J. Mech. Phys. Solids. 133 (2019) 103709. doi:10.1016/j.jmps.2019.103709.

[51] S. Wei, G. Zhu, C.C. Tasan, Slip-twinning interdependent activation across phase boundaries: An in-situ investigation of a Ti-Al-V-Fe (α+β) alloy, Acta Mater. (2021). doi:10.1016/j.actamat.2020.116520.

[52] S. Wei, J. Kim, J.L. Cann, R. Gholizadeh, N. Tsuji, C.C. Tasan, Plastic strain-induced sequential martensitic transformation, Scr. Mater. 185 (2020) 36–41. doi:10.1016/j.scriptamat.2020.03.060.

[53] M.E. Gurtin, E. Fried, L. Anand, The Mechanics and Thermodynamics of Continua, 2010. doi:10.1017/cbo9780511762956.

[54] D. Dye, H.J. Stone, R.C. Reed, A two phase elastic-plastic self-consistent model for the accumulation of microstrains in Waspaloy, Acta Mater. (2001). doi:10.1016/S1359-6454(01)00003-9.

[55] A. Wanner, D.C. Dunand, Synchrotron X-ray study of bulk lattice strains in externally loaded

Cu-Mo composites, Metall. Mater. Trans. A Phys. Metall. Mater. Sci. (2000). doi:10.1007/BF02830344.

[56]   M.R. Daymond, P.J. Withers, A synchrotron radiation study of transient internal strain changes during the early stages of thermal cycling in an Al / SiCw MMC, Scr. Mater. (1996). doi:10.1016/1359-6462(96)00274-6.

[57]   B.H. Toby, R.B. Von Dreele, GSAS-II: The genesis of a modern open-source all purpose crystallography software package, J. Appl. Crystallogr. (2013). doi:10.1107/S0021889813003531.

[58]   H.-J. Bunge, Texture Analysis in Materials Science, 1982. doi:10.1016/c2013-0-11769-2.

[59]   C.M. Cepeda-Jiménez, J.M. Molina-Aldareguia, M.T. Pérez-Prado, EBSD-Assisted Slip Trace Analysis During In Situ SEM Mechanical Testing: Application to Unravel Grain Size Effects on Plasticity of Pure Mg Polycrystals, JOM. (2016). doi:10.1007/s11837-015-1521-6.

[60]   I. Müller, H. Xu, ON THE PSEUDO-ELASTIC HYSTERESIS, Acta Metall. Mater. 39 (1991) 263–271.

[61]   Z. Zhang, X. Ding, J. Sun, T. Suzuki, T. Lookman, K. Otsuka, X. Ren, Nonhysteretic Superelasticity of Shape Memory Alloys at the Nanoscale, Phys. Rev. Lett. 111 (2013) 145701. doi:10.1103/PhysRevLett.111.145701.

[62]   N. Abdolrahim, I.N. Mastorakos, H.M. Zbib, Deformation mechanisms and pseudoelastic behaviors in trilayer composite metal nanowires, Phys. Rev. B - Condens. Matter Mater. Phys. 81 (2010) 1–5. doi:10.1103/PhysRevB.81.054117.

[63]   K.H. Kwon, B.C. Suh, S. Il Baik, Y.W. Kim, J.K. Choi, N.J. Kim, Deformation behavior of duplex austenite and ε-martensite high-Mn steel, Sci. Technol. Adv. Mater. 14 (2013). doi:10.1088/1468-6996/14/1/014204.

[64]   P. Schloth, M.A. Weisser, H. Van Swygenhoven, S. Van Petegem, P. Susila, V. Subramanya Sarma, B.S. Murty, S. Lauterbach, M. Heilmaier, Two strain-hardening mechanisms in nanocrystalline austenitic steel: An in situ synchrotron X-ray diffraction study, Scr. Mater. 66 (2012) 690–693. doi:10.1016/j.scriptamat.2012.01.021.

[65]   Y. Tian, S. Lin, J.Y.P. Ko, U. Lienert, A. Borgenstam, P. Hedström, Micromechanics and microstructure evolution during in situ uniaxial tensile loading of TRIP-assisted duplex stainless steels, Mater. Sci. Eng. A. 734 (2018) 281–290. doi:10.1016/j.msea.2018.07.040.

[66]   R. Blondé, E. Jimenez-Melero, L. Zhao, J.P. Wright, E. Brück, S. van der Zwaag, N.H. van Dijk, Mechanical stability of individual austenite grains in TRIP steel studied by synchrotron X-ray diffraction during tensile loading, Mater. Sci. Eng. A. 618 (2014) 280–287. doi:10.1016/j.msea.2014.09.008.

[67]   R.G. Stringfellow, D.M. Parks, G.B. Olson, A constitutive model for transformation plasticity accompanying strain-induced martensitic transformations in metastable austenitic steels, Acta Metall. Mater. 40 (1992) 1703–1716. doi:10.1016/0956-7151(92)90114-T.

[68]   T. Park, L.G. Hector, X. Hu, F. Abu-Farha, M.R. Fellinger, H. Kim, R. Esmaeilpour, F. Pourboghrat, Crystal plasticity modeling of 3rd generation multi-phase AHSS with martensitic transformation, Int. J. Plast. 120 (2019) 1–46. doi:10.1016/j.ijplas.2019.03.010.

[69]   M. Zecevic, M. V. Upadhyay, E. Polatidis, T. Panzner, H. Van Swygenhoven, M. Knezevic, A crystallographic extension to the Olson-Cohen model for predicting strain path dependence of martensitic transformation, Acta Mater. 166 (2019) 386–401. doi:10.1016/j.actamat.2018.12.060.

[70] S. Hémery, P. Villechaise, In situ EBSD investigation of deformation processes and strain partitioning in bi-modal Ti-6Al-4V using lattice rotations, Acta Mater. 171 (2019) 261–274. doi:10.1016/j.actamat.2019.04.033.

[71] A. Fillafer, C. Krempaszky, E. Werner, On strain partitioning and micro-damage behavior of dual-phase steels, Mater. Sci. Eng. A. 614 (2014) 180–192. doi:10.1016/j.msea.2014.07.029.

[72] J.W. Christian, Tetragonal martensites in ferrous alloys-a critique, Mater. Trans. JIM. 33 (1992) 208–214.

[73] J. Liu, C. Chen, Q. Feng, X. Fang, H. Wang, F. Liu, J. Lu, D. Raabe, Dislocation activities at the martensite phase transformation interface in metastable austenitic stainless steel: An in-situ TEM study, Mater. Sci. Eng. A. 703 (2017) 236–243. doi:10.1016/j.msea.2017.06.107.

[74] X.L. Wu, X.Z. Liao, S.G. Srinivasan, F. Zhou, E.J. Lavernia, R.Z. Valiev, Y.T. Zhu, New deformation twinning mechanism generates zero macroscopic strain in nanocrystalline metals, Phys. Rev. Lett. 100 (2008) 5–8. doi:10.1103/PhysRevLett.100.095701.

[75] B.Q. Li, B. Li, Y.B. Wang, M.L. Sui, E. Ma, Twinning mechanism via synchronized activation of partial dislocations in face-centered-cubic materials, Scr. Mater. 64 (2011) 852–855. doi:10.1016/j.scriptamat.2011.01.016.

[76] R.K. Pathria, P.D. Beale, Statistical Mechanics, Third Edition, 2007.

[77] S.F. Liu, Y. Wu, H.T. Wang, W.T. Lin, Y.Y. Shang, J.B. Liu, K. An, X.J. Liu, H. Wang, Z.P. Lu, Transformation-reinforced high-entropy alloys with superior mechanical properties via tailoring stacking fault energy, J. Alloys Compd. 792 (2019) 444–455. doi:10.1016/j.jallcom.2019.04.035.

[78] J.S. Jeong, W. Woo, K.H. Oh, S.K. Kwon, Y.M. Koo, In situ neutron diffraction study of the microstructure and tensile deformation behavior in Al-added high manganese austenitic steels, Acta Mater. 60 (2012) 2290–2299. doi:10.1016/j.actamat.2011.12.043.

[79] L. Zhu, H. Ruan, X. Li, M. Dao, H. Gao, J. Lu, Modeling grain size dependent optimal twin spacing for achieving ultimate high strength and related high ductility in nanotwinned metals, Acta Mater. 59 (2011) 5544–5557. doi:10.1016/j.actamat.2011.05.027.

[80] M. Waldenström, An experimental study of carbide-austenite equilibria in iron- base alloys with Mo, Cr, Ni, and Mn in the temperature range 1173 to 1373 K, Metall. Trans. A. 8 (1977) 1963–1977. doi:10.1007/BF02646571.

[81] J. Chu, Y. Bao, Study on the relationship between vacuum denitrification and manganese evaporation behaviours of manganese steel melts, Vacuum. 192 (2021). doi:10.1016/j.vacuum.2021.110420.

[82] Y. Lü, B. Hutchinson, D.A. Molodov, G. Gottstein, Effect of deformation and annealing on the formation and reversion of ε-martensite in an Fe-Mn-C alloy, Acta Mater. 58 (2010) 3079–3090. doi:10.1016/j.actamat.2010.01.045.

[83] H.M. Rietveld, A profile refinement method for nuclear and magnetic structures, J. Appl. Crystallogr. 2 (1969) 65–71. doi:10.1107/s0021889869006558.

[84] W.A. Johnson, R.F. Mehl, Reaction Kinetics in Processes of Nucleation and Growth, Trans. Am. Inst. Minning Metall. Eng. 135 (1939) 416–458.

[85] G.B. Olson, M. Cohen, Kinetics of strain-induced martensitic nucleation, Metall. Trans. A. 6 (1975) 791–795. doi:10.1007/BF02672301.

[86] T.R. Bieler, P. Eisenlohr, F. Roters, D. Kumar, D.E. Mason, M.A. Crimp, D. Raabe, The role of heterogeneous deformation on damage nucleation at grain boundaries in single phase metals, Int.

J. Plast. (2009). doi:10.1016/j.ijplas.2008.09.002.

[87]   S. Wei, G. Zhu, C.C. Tasan, Slip-twin transfer across phase boundaries: An in-situ investigation of a Ti-Al-V-Fe (α+β) alloy, Acta Mater. 206 (2020) 116520. doi:10.1016/j.actamat.2020.116520.

[88]   D. Wei, X. Li, W. Heng, Y. Koizumi, F. He, W.M. Choi, B.J. Lee, H.S. Kim, H. Kato, A. Chiba, Novel Co-rich high entropy alloys with superior tensile properties, Mater. Res. Lett. (2019). doi:10.1080/21663831.2018.1553803.

[89]   N. Glavatska, I. Glavatsky, G. Mogilny, V. Gavriljuk, Magneto-thermal shape memory effect in Ni-Mn-Ga, Appl. Phys. Lett. 80 (2002) 3533–3535. doi:10.1063/1.1478130.

[90]   P.M. Anderson, J.P. Hirth, J. Lothe, Theory of dislocations 3rd Edition, 2017.

[91]   M.H. Yoo, Slip, twinning, and fracture in hexagonal close-packed metals, Metall. Trans. A. (1981). doi:10.1007/BF02648537.

[92]   R. Ahmad, Z. Wu, W.A. Curtin, Analysis of double cross-slip of pyramidal I ⟨c+a⟩ screw dislocations and implications for ductility in Mg alloys, Acta Mater. (2020). doi:10.1016/j.actamat.2019.10.053.

[93]   B.Y. Liu, F. Liu, N. Yang, X.B. Zhai, L. Zhang, Y. Yang, B. Li, J. Li, E. Ma, J.F. Nie, Z.W. Shan, Large plasticity in magnesium mediated by pyramidal dislocations, Science (80-.). 364 (2019) 73–75. doi:10.1126/science.aaw2843.

[94]   H. Fan, J.A. El-Awady, Towards resolving the anonymity of pyramidal slip in magnesium, Mater. Sci. Eng. A. 644 (2015) 318–324. doi:10.1016/j.msea.2015.07.080.

[95]   Y.K. Lee, C.S. Choi, Driving force for $\gamma\rightarrow\varepsilon$ martensitic transformation and stacking fault energy of γ in {Fe-Mn} binary system, Metall. Mater. Trans. A. 31 (2000) 355–360.

[96]   A. Chakraborty, M. Adhikary, T. Venugopalan, V. Singh, T. Nanda, B.R. Kumar, Effect of ferrite-martensite interface morphology on bake hardening response of DP590 steel, Mater. Sci. Eng. A. 676 (2016) 463–473. doi:10.1016/j.msea.2016.09.018.

[97]   Y. Aruga, M. Kozuka, Y. Takaki, T. Sato, Evaluation of Solute Clusters Associated with Bake-Hardening Response in Isothermal Aged Al-Mg-Si Alloys Using a Three-Dimensional Atom Probe, Metall. Mater. Trans. A Phys. Metall. Mater. Sci. 45 (2014) 5906–5913. doi:10.1007/s11661-014-2548-y.

[98]   R.E. Reed, A.S. Gijilec, Concerning the mechanics of type-A Portevin-Le Chatelier Plastic Flow Initiation in Al 6061, Metall. Trans. A. 6 (1975) 461–466.

[99]   D. Wei, A. Anniyaer, Y. Koizumi, K. Aoyagi, M. Nagasako, H. Kato, A. Chiba, On microstructural homogenization and mechanical properties optimization of biomedical Co-Cr-Mo alloy additively manufactured by using electron beam melting, Addit. Manuf. 28 (2019) 215–227. doi:10.1016/j.addma.2019.05.010.

[100]   K. Ueki, K. Ueda, M. Nakai, T. Nakano, T. Narushima, Microstructural Changes During Plastic Deformation and Corrosion Properties of Biomedical Co-20Cr-15W-10Ni Alloy Heat-Treated at 873 K, Metall. Mater. Trans. A Phys. Metall. Mater. Sci. 49 (2018) 2393–2404. doi:10.1007/s11661-018-4597-0.

[101]   A. Kisko, A.S. Hamada, J. Talonen, D. Porter, L.P. Karjalainen, Effects of reversion and recrystallization on microstructure and mechanical properties of Nb-alloyed low-Ni high-Mn austenitic stainless steels, Mater. Sci. Eng. A. 657 (2016) 359–370. doi:10.1016/j.msea.2016.01.093.

[102] J. Han, Y.K. Lee, The effects of the heating rate on the reverse transformation mechanism and the phase stability of reverted austenite in medium Mn steels, Acta Mater. 67 (2014) 354–361. doi:10.1016/j.actamat.2013.12.038.

[103] S. Kajiwara, T. Kikuchi, Reversible movement of the austenite-martensite interface and dislocation structures in reverse-transformed austenite in Fe-Ni-C alloys, Philos. Mag. A Phys. Condens. Matter, Struct. Defects Mech. Prop. 48 (1983) 509–526. doi:10.1080/01418618308234910.

[104] S. Ogata, J. Li, S. Yip, Energy landscape of deformation twinning in bcc and fcc metals, Phys. Rev. B - Condens. Matter Mater. Phys. 71 (2005) 1–11. doi:10.1103/PhysRevB.71.224102.

[105] V. V ífek, Intrinsic stacking faults in body-centred cubic crystals, Philos. Mag. 18 (1968) 773–786. doi:10.1080/14786436808227500.

[106] O. Blaschko, G. Krexner, J. Pleschiutschnig, G. Ernst, C. Hitzenberger, H.P. Karnthaler, A. Korner, Coherent modulated structure during the martensitic hcp-fcc phase transition in Co and in a CoNi alloy, Phys. Rev. Lett. 60 (1988) 2800–2803. doi:10.1103/PhysRevLett.60.2800.

[107] P. Tolédano, G. Krexner, M. Prem, M. Prem, H.P. Weber, V.P. Dmitriev, Theory of the martensitic transformation in cobalt, Phys. Rev. B - Condens. Matter Mater. Phys. (2001). doi:10.1103/PhysRevB.64.144104.

[108] Y. Chen, Y. Li, Y. Koizumi, H. Haider, A. Chiba, Effects of carbon addition on wear mechanisms of CoCrMo metal-on-metal hip joint bearings, Mater. Sci. Eng. C. (2017). doi:10.1016/j.msec.2017.03.211.

[109] B.S. Lee, Y. Koizumi, H. Matsumoto, A. Chiba, Collective behavior of strain-induced martensitic transformation (SIMT) in biomedical Co-Cr-Mo-N alloy polycrystal: An ex-situ electron backscattering diffraction study, Mater. Sci. Eng. A. (2014). doi:10.1016/j.msea.2014.05.071.

[110] T. Mitsunobu, Y. Koizumi, B.S. Lee, A. Chiba, Asymmetric slip trace formation in tension/compression cyclic deformation of biomedical Co-Cr-Mo-N alloy with negative stacking fault energy, Scr. Mater. (2014). doi:10.1016/j.scriptamat.2013.10.015.

[111] R. Lizárraga, F. Pan, L. Bergqvist, E. Holmström, Z. Gercsi, L. Vitos, First Principles Theory of the hcp-fcc Phase Transition in Cobalt, Sci. Rep. (2017). doi:10.1038/s41598-017-03877-5.

[112] B. Geddes, H. Leon, X. Huang, Superalloys: Alloying and Performance, 2010.

[113] Z. Li, C.C. Tasan, K.G. Pradeep, D. Raabe, A TRIP-assisted dual-phase high-entropy alloy: Grain size and phase fraction effects on deformation behavior, Acta Mater. 131 (2017) 323–335. doi:10.1016/j.actamat.2017.03.069.

[114] S. Zaefferer, N.N. Elhami, Theory and application of electron channelling contrast imaging under controlled diffraction conditions, Acta Mater. 75 (2014) 20–50. doi:10.1016/j.actamat.2014.04.018.

[115] F. He, S. Wei, J.L. Cann, Z. Wang, J. Wang, C.C. Tasan, Composition-dependent slip planarity in mechanically-stable face centered cubic complex concentrated alloys and its mechanical effects, Acta Mater. 220 (2021). doi:10.1016/j.actamat.2021.117314.

[116] R. Su, D. Neffati, S. Xue, Q. Li, Z. Fan, Y. Liu, H. Wang, Y. Kulkarni, X. Zhang, Deformation mechanisms in FCC Co dominated by high-density stacking faults, Mater. Sci. Eng. A. (2018). doi:10.1016/j.msea.2018.08.057.

[117] Y. Liu, Y. Chen, K.Y. Yu, H. Wang, J. Chen, X. Zhang, Stacking fault and partial dislocation dominated strengthening mechanisms in highly textured Cu/Co multilayers, Int. J. Plast. (2013).

doi:10.1016/j.ijplas.2013.03.005.

[118] M. Naeem, H. He, F. Zhang, H. Huang, S. Harjo, T. Kawasaki, B. Wang, S. Lan, Z. Wu, F. Wang, Y. Wu, Z. Lu, Z. Zhang, C.T. Liu, X.L. Wang, Cooperative deformation in high-entropy alloys at ultralow temperatures, Sci. Adv. (2020). doi:10.1126/sciadv.aax4002.

[119] B. Clausen, T. Lorentzen, T. Leffers, Self-consistent modelling of the plastic deformation of F.C.C. polycrstals and its implications for diffraction measurements of internal stresses, Acta Mater. (1998). doi:10.1016/S1359-6454(98)00014-7.

[120] S. Cheng, A.D. Stoica, X.L. Wang, Y. Ren, J. Almer, J.A. Horton, C.T. Liu, B. Clausen, D.W. Brown, P.K. Liaw, L. Zuo, Deformation crossover: From Nano- to mesoscale, Phys. Rev. Lett. (2009). doi:10.1103/PhysRevLett.103.035502.

[121] W. Woo, E.W. Huang, J.W. Yeh, H. Choo, C. Lee, S.Y. Tu, In-situ neutron diffraction studies on high-temperature deformation behavior in a CoCrFeMnNi high entropy alloy, Intermetallics. (2015). doi:10.1016/j.intermet.2015.02.020.

[122] L. Balogh, G. Ribárik, T. Ungár, Stacking faults and twin boundaries in fcc crystals determined by x-ray diffraction profile analysis, J. Appl. Phys. (2006). doi:10.1063/1.2216195.

[123] B.E. Warren, X-ray studies of deformed metals, Prog. Met. Phys. (1959). doi:10.1016/0502-8205(59)90015-2.

[124] B.E. Warren, E.P. Warekois, Stacking faults in cold worked alpha-brass, Acta Metall. (1955). doi:10.1016/0001-6160(55)90138-3.

[125] R.P. Reed, R.E. Schramm, Relationship between stacking-fault energy and x-ray measurements of stacking-fault probability and microstrain, J. Appl. Phys. (1974). doi:10.1063/1.1663122.

[126] L. Rémy, INTERACTION BETWEEN SLIP AND TWINNING SYSTEMS AND THE INFLUENCE OF TWINNING ON THE MECHANICAL BEHAVIOR OF fcc METALS AND ALLOYS., in: Metall. Trans. A, Phys. Metall. Mater. Sci., 1981. doi:10.1007/BF02648536.

[127] T.H. Lee, E. Shin, C.S. Oh, H.Y. Ha, S.J. Kim, Correlation between stacking fault energy and deformation microstructure in high-interstitial-alloyed austenitic steels, Acta Mater. (2010). doi:10.1016/j.actamat.2010.01.056.

[128] M. Hillert, Phase equilibria, phase diagrams and phase transformations: Their thermodynamic basis, second edition, 2007. doi:10.1017/CBO9780511812781.

[129] C.H.P. Lupis, Chemical Thermodynamics of Materials, Prentice Hall, 1993.

[130] M. Hillert, M. Jarl, A model for alloying in ferromagnetic metals, Calphad. (1978). doi:10.1016/0364-5916(78)90011-1.

[131] K. Oikawa, G.W. Qin, T. Ikeshoji, R. Kainuma, K. Ishida, Direct evidence of magnetically induced phase separation in the fcc phase and thermodynamic calculations of phase equilibria of the Co-Cr system, in: Acta Mater., 2002. doi:10.1016/S1359-6454(01)00433-5.

[132] A.T. Dinsdale, SGTE data for pure elements, Calphad. (1991). doi:10.1016/0364-5916(91)90030-N.

[133] J. Sato, K. Oikawa, R. Kainuma, K. Ishida, Experimental verification of magnetically induced phase separation in αCo phase and thermodynamic calculations of phase equilibria in the Co-W system, Mater. Trans. (2005). doi:10.2320/matertrans.46.1199.

[134] Y.F. Cui, X. Zhang, G.L. Xu, W.J. Zhu, H.S. Liu, Z.P. Jin, Thermodynamic assessment of Co-Al-W system and solidification of Co-enriched ternary alloys, J. Mater. Sci. (2011). doi:10.1007/s10853-010-5115-y.

[135] S. Yang, M. Jiang, H. Li, Y. Liu, L. Wang, Assessment of Co-Cr-Ni ternary system by

CALPHAD technique, Rare Met. (2012). doi:10.1007/s12598-012-0466-y.

[136] S.Y. Yang, M. Jiang, H.X. Li, L. Wang, Thermodynamic assessment of Co-Cr-W ternary system, Trans. Nonferrous Met. Soc. China (English Ed. (2011). doi:10.1016/S1003-6326(11)61007-8.

[137] L.Y. Tian, R. Lizárraga, H. Larsson, E. Holmström, L. Vitos, A first principles study of the stacking fault energies for fcc Co-based binary alloys, Acta Mater. (2017). doi:10.1016/j.actamat.2017.07.010.

[138] R. Zhang, S. Zhao, J. Ding, Y. Chong, T. Jia, C. Ophus, M. Asta, R.O. Ritchie, A.M. Minor, Short-range order and its impact on the CrCoNi medium-entropy alloy, Nature. (2020). doi:10.1038/s41586-020-2275-z.

[139] C.B. Carter, I.L.F. Ray, On the stacking-fault energies of copper alloys, Philos. Mag. (1977). doi:10.1080/14786437708235982.

[140] D.J.H. Cockayne, M.L. Jenkins, I.L.F. Ray, The measurement of stacking-fault energies of pure face-centred cubic metals, Philos. Mag. (1971). doi:10.1080/14786437108217419.

[141] Y.Y. Shang, Y. Wu, J.Y. He, X.Y. Zhu, S.F. Liu, H.L. Huang, K. An, Y. Chen, S.H. Jiang, H. Wang, X.J. Liu, Z.P. Lu, Solving the strength-ductility tradeoff in the medium-entropy NiCoCr alloy via interstitial strengthening of carbon, Intermetallics. (2019). doi:10.1016/j.intermet.2018.12.009.

[142] J.B. Baudouin, G. Monnet, M. Perez, C. Domain, A. Nomoto, Effect of the applied stress and the friction stress on the dislocation dissociation in face centered cubic metals, Mater. Lett. (2013). doi:10.1016/j.matlet.2012.10.117.

[143] G. Lu, N. Kioussis, V. V. Bulatov, Generalized-stacking-fault energy surface and dislocation properties of aluminum, Phys. Rev. B - Condens. Matter Mater. Phys. (2000). doi:10.1103/PhysRevB.62.3099.

[144] S. Ogata, J. Li, S. Yip, Energy landscape of deformation twinning in bcc and fcc metals, Phys. Rev. B - Condens. Matter Mater. Phys. (2005). doi:10.1103/PhysRevB.71.224102.

[145] M. Jo, Y.M. Koo, B.J. Lee, B. Johansson, L. Vitos, S.K. Kwon, Theory for plasticity of face-centered cubic metals, Proc. Natl. Acad. Sci. U. S. A. (2014). doi:10.1073/pnas.1400786111.

[146] K.P.D. Lagerlöf, J. Castaing, P. Pirouz, A.H. Heuer, Nucleation and growth of deformation twins: A perspective based on the double-cross-slip mechanism of deformation twinning, Philos. Mag. A. (2002). doi:10.1080/01418610208240069.

[147] L. Rémy, A. Pineau, B. Thomas, Temperature dependence of stacking fault energy in close-packed metals and alloys, Mater. Sci. Eng. (1978). doi:10.1016/0025-5416(78)90194-5.

[148] S.C. Park, L.P. Beckerman, R.E. Reed-Hill, On the Portevin-Le Chatelier Effect Due to Snoek Strain Aging in the Niobium Oxygen System, Metall. Trans. A, Phys. Metall. Mater. Sci. 14 A (1983) 463–469. doi:10.1007/BF02644223.

[149] Z. Lei, X. Liu, Y. Wu, H. Wang, S. Jiang, S. Wang, X. Hui, Y. Wu, B. Gault, P. Kontis, D. Raabe, L. Gu, Q. Zhang, H. Chen, H. Wang, J. Liu, K. An, Q. Zeng, T.G. Nieh, Z. Lu, Enhanced strength and ductility in a high-entropy alloy via ordered oxygen complexes, Nature. 563 (2018) 546–550. doi:10.1038/s41586-018-0685-y.

[150] K. Habib, M. Koyama, T. Tsuchiyama, H. Noguchi, Dislocation motion at a fatigue crack tip in a high-nitrogen steel clarified through in situ electron channeling contrast imaging, Mater. Charact. (2019). doi:10.1016/j.matchar.2019.109930.

[151] M. Ojima, Y. Adachi, Y. Tomota, Y. Katada, Y. Kaneko, K. Kuroda, H. Saka, Weak beam TEM study on stacking fault energy of high nitrogen steels, Steel Res. Int. (2009).

doi:10.2374/SRI09SP038.

[152]   S. Kibey, J.B. Liu, M.J. Curtis, D.D. Johnson, H. Sehitoglu, Effect of nitrogen on generalized stacking fault energy and stacking fault widths in high nitrogen steels, Acta Mater. (2006). doi:10.1016/j.actamat.2006.02.048.

[153]   Y.Z. Tian, L.J. Zhao, S. Chen, A. Shibata, Z.F. Zhang, N. Tsuji, Significant contribution of stacking faults to the strain hardening behavior of Cu-15%Al alloy with different grain sizes, Sci. Rep. (2015). doi:10.1038/srep16707.

[154]   F. He, Z. Wang, Q. Wu, D. Chen, T. Yang, J. Li, J. Wang, C.T. Liu, J. jung Kai, Tuning the defects in face centered cubic high entropy alloy via temperature-dependent stacking fault energy, Scr. Mater. (2018). doi:10.1016/j.scriptamat.2018.06.002.

[155]   H. Wei, Y. Wei, Interaction between a screw dislocation and stacking faults in FCC metals, Mater. Sci. Eng. A. (2012). doi:10.1016/j.msea.2012.01.115.

[156]   K. Rajan, Stacking fault strengthening in low stacking fault energy alloys, Scr. Metall. 17 (1983) 101–104.

[157]   W.W. Jian, G.M. Cheng, W.Z. Xu, C.C. Koch, Q.D. Wang, Y.T. Zhu, S.N. Mathaudhu, Physics and model of strengthening by parallel stacking faults, Appl. Phys. Lett. (2013). doi:10.1063/1.4822323.

[158]   V.S. Sarma, J. Wang, W.W. Jian, A. Kauffmann, H. Conrad, J. Freudenberger, Y.T. Zhu, Role of stacking fault energy in strengthening due to cryo-deformation of FCC metals, Mater. Sci. Eng. A. (2010). doi:10.1016/j.msea.2010.08.015.

[159]   G. Zhu, L. Wang, J. Wang, J. Wang, J.-S. Park, X. Zeng, Highly deformable Mg-Al-Ca alloy with Al2Ca precipitates, Acta Mater. (2020) In press.

[160]   A.H. Cottrell, LX. The formation of immobile dislocations during slip, London, Edinburgh, Dublin Philos. Mag. J. Sci. (1952). doi:10.1080/14786440608520220.

[161]   A.N. Stroh, Constrictions and jogs in extended dislocations, Proc. Phys. Soc. Sect. B. (1954). doi:10.1088/0370-1301/67/5/307.

[162]   P.B. Hirsch, Extended jogs in dislocations in face-centred cubic metals, Philos. Mag. (1962). doi:10.1080/14786436208201859.

[163]   G. Zhu, L. Wang, H. Zhou, J. Wang, Y. Shen, P. Tu, H. Zhu, W. Liu, P. Jin, X. Zeng, Improving ductility of a Mg alloy via non-basal <a> slip induced by Ca addition, Int. J. Plast. (2019). doi:10.1016/j.ijplas.2019.04.020.

[164]   H. Wu, G. Fan, An overview of tailoring strain delocalization for strength-ductility synergy, Prog. Mater. Sci. (2020). doi:10.1016/j.pmatsci.2020.100675.

[165]   R.W. Cahn, P. Haasen, Physical Metallurgy - vol 1, Phys. Metall. 1 (1996) 1042.

[166]   B. Li, E. Ma, Atomic shuffling dominated mechanism for deformation twinning in magnesium, Phys. Rev. Lett. (2009). doi:10.1103/PhysRevLett.103.035503.

[167]   A. Serra, D.J. Bacon, R.C. Pond, Comment on "atomic shuffling dominated mechanism for deformation twinning in magnesium," Phys. Rev. Lett. 104 (2010). doi:10.1103/PhysRevLett.104.029603.

[168]   H.A. Khater, A. Serra, R.C. Pond, Atomic shearing and shuffling accompanying the motion of twinning disconnections in Zirconium, Philos. Mag. 93 (2013) 1279–1298. doi:10.1080/14786435.2013.769071.

[169]   A. Ishii, J. Li, S. Ogata, Shuffling-controlled versus strain-controlled deformation twinning: The case for HCP Mg twin nucleation, Int. J. Plast. (2016). doi:10.1016/j.ijplas.2016.01.019.

[170] B.Y. Liu, J. Wang, B. Li, L. Lu, X.Y. Zhang, Z.W. Shan, J. Li, C.L. Jia, J. Sun, E. Ma, Twinning-like lattice reorientation without a crystallographic twinning plane, Nat. Commun. (2014). doi:10.1038/ncomms4297.

[171] Y. He, B. Li, C. Wang, S.X. Mao, Direct observation of dual-step twinning nucleation in hexagonal close-packed crystals, Nat. Commun. 11 (2020). doi:10.1038/s41467-020-16351-0.

[172] Q.J. Li, H. Sheng, E. Ma, Strengthening in multi-principal element alloys with local-chemical-order roughened dislocation pathways, Nat. Commun. (2019). doi:10.1038/s41467-019-11464-7.

[173] J. Ding, Q. Yu, M. Asta, R.O. Ritchie, Tunable stacking fault energies by tailoring local chemical order in CrCoNi medium-entropy alloys, Proc. Natl. Acad. Sci. U. S. A. (2018). doi:10.1073/pnas.1808660115.

[174] T.M. Smith, B.S. Good, T.P. Gabb, B.D. Esser, A.J. Egan, L.J. Evans, D.W. McComb, M.J. Mills, Effect of stacking fault segregation and local phase transformations on creep strength in Ni-base superalloys, Acta Mater. 172 (2019) 55–65. doi:10.1016/j.actamat.2019.04.038.

Appendix

A1. Core Computational Codes for Slip Trace Analyses

```
%https://github.com/shaolouwei/STrCryst
%Point-wise Schmid factor calculations for one input
%Plus slip trace predictions
%Computations in a sense to understand anisotropic plasticity in HCP
%Example only given for basal slip system for clarity



a=170.6;                   %input Euler angles as degree
b=144.0;
c=345.1;


c=c-30;                    %For HCP, we need to rotate before calculation


load=[0,1,0]               %input the loading direction, in TESCAN MIRA 3,
x=[0,1,0]; y=[1,0,0]
surf=[0,0,1]               %input the EBSD viewing direction, ND=[0,0,1]
SURF=[0,0,1]               %used for slip trace calculation


r=1.61;                    %input the c-to-a ratio of an HCP lattice from
synchrotron, 1.5946 for TiAlVFe [S.L. Wei et al., Acta Mater, 2020]



%Compute the G matrix
a=pi*a/180                 %convert deg. to rad.
b=pi*b/180
c=pi*c/180

a11=cos(a)*cos(c)-sin(a)*sin(c)*cos(b);    %compute the G matrix

a12=sin(a)*cos(c)+cos(a)*sin(c)*cos(b);

a13=sin(c)*sin(b);

a21=-cos(a)*sin(c)-sin(a)*cos(c)*cos(b);

a22=-sin(a)*sin(c)+cos(a)*cos(c)*cos(b);

a23=cos(c)*sin(b);

a31=sin(a)*sin(b);
```

```matlab
a32=-cos(a)*sin(b);

a33=cos(b);

G=[a11,a12,a13;a21,a22,a23;a31,a32,a33]

p=G*load'
surf=G*surf'


%Variants in basal slip system: <11-20>{0001}

h1=0
k1=0
i1=0
l1=1

u1=1
v1=1
t1=-2
w1=0

h2=0
k2=0
i2=0
l2=1

u2=-1
v2=2
t2=-1
w2=0


h3=0
k3=0
i3=0
l3=1

u3=2
v3=-1
t3=-1
w3=0
```

```matlab
n1=[(2*h1+k1)*(3^0.5)/3, k1, l1/r]
n1=n1/norm(n1)
s1=[(2*u1+v1)*(3^0.5)/2, 3*v1/2, w1*r]
s1=s1/norm(s1)


n2=[(2*h2+k2)*(3^0.5)/3, k2, l2/r]
n2=n2/norm(n2)
s2=[(2*u2+v2)*(3^0.5)/2, 3*v2/2, w2*r]
s2=s2/norm(s2)


n3=[(2*h3+k3)*(3^0.5)/3, k3, l3/r]
n3=n3/norm(n3)
s3=[(2*u3+v3)*(3^0.5)/2, 3*v3/2, w3*r]
s3=s3/norm(s3)


SF1=abs(dot(p,n1)*dot(p,s1))
SF2=abs(dot(p,n2)*dot(p,s2))
SF3=abs(dot(p,n3)*dot(p,s3))



%End of basal slip system

%Plot the slip trace
%Note that this calculation must be done in sample frame

n1=inv(G)*n1'
n2=inv(G)*n2'
n3=inv(G)*n3'

m1=cross(n1,SURF)
m2=cross(n2,SURF)
m3=cross(n3,SURF)

k1=-1/(m1(1,2)/m1(1,1))         %In Tescan MIRA3 one needs to reverse x and
y direction
k2=-1/(m2(1,2)/m2(1,1))
k3=-1/(m3(1,2)/m3(1,1))

ang1=rad2deg(atan(k1))
ang2=rad2deg(atan(k2))
ang3=rad2deg(atan(k3))

x=-1:0.1:1
```

```
y1=k1*x
y2=k2*x
y3=k3*x

plot(x,y1,'blue','LineWidth',1.5)
axis equal
axis([-1 1, -1 1])

hold on
```

A2. List of Publications

Thesis-related publications

[1] <u>S.L. Wei</u>, F. He, and C.C. Tasan*. Metastability in high-entropy alloys: a review. **Journal of Materials Research**, 2018, 33: 2924-2937. (Chapter 1)

[2] <u>S.L. Wei</u>, J. Kim, and C.C. Tasan*. Boundary micro-cracking in metastable $Fe_{45}Mn_{35}Co_{10}Cr_{10}$ high-entropy alloys. **Acta Materialia**, 2019, 168: 76-86. (Chapter 1)

[3] <u>S.L. Wei</u>, J. Kim, J.L. Cann, R. Gholizadeh, N. Tsuji, and C.C. Tasan*. Plastic strain-induced sequential martensitic transformation. **Scripta Materialia,** 2020, 185: 36-41. (Chapter 3)

[4] <u>S.L. Wei</u>, M. Xu, J.M. LeBeau, and C.C. Tasan*.Tuning mechanical metastability in FeMnCo medium entropy alloys and a peek into deformable hexagonal close-packed martensite, **Applied Physics Letters**, 2021, 119: 261905. (Chapter 3)

[5] <u>S.L. Wei</u>, M. Jiang, and C.C. Tasan*. Interstitial-free bake hardening realized by epsilon martensite back-transformation. **Metallurgical and Materials Transactions A,** 2019, 50: 3985-3991. (Chapter 3)

[6] <u>S.L. Wei</u> and C.C. Tasan*. Deformation faulting in a CoCrNiW complex concentrated alloy: a case of negative intrinsic stacking fault energy?. **Acta Materialia**, 2020, 200: 992-1007. (Chapter 4)

Other publications

[1] <u>S.L. Wei</u>, S.J. Kim, J.Y. Kang, Y. Zhang, Y.J. Zhang, T. Furuhara, E.S. Park, and C.C. Tasan*. Natural-mixing-guided design of refractory high-entropy alloys with as-cast tensile ductility. **Nature Materials,** 2020, 19: 1175-1181.

[2] <u>S.L. Wei</u>, J. Kim, and C.C. Tasan*. In-situ investigation of plasticity in a Ti-Al-V-Fe (α+β) alloy: Slip mechanisms, strain localization, and partitioning. **International Journal of Plasticity**, 2021, 103131.

[3] <u>S.L. Wei</u>, G. Zhu, and C.C. Tasan*. Slip-twinning interdependent activation across phase boundaries: an in-situ study of a Ti-Al-V-Fe (α+β) alloy. **Acta Materialia**, 2021, 206: 116520.

[4] <u>S.L. Wei</u>, D.P. Moriarty, and C.C. Tasan*. An in-situ SEM elevated temperature investigation of serrated plastic flow and damage micro-events in a CoCrFeNiW-C alloy. **Acta Materialia.** (Review report received Aug. 05, 2021, in revision)